Astronomy Letters, Vol. 29, No. 5, 2003, pp. 279–288. Translated from Pis'ma v Astronomicheskiĭ Zhurnal, Vol. 29, No. 5, 2003, pp. 323–333.

Observations of Soft Gamma-Ray or Hard X-ray Bursts in the GRIF Experiment on the *Mir* Orbiting Station

M. I. Kudryavtsev[1], S. I. Svertilov[2*], and O. V. Morozov[2]

[1] *Space Research Institute, Russian Academy of Sciences, ul. Profsoyuznaya 84/32, Moscow, 117810 Russia*

[2] *Institute of Nuclear Physics, Moscow State University, Vorob'evy gory, Moscow, 119992 Russia*

Received November 15, 2002

Abstract—During the GRIF experiment onboard the *Mir* orbiting station, the sky was monitored with a PX-2 wide-field (~1 sr) scintillation X-ray spectrometer to detect bursts in the photon energy range 10–300 keV. Because of the comprehensive instrumentation, which, apart from the X-ray and gamma-ray instruments, also included charged-particle detectors, the imitations of astrophysical bursts by magnetospheric electron precipitations and strongly ionizing nuclei were effectively filtered out. It was also possible to separate solar and atmospheric events. Several tens of bursts interpreted as being astrophysical were detected in the experiment at sensitivity levels $S \sim 10^{-7}$ erg cm^{-2} (for bursts whose spectra were characterized by effective temperatures $kT \sim 100$ keV) and $S \sim 3 \times 10^{-8}$ erg cm^{-2} (for bursts with $kT \sim 25$ keV). Some of the soft gamma-ray or hard X-ray bursts with $kT \sim 10$–50 keV were identified with the bursting pulsar GRO J1744–28. Our estimate of the detection rate for cosmological soft gamma-ray or hard X-ray bursts from the entire sky suggests that the distributions of long-duration (>1 s) gamma-ray bursts (GRBs) in characteristic energy kT and duration are inconsistent with the steady-state cosmological model in which the evolution of burst sources is disregarded. Based on GRIF and BATSE/CGRO data, we conclude that most of the GRB sources originate at redshifts $1 < z < 5$.

Key words: *cosmic GRBs, X-ray transients, soft gamma-ray repeaters, distribution, energy spectrum, duration.*

INTRODUCTION

The most complete results to date on the statistics of gamma-ray bursts (GRBs) have been obtained from BATSE observations at the Compton Gamma-Ray Observatory (CGRO) mainly for the energy range 0.05–1 MeV (the main results of other experiments, in particular, KONUS observations on the *Venera* spacecraft also refer to this energy range). As regards the distribution in spectral hardness (effective temperature kT), most of the GRBs detected in the BATSE/CGRO experiment are known to have $kT > 50$ keV (Paciesas *et al.* 1999a, 1999b). Below, such GRBs are called typical ones. Whether the relatively small number of soft bursts in the population of typical GRBs reflects their true kT distribution or is the result of selection related to the high energy threshold in most experiments (the nominal BATSE/CGRO energy threshold is 20 keV; the actual triggering threshold is 50 keV) is still an open question (Paciesas *et al.* 2001). In any case, the BATSE data themselves, which contain information on the so-called GRBs without gamma-ray radiation, i.e., the bursts detected only in the first two channels (in the energy range 20–100 keV), indicate that the population of soft gamma-ray or hard X-ray bursts may exist. BATSE/CGRO data on the GRB durations suggest that two groups of bursts differing in characteristic durations Δt can be separated: relatively short ($\Delta t < 1$ s) and longer ($\Delta t > 1$ s) bursts (Koshut *et al.* 1996; Kouveliotou *et al.* 1993).

It should be noted that recurrent bursts from the same source are not characteristic of typical GRBs. At the same time, events that occur in the same source can contribute to the population of soft gamma-ray or hard X-ray bursts. Thus, the observations carried out in recent years on various spacecraft (*Venera*, *Prognoz*, *Granat*, CGRO) have revealed several recurrent sources of relatively soft GRBs, the so-called soft gamma-ray repeaters. The latter differ in their morphological properties from the main population of typical GRBs (Mazets *et al.* 1981; Kouveliotou *et al.* 1994, 1998, 1999; Hurley *et al.* 1999). In particular, they are generally short and exhibit relatively soft spectra (with an effective temperature $kT \sim 30$–40 keV). Neutron stars with

* E-mail: sis@coronas.ru

strong magnetic fields (magnetars), which form an independent class of Galactic objects, are currently believed to be the sources of recurrent GRBs (Duncan and Thomson 1992; Vasisht and Gotthelf 1997). This class significantly differs from the population of typical GRB sources, which, in turn, are associated with processes at cosmological distances (Paczynski 1986; Kulkarni *et al.* 1998).

In cosmological models, the origin of GRBs is associated with processes at the final evolutionary stages of massive stars, such as the collapse of a massive star (MacFadyen *et al.* 2001) or the merging of neutron stars (Eichler *et al.* 1989; Janka *et al.* 1999). Therefore, cosmological scenarios suggest that the GRB rate, to a certain extent, reflects the star-formation history up to high values of $z \sim 20$ (Totani 1997; 1999; Wijers *et al.* 1998; Blain and Natarajan 2000; Barkana and Loeb 2001). Because of the cosmological redshift, one might expect the bursts that occur at high z to be observed as softer GRBs—the so-called Mallozzi effect (the anticorrelation between spectral hardness and intensity; Mallozzi *et al.* 1995). Since the GRB rate in most cosmological models is assumed to be at a maximum at the epoch of primordial star formation, one might expect an increase in the observed direction rate of both dimmer and softer bursts. Models that predict the highest burst rate at $z = 1$–5 (Lipunov *et al.* 1993), which corresponds to the maximum star-formation rate inferred by Madau *et al.* (1998) and Hughes *et al.* (1998), and models in which the burst rate is also high at epochs corresponding to $z > 5$ (Bromm and Loeb 2002; Donaghy *et al.* 2002) are considered. In essence, what values of z correspond to the maximum GRB rate and whether the GRB sources refer to the epoch of primordial star formation are still open questions.

Searches for the population of soft (i.e., with $kT <$ 50 keV) cosmic bursts are of current interest in further studying the events mentioned above. Statistical characteristics of such bursts, in particular, their distributions in spectral hardness and duration, can give answers to the following questions: Is there a boundary between the bursts from gamma-ray repeaters and the typical GRBs and over what morphological burst characteristics does it pass? Do soft GRBs unrelated to repeaters exist? Are there actually several separate groups in the population of typical GRBs? In connection with the last question, it should be noted that all of the results that provide evidence for the cosmological nature of GRBs, based on the identification of their sources by afterglows (Costa *et al.* 1997; Van Paradijs *et al.* 1997; Frail *et al.* 1997) and on the analysis of statistical dependences, such as the dilatation effect (Norris *et al.* 1994; Mitrofanov 1998) and the Mallozzi effect, have been obtained precisely for the group of relatively long bursts ($\Delta t > 1$ s). As regards the shorter bursts, no data that would strongly suggest that they belong to the population of objects at cosmological distances have yet been obtained. In light of the aforesaid, investigating the separate population of soft GRBs is important both for further progress in understanding the nature of typical GRBs and for studying magnetars, a new type of astrophysical object.

Here, based on the data obtained during the multipurpose GRIF experiment onboard the *Mir* orbiting station, we study the morphological and statistical characteristics of soft gamma-ray or hard X-ray bursts. The distinctive features of this experiment are a high sensitivity ($\sim 3 \times 10^{-8}$ erg cm^{-2}) and a low burst photon detection energy threshold ($\sim$10 keV), which allow not only typical GRBs but also softer events to be observed.

THE OBSERVING TECHNIQUE FOR COSMIC X-RAY AND GAMMA-RAY BURSTS IN THE GRIF EXPERIMENT

The GRIF experiment was carried out on the Spectrum module of the Mir orbiting station (an average altitude of $\sim$400 km, an orbital inclination of 51°, and a revolution period of $\sim$90 min) from October 1995 through June 1997 (Kudryavtsev *et al.* 1995, 1996; Bogomolov *et al.* 1997).

To search for and analyze hard X-ray and gamma-ray bursts from astrophysical objects, we used data from the PX-2 directional scintillation spectrometer: the observed photon energy range is $\Delta E_\gamma =$ 10–300 keV; the effective area in various energy ranges is $S \sim 300$ cm^2 (20–100 keV), $S \sim 200$ cm^2 (100–200 keV), and $S \sim 100$ cm^2 (200–300 keV); and the field of view is $\Omega \sim 1$ sr. This instrument consisted of seven identical detector units and an electronic data processing and transformation system. The detectors were based on phoswich: a CsI(Na) crystal (0.35 cm in thickness, 8.0 cm in diameter)—an anticoincidence cap of a plastic scintillator viewed (from the lead glass) by the same photomultiplier as the CsI(Na) crystal.

During the entire experiment, we measured the 5-s-averaged count rates of X-ray photons in the energy ranges 10–50, 25–50, 50–100, 100–200, and 200–300 keV and of accompanying charged particles. Additional data output was provided in the 10–50, 25–50, and 50–100 keV channels, which made it possible to measure the count rates with a time resolution of 2.5 s. The PX-2 instrument and its location and orientation were described in more detail previously (Kudryavstev *et al.* 2002).

The potentialities of the GRIF experiment in detecting astrophysical bursts can be assessed from the

background count rates in the PX-2 X-ray channels. A 5σ criterion was used to select bursts. Given the measured background count rates in the energy range 25–100 keV ($\sim$100 counts s^{-1}), the count-rate integration time (5 s), and the effective area $\sim$300 cm^2 for a burst with a standard duration of 5 s and an optically thin plasma spectrum

$$dJ/dE = J_0(E_0/E)\exp(-E/kT) \qquad (1)$$

with $kT = 25$ keV, the threshold burst fluence is $\sim 3 \times 10^{-8}$ erg cm^{-2} (for a typical GRB with $kT =$ 100 keV, the corresponding value is $\sim 10^{-7}$ erg cm^{-2}; i.e., it corresponds to the BATSE/CGRO sensitivity threshold).

Based on our estimates, we may conclude that the threshold burst fluences reached in the experiment with the PX-2 instrument are lower than those reached with the BATSE instrumentation for soft bursts ($kT < 50$ keV). For bursts with $kT > 50$ keV, the two experiments have a similar sensitivity.

RESULTS OF THE GRIF OBSERVATIONS OF SOFT GAMMA-RAY OR HARD X-RAY BURSTS

When selecting candidates for astrophysical bursts, apart from the 5σ criterion for the peak 25–100 keV intensity, we used two additional conditions: (1) an increase in the X-ray channels should not be accompanied by a rise in the corresponding electron fluxes and (2) a statistically significant increase in the count rate should be recorded by at least two of the seven detectors. The first condition eliminates the imitations of astrophysical X-ray and gamma-ray bursts by the bremsstrahlung of precipitating magnetospheric electrons. Such precipitations were controlled with the FON-1 sensitive energetic-electron detector in the GRIF instrumentation. This detector could record electron fluxes with energies of several hundred keV at a level $\geq 10^{-1}$ cm^{-2} s^{-1} sr^{-1} in all segments of the Mir orbit outside the zones of trapped radiation. The second condition allows the burst imitations due to the exposure of the scintillation crystals to highly ionizing particles, mostly heavy nuclei, to be removed. Because of the specific PX-2 detector arrangement, the probability of a nucleus passing through two detectors is negligible. Nevertheless, in order to exclude this possibility of imitations as well, we imposed a more stringent condition when selecting the bursts being analyzed here: only the events for which statistically significant increases in the count rates of three neighboring detectors were recorded were considered as candidates for astrophysical bursts.

As a result, we selected several tens of events that satisfied the above criteria. For these events, we chose

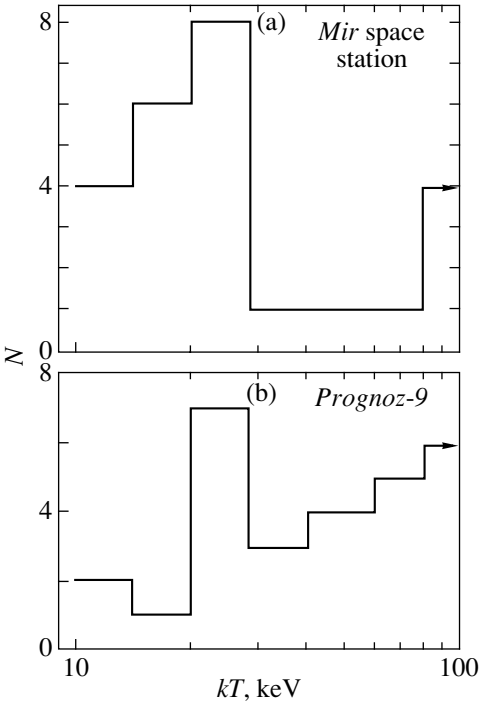

Fig. 1. The distribution of astrophysical bursts detected during the GRIF experiment in kT (the effective temperature in the optically thin plasma spectral representation (1)): (a) on the *Mir* space station and (b) on the *Prognoz-9* station (Kudryavtsev and Svertilov 1988)

a spectral representation in the form (1). To determine the parameter kT, the peak flux in a given energy range, and the spectral flux density at a certain energy $J(E = E_0)$, we used special instrumental functions that related the spectral parameters and count rates in different channels of the instrument (Kudryavtsev *et al.* 2002). In this approach, the error in kT can be systematic in nature and, to a large extent, is determined by the form of the instrumental function, which relates kT to the ratio of the count rates in adjacent energy ranges. The statistical scatter of count rates in the channels also contributes to the error in kT. For the bursts detected at the sensitivity threshold (i.e., near the 5σ level), the mean statistical error in kT is $\sim$20% for $kT = 10$–30 keV, $\sim$30% for $kT =$ 30–50 keV, and $\sim$50% for $kT = 50$–100 keV.

The bursts selected by the above criteria are characterized by kT in the range from $\sim$10 to $\sim$500 keV. The solar origin of these bursts can be ruled out, because no manifestations of solar flaring activity were observed when the events were recorded (Coffey 2001). Therefore, these bursts are considered below as candidates for astrophysical bursts from GRIF data. Their kT distribution is shown in Fig. 1a. Figure 1b shows the kT distribution (in a spectral representation of the type (1)) of astrophysical bursts detected during an experiment onboard the *Prognoz-9*

Table

Burst detection date, UT	Duration, s	kT, keV	Fluence at >25 keV, erg cm^{-2}	Peak 25–50 keV flux, phot cm^{-2} s^{-1}	Burst detection date in other experiments
951108 $11^h35^m03^s$	∼8.7	70 ± 30	$(1.0 \pm 0.4) \times 10^{-7}$	$(6.6 \pm 1.2) \times 10^{-2}$	GRB
951111 09 42 06	15–20	500 ± 200	$(2.1^{+2.0}_{-1.0}) \times 10^{-5}$	$(4.7^{+4.7}_{-2.3}) \times 10^{-1}$	GRB, KONUS/WIND, 951111 $09^h42^m40^s$
951201 09 00 59	∼19.2	15 ± 3	$(6.8^{+6.0}_{-3.0}) \times 10^{-7}$	$(5.5^{+5.5}_{-2.7}) \times 10^{-1}$	–
951227 14 11 11	∼ 9.0	10.0 ± 2.0	$(6.9 \pm 5.0) \times 10^{-7}$	$(2.4^{+2.5}_{-1.2}) \times 10^{0}$	KONUS/WIND, 95122714$^h11^m57^s$ GRO J1744-28
951227 17 15 52	∼25.5	24 ± 5	$(1.6^{+1.6}_{-0.8}) \times 10^{-6}$	$(2.6^{+2.6}_{-1.3}) \times 10^{0}$	KONUS/WIND, 951227 $17^h16^m39^s$ GRO J1744-28
960102 00 10 34	∼9.0	18 ± 3.5	$(1.8 \pm 0.7) \times 10^{-7}$	$(6.7 \pm 1.3) \times 10^{-1}$	KONUS/WIND, 960102 $00^h12^m31^s$ GRO J1744-28
960102 03 04 02	∼3.7	14 ± 3	$(9.4 \pm 3.0) \times 10^{-8}$	$(3.3 \pm 0.7) \times 10^{-1}$	KONUS/ WIND, 960102 $03^h11^m01^s$ GRO J1744-28 BATSE burster, 960102 $03^h10^m00^s$
960102 04 43 51	∼12.4	28 ± 5.5	$(5.0 \pm 4.0) \times 10^{-7}$	$(1.4 \pm 1.0) \times 10^{0}$	–
960103 13 55 39	∼9.0	13 ± 2.5	$(1.2 \pm 0.5) \times 10^{-7}$	$(4.0 \pm 0.8) \times 10^{-1}$	–
960103 17 00 03	∼9.0	22 ± 4.5	$(1.7 \pm 0.7) \times 10^{-7}$	$(1.4 \pm 0.3) \times 10^{-1}$	KONUS/WIND, 960103 $17^h00^m08^s$ GRO J1744-28
960103 18 22 46	∼5.1	10.5 ± 2.0	$(8.0 \pm 3.0) \times 10^{-8}$	$(3.7 \pm 0.7) \times 10^{-1}$	KONUS/WIND, 960103 $18^h22^m22^s$ GRO J1744-28 BATSE burster, 960103 $18^h22^m00^s$
960103 20 10 49	∼14.1	15 ± 3	$(5.0 \pm 4.0) \times 10^{-7}$	$(5.0 \pm 3.0) \times 10^{-1}$	KONUS/WIND, 960103 $20^h10^m30^s$ GRO J1744-28
960105 15 36 39	∼9.0	20.5 ± 2.0	$(1.4 \pm 0.3) \times 10^{-7}$	$(3.7 \pm 0.7) \times 10^{-1}$	–
960117 07 45 46	∼1.4	60 ± 10	$(1.7^{+1.7}_{-0.8}) \times 10^{-5}$	$(6.8^{+6.8}_{-3.2}) \times 10^{1}$	GRB
960123 12 06 42	∼20.4	300 ± 100	$(5.0 \pm 1.0) \times 10^{-6}$	$(1.0 \pm 0.2) \times 10^{-1}$	GRB, KONUS/WIND, 961123 $12^h07^m21^s$ BATSE/CGRO (nontriggered event), 961123 $12^h07^m18^s$
960128 18 18 13	∼2.2	125 ± 40	$(1.9 \pm 0.6) \times 10^{-7}$	$(2.5 \pm 0.2) \times 10^{-1}$	GRB
960201 05 22 20	∼1.7	13 ± 2.5	$(4.5 \pm 2.0) \times 10^{-8}$	$(5.0 \pm 1.0) \times 10^{-1}$	–
960315 14 59 32	∼1.3	20 ± 4	$(2.0^{+2.0}_{-1.0}) \times 10^{-6}$	$(2.0^{+2.0}_{-1.0}) \times 10^{1}$	–
961118 23 33 21	∼2.7	20 ± 4	$(5.0^{+5.0}_{-2.5}) \times 10^{-7}$	$(2.5^{+2.5}_{-1.2}) \times 10^{0}$	–
970108 17 56 38	∼7.0	15 ± 3	$(9.0 \pm 4.0) \times 10^{-8}$	$(3.8 \pm 0.7) \times 10^{-1}$	–
970108 20 53 55	∼6.4	20 ± 4	$(2.7 \pm 2.0) \times 10^{-7}$	$(1.2 \pm 0.7) \times 10^{0}$	BATSE bursting pulsar, 970108 $20^h53^m00^s$
970109 21 32 23	∼5.1	38 ± 10	$(5.5 \pm 3.5) \times 10^{-7}$	$(6.0 \pm 0.4) \times 10^{-1}$	–
970110 00 28 48	∼ 9.0	22.5 ± 4.5	$(6.0 \pm 4.0) \times 10^{-7}$	$(1.1 \pm 0.7) \times 10^{0}$	–
970601 19 19 02	∼51	100 ± 10	$(3.5 \pm 2.0) \times 10^{-5}$	$(2.7 \pm 1.6) \times 10^{0}$	GRB, KONUS/WIND, 970601 $19^h19^m30^s$

station (Kudryavstev and Svertilov 1988). Note that, despite the poor statistics, the two distributions are similar to within details. The salient feature of the two distributions is a statistically significant number of events with kT in the range 10–50 keV. Below, the bursts with $kT \sim 10$–50 keV and $kT > 50$ keV are called soft gamma-ray or hard X-ray bursts and typical GRBs, respectively.

Thus, a total of 24 bursts that satisfied the condition kT >10 keV, i.e., those belonging to hard X-ray or gamma-ray bursts and typical GRBs, were detected in the GRIF experiment. The basic parameters of these bursts are given in the table.

In those cases where an event fitted into a single bin in the time series (i.e., its duration was shorter than 5.1 s), we used a comparison of the count rates measured by the following two independent methods to estimate the duration: using a digital-to-analog converter whose output gave the number of pulses in a given time interval ($N_{\rm DAC}$) and a log-counting ratemeter (frequency meter) whose readings $N_{\rm INT}$ are related to $N_{\rm DAC}$ by

$$N_{\rm RATE} = N_{\rm DAC}(1 - \exp(-\Delta t/\tau)), \qquad (2)$$

where Δt is the duration of the increase and $\tau \sim 5$ s is a parameter that characterizes the temporal properties of the ratemeter. Relation (2) was experimentally tested during ground-based calibrations of the PX-2 instrument by simulating a burst by an oscillator pulse packet. To within the statistical scatter, it holds for pulse packets with a duration up to 0.5 s.

We determined the fluence S (>25 keV) from the spectral flux density integrated over the burst duration at energy 25 keV and the parameter kT. For a more accurate determination of S, we estimated the offset θ of the burst sources from the PX-2 axis. The ratio of the dispersions of the count rates measured with individual detectors, σ_i, to the value $\bar{N}$ averaged over all detectors can be used as a measure of this offset. This ratio was calculated for various offsets and azimuthal directions by assuming that the difference between the count rates of individual detectors is attributable to geometric factors only (different relative exposed areas). Averaging over various azimuthal directions yielded the function $\sigma_i/\bar{N}(\theta)$ that was used to determine the offset θ.

Among the candidates for astrophysical bursts listed in the table, the six hardest ($kT > 50$ keV) bursts have previously been interpreted as typical GRBs (Kudryavtsev *et al.* 2002). At least three of them were observed in other experiments: BATSE/CGRO (Kommers *et al.* 2001) and KONUS/WIND (Golenetskii 2002). Among the 18 bursts that belong to the category of soft gamma-ray or hard X-ray bursts, eight were reliably identified with bursts from the bursting pulsar GRO J1744–28 (Kouveliotou *et al.* 1996), which were also detected in the BATSE/CGRO (Briggs 2002) and KONUS/WIND (Golenetskii 2002) experiments.

As follows from the data presented in the table, most of the soft gamma-ray or hard X-ray bursts were detected during the GRIF experiment in late December 1995–early January 1996 (ten bursts) and in January 1997 (four bursts). During these periods, the bursting pulsar GRO J1744–28 was within the PX-2 field of view (Kouveliotou *et al.* 1996). Two periods of bursting activity in this pulsar are known to have been observed: from December 2, 1995, through May 1996 and from December 1, 1996, through April 1997. In January 1996 and January 1997, the bursting activity of this source was high and reached ~40 bursts per day (Aptekar *et al.* 1998; Woods *et al.* 1999). In their morphological parameters ($kT \sim 10$–20 keV, duration ~10 s, fluence $\sim 10^{-7}$ erg cm^{-2}), the bursts detected during the GRIF experiment in January 1996 and January 1997 also closely correspond to the bursts from GRO J1744–28. Moreover, even the tendency pointed out by Woods *et al.* (1999) for the burst duration to decrease during the second outburst of activity (on average, less than 10 s) compared to the burst duration during the first outburst of its activity (on average, more that 10 s) can be traced. Thus, although only eight bursts were reliably identified with the pulsar GRO J1744–28 (see the table), we can assume with a high confidence that all of the 14 soft gamma-ray or hard X-ray bursts detected during the GRIF experiment in December 1995–January 1996 and in January 1997 are associated with the transient pulsar GRO J1744–28. Therefore, only four bursts observed during the periods when either no objects similar to soft gamma-ray repeaters were within the PX-2 field of view or their activity was low can be considered as a kind of extension of the population of typical GRBs to $kT < 50$ keV. In this case, we cannot rule out the possibility that these bursts could be associated with as yet unidentified objects similar to soft gamma-ray repeaters or bursting pulsars, and it is appropriate to talk about the upper limit on the rate of soft cosmological GRBs obtained in the GRIF experiment.

DISCUSSION AND CONCLUSIONS

Let us consider in more detail the question of what additional information the GRIF experiment can give when discussing the cosmological nature of GRBs.

Astrophysical bursts detected during the GRIF experiment onboard the *Mir* space station and GRBs from the 4B BATSE catalog (Meegan *et al.* 1996) are

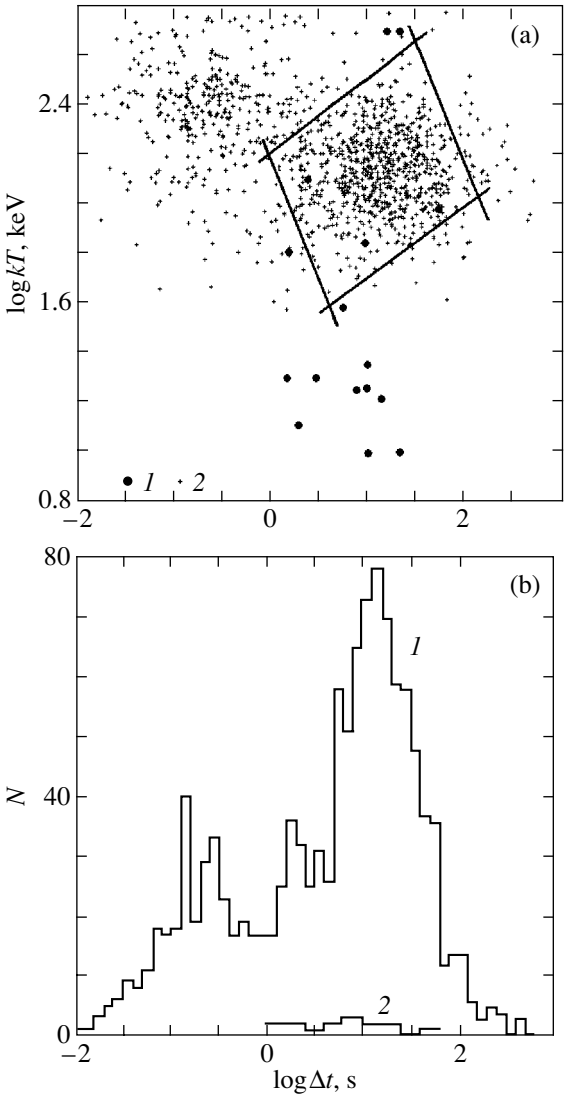

Fig. 2. (a) The spectral hardness–duration diagram for astrophysical bursts detected in the GRIF experiment onboard the *Mir* space station (*1*) and GRBs from the **4B** BATSE/CGRO catalog (*2*). The lines bound the region of typical long-duration (>1 s) GRBs. (b) The GRB duration distribution constructed from BATSE/CGRO data (*1*) and the duration distribution of astrophysical objects detected in the GRIF experiment (*2*).

marked in the spectral hardness–duration diagram in Fig. 2a. The standard quantity T_{50} (Meegan *et al.* 1996) was used as a measure of the duration Δt for GRBs from the BATSE catalog, while the kT values were determined from the ratio of the fluences in the energy ranges 20–50 and 50–300 keV under the assumption of a 100% detector efficiency. Figure 2b shows the distribution folded in kT, i.e., the differential burst duration distribution. The distributions shown in Fig. 2 reflect the existence of two groups of bursts: relatively hard short ($\Delta t < 1$ s) and, on average, softer and long ($\Delta t > 1$ s) bursts.

As we see from Fig. 2, the durations of most of the astrophysical bursts with kT in the range 10–50 keV detected during the GRIF experiment lie within the range 2–30 s; i.e., they correspond to the group of long-duration bursts. This suggests that, probably, most of the soft gamma-ray or hard X-ray bursts observed during the GRIF experiment are not cosmological, because, otherwise, their durations would be, on average, longer than those of the GRBs detected during the BATSE/CGRO experiment. Nevertheless, when recalculated to the entire sky, the number of soft gamma-ray or hard X-ray bursts detected during the GRIF experiment that were definitely not identified with known Galactic sources can be considered as an upper limit on the number of observed cosmological soft GRBs, i.e., bursts that can belong to the extension of the population of typical GRBs to $kT < 50$ keV. Taking into account the data shown in Fig. 2, we will compare only the events that belong to the group of long-duration ($\Delta t > 1$ s) GRBs in the context of our subsequent analysis.

For objects at cosmological distances, the observed quantities $\Delta t^{\rm obs}$ and $kT^{\rm obs}$, which characterize the duration and spectral hardness (characteristic energy), respectively, are known to be related to the corresponding values of Δt_0 and kT_0 in the source via the factor $1 + z$, where z is the cosmological redshift. Therefore, if the burst spectra and durations in the source were identical and if the observed spread of bursts in kT and Δt were attributable to the cosmological redshift and dilatation effects, then the distribution in kT and Δt would reflect the z distribution of bursts sources. Clearly, the number of observed bursts with kT larger than a given value is determined by the observable number of bursts sources $N(<z)$ located at distances within the volume specified by z that corresponds to the $kT_0/kT^{\rm obs}$ ratio

$$N(>kT) = N(<z = kT_0/kT - 1). \qquad (3)$$

Figure 3 shows the integral kT distributions of astrophysical bursts detected during the GRIF experiment (except for the bursts that were reliably identified with GRO J1744–28) and long-duration ($\Delta t >$ 1 s) GRBs from the 4B BATSE catalog. These distributions were recalculated to take into account the burst detection efficiency from the entire sky and were normalized to the same exposure time (one year). To estimate the burst detection efficiency from the entire sky during the GRIF experiment, we used the ratio of the solid angle that characterizes the PX-2 geometric field of view ($\sim$1 sr) to 4π sr. It should be noted that adding the group of short-duration ($\Delta t < 1$ s) bursts does not change the pattern of the distribution, because long-duration events account for most of the GRBs detected during the BATSE/CGRO experiment.

Figure 3 also shows the distributions $N(>kT)$ constructed for various kT_0 using the simplest cosmological model ($\Omega_m = 1$, $\Omega_\Lambda = 0$) in which the source evolution is disregarded (the number of bursts Q formed per unit time in a unit element of the comoving volume does not depend on z). The values of $N(>kT)$ were calculated using relation (3) from $N(<z)$, which were determined from the standard formula that specifies the number of bursts observed in a time interval Δt

$$N(<z) = \int_0^z Q(z')\frac{\Delta t}{(1+z')}\frac{dV}{dz'}dz', \qquad (4)$$

where dV/dz is an element of the comoving volume and Q is the number of bursts formed per unit time in a unit element of the comoving volume (as was pointed out above, we consider a nonevolutional model, i.e., $Q = \text{const}$).

The $N(>kT)$ dependences shown in Fig. 3 were computed for several values of kT_0 (indicated in the figure) and normalized to the number of bursts with durations >1 s observed during the BATSE/CGRO experiment, which corresponds to $z < 0.5$ (under the above assumptions). The detection rate of soft GRBs from the entire sky estimated in the GRIF experiment allows the observed distribution $N(>kT)$ keV to be extended to $kT < 50$ keV. Of course, given the above remarks, this estimate can be considered only as an upper limit of the burst detection rate if the nature of the bursts with $kT < 50$ keV is assumed to be the same as that of the typical GRBs. Note that the GRIF and BATSE/CGRO data on the statistics of typical ($kT > 50$ keV) GRBs with burst fluences $> 10^{-7}$ erg cm^2 are consistent with each other (Kudryavtsev *et al.* 2002). As regards the bursts with $kT \sim 10$–50 keV, their estimated detection rate from the entire sky, as follows from Fig. 3, suggests that the BATSE distribution in the parameter that characterizes the spectral hardness of GRBs may actually reflect their real distribution.

Among the dependences $N(>kT)$ computed in terms of the cosmological model that disregards source evolution, only the dependence obtained for $kT_0 = 500$ keV agrees with the observed distribution. However, such a large value of kT_0 (given that the softest GRBs observed in the BATSE experiment are characterized by $kT \sim 50$ keV) implies that the possible range $z_{\min} < z < z_{\max}$ must correspond to a ratio $(1+z_{\max})/(1+z_{\min}) \sim 10$. However, it can be shown that this z range for the model that disregards evolution is in conflict with the burst distributions in duration and characteristic energy shown in Fig. 2. Indeed, if the spread of bursts in kT and Δt were

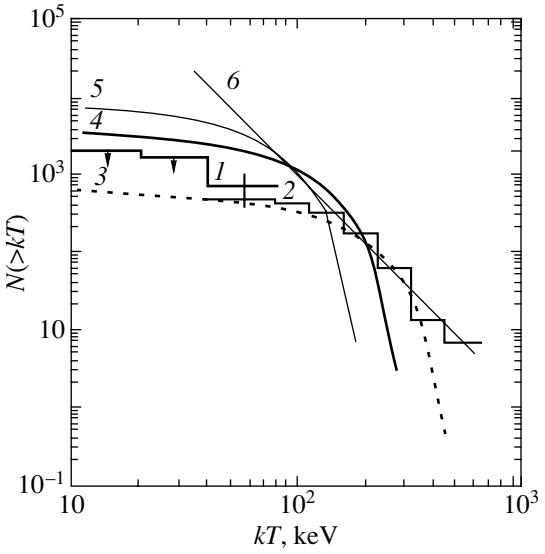

Fig. 3. The integral distribution of astrophysical bursts detected during the GRIF experiment onboard the *Mir* space station (*1*) and long-duration (>1 s) GRBs from the 4B BATSE/CGRO catalog (*2*) in observed characteristic energy kT. The dependences computed in terms of a simple cosmological model ($\Omega_m = 1, \Omega_\Lambda = 0$) with a uniform (in z) burst rate for kT_0 in the source: 500 (*3*), 300 (*4*), and 200 keV (*5*), are also presented. Also shown is the dependence $N \sim kT^{-3}$ (*6*), which fits the distribution ($N > kT$) at large kT.

attributable to the cosmological redshift and dilatation effects alone, then, on average, these parameters would be inversely proportional, which is an obvious consequence of (3) and (4). In addition, the kT and Δt ranges would correspond to each other; i.e., the scales of the relative spread in these quantities would be equal. At the same time, it follows from the observed GRB distributions in kT and Δt (see Fig. 2) that no correlation can be traced between the duration and spectral hardness both for individual groups of bursts and for the entire population of bursts detected in the BATSE and GRIF experiments. It thus follows that the spread in duration and spectral hardness, which could stem from the fact that the sources are located at distances characterized by different z, is overlapped by the dispersion of these parameters in the source. The latter conclusion is also confirmed by the fact that the ranges of observed durations and spectral hardnesses do not correspond to each other by more than three orders of magnitude in duration and about one order of magnitude in spectral hardness. The relative boundaries of the possible range $z_{\min} < z < z_{\max}$ can be determined from the distribution shown in Fig. 2. The relative change in Δt (or kT), determined from (3) and (4), along the anticorrelation straight lines $kT \sim (\Delta t)^{-1}$, which bound the region where GRBs are located in the $kT - \Delta t$ diagram (see

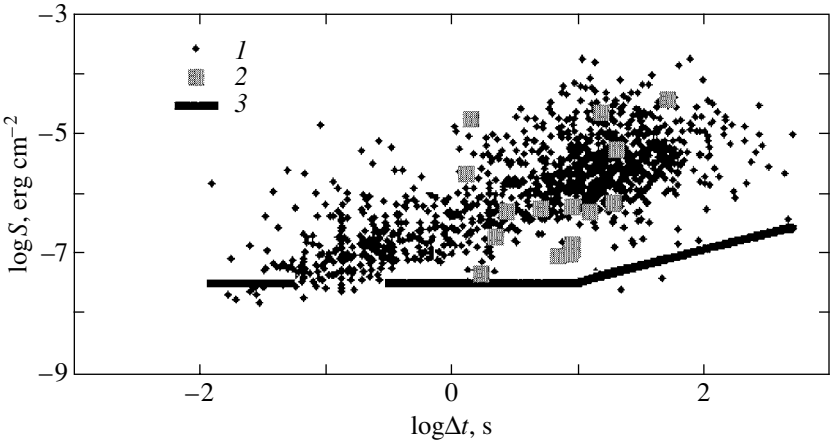

Fig. 4. The two-dimensional fluence–duration diagram constructed from BATSE/CGRO (*1*) and GRIF (*2*) data; *3* is the PX-2 sensitivity threshold in the GRIF experiment.

Fig. 2), can be taken as an upper limit of the ratio $(1+z_{\max})/(1+z_{\min})$. It follows from the figure that, in particular, the long-duration ($\Delta t > 1$ s) bursts lie mostly within the region along the boundaries of which the relative change in kT and Δt is $\sim$3. Thus, the following estimate can be obtained for the z range:

$$\frac{1+z^{\max}}{1+z^{\min}} < 3. \qquad (5)$$

Clearly, estimate (8) does not correspond to the z range obtained in terms of the nonevolutional model with $kT_0 = 500$ keV.

The aforesaid is valid only if the deficit of bursts in the range of low kT (accordingly, high z) is real rather than the result of a limited sensitivity of the experiments. The fact that the GRIF sensitivity is high enough to justify our conclusion that the region of burst sources is limited at high z is illustrated by Fig. 4. This figure shows a two-dimensional diagram that characterizes the distribution of GRBs detected during the BATSE and GRIF experiments in fluence and duration. We see from the figure that for almost the entire group of long-duration ($\Delta t > 1$ s) bursts detected in the BATSE experiment, their fluences lie above the GRIF sensitivity threshold, with the faintest observable bursts in the GRIF experiment having minimum fluences $S \sim 3 \times 10^{-8}$ erg cm^{-2}.

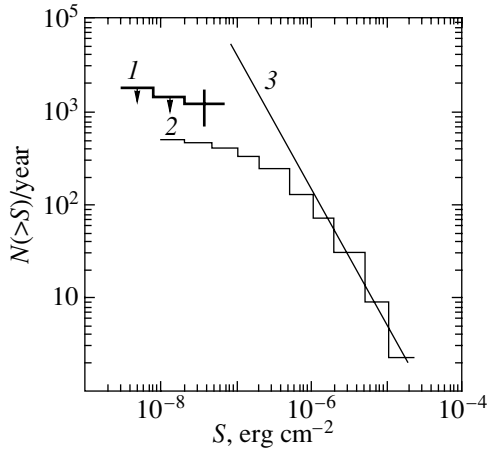

Fig. 5. The integral GRB distribution in fluence S ($\log N - \log S$) for the burst detection rate from the entire sky constructed from PX-2 (*1*) and BATSE/CGRO (*2*) data (long-duration, $\Delta T > 1$ s, bursts) and the dependence $N(>S) \sim S^{-3/2}$, which holds for a uniform spatial distribution of sources (*3*).

Figure 5 shows the fluence distribution ($\log N - \log S$) constructed by including the statistics of soft GRBs. The $\log N - \log S$ distribution constructed from GRIF data was recalculated to the entire sky by using a technique considered in detail previously (Kudryavtsev *et al.* 2002). Note that, as we see from Fig. 4, adding soft GRBs does not fundamentally change the pattern of the $\log N - \log S$ distribution, although this addition allows the distribution to be extended to lower S, down to $\sim 10^{-8}$ erg cm^{-2}. If the fluence distribution is assumed to reflect the spatial distribution of sources, then the spread in observed S is determined by the corresponding z range.

If the deviation of the distribution $N(>S)$ from the dependence $S^{-3/2}$ is assumed to be attributable to the cosmological effects alone, then $z \sim 1$ must correspond to the values of S at which this deviation becomes statistically significant ($\sim 2 \times 10^{-6}$ erg cm^{-2}). According to the standard cosmological relations between the observed fluence and luminosity in the source (Zeldovich and Novikov 1975), the faintest bursts observable in the GRIF experiment with fluences $S \sim 3 \times 10^{-8}$ erg cm^{-2} correspond to $z \sim 20$;

i.e., the GRIF sensitivity margin allows the possible z range given by estimate (5) to be definitely covered.

To summarize, we can say that the cosmological model that disregards source evolution is inconsistent with the experimental distribution $N(>kT)$ for relatively low values of $kT_0(<300$ keV) and the z range predicted by this model is in conflict with the estimate obtained from the combined distribution in kT and Δt for high values of $kT_0 \sim 500$ keV. Thus, there is reason to reject the model that disregards source evolution, which, in turn, leads us to conclude that the GRB rate was, probably, not constant during the evolution of the Universe; i.e., most of the GRBs originated at epochs that corresponded to the limited z range specified by inequality (5). In this case, the GRB distributions in observed duration and spectral hardness are essentially determined by the dispersions of these quantities in the sources.

The absolute boundaries of the z range can be chosen by using data on the direct identification of GRBs with extragalactic objects. The results available to date suggest that the z values for the bursts identified with extragalactic objects lie within the range from $\sim$0.4 to $\sim$4.5; $z \geq 1.0$ for most of the identified bursts (Donaghy *et al.* 2002). Thus, given constraint (5), the following estimate can be obtained for the bulk of the population of GRB sources: $1 < z < 5$. It should be noted that this estimate refers only to the group of long-duration GRBs.

The above estimate matches the range of possible z values obtained by analyzing the nontriggered events detected in the BATSE/CGRO experiment (Kommers *et al.* 2000). In general, this is not surprising, because the main conclusion drawn from the GRIF observations of soft GRBs lies in the establishment of the fact that there is no significant selection at low kT and low fluences in the BATSE data and that the GRBs detected at the BATSE/CGRO sensitivity level probably give an exhaustive sample from the entire population of GRBs. This conclusion is consistent with most of the theoretical models that associate the burst rate with the star-formation history. In these models, the burst rate is highest at z from $\sim$1 to 5 (Lipunov *et al.* 1993; Madau *et al.* 1998; Hughes *et al.* 1998; Rowan-Robinson 1999).

REFERENCES

1. R. L. Aptekar, P. S. Butterworth, T. L. Cline, *et al.*, Astrophys. J. **493**, 404 (1998).
2. R. Barkana and A. Loeb, Phys. Rep. **349**, 125 (2001).
3. A. W. Blain and P. Natarajan, Mon. Not. R. Astron. Soc. **312**, L35 (2000).
4. A. V. Bogomolov, Yu. I. Logachev, M. I. Kudryavtsev *et al.*, Izv. Akad. Nauk, Ser. Fiz. **61**, 1130 (1997).
5. M. S. Briggs, private communication (2002).
6. V. Bromm and A. Loeb, Astrophys. J. **575**, 111 (2002).
7. H. E. Coffey, http//www.ndgc.noaa.gov/stp/SOLAR/getdata.html (2001).
8. E. Costa, F. Frontera, J. Heise, *et al.*, Nature **387**, 783 (1997).
9. T. Donaghy, D. Q. Lamb, D. E. Reichart, and C. Graziani, astro-ph/0210436 (2002).
10. R. C. Duncan and C. Thomson, Astrophys. J. **392**, 9 (1992).
11. D. Eichler, M. Livio, T. Piran, and D. N. Schramm, Nature **340**, 126 (1989).
12. D. A. Frail, S. R. Kulkarni, S. R. Nicastro, *et al.*, Nature **389**, 261 (1997).
13. S. V. Golenetskiĭ, private communication (2002).
14. K. Hurley, P. Li, C. Kouveliotou, *et al.*, Astrophys. J. Lett. **510**, L111 (1999).
15. D. H. Hughes, S. Serjeant, J. S. Dunlop, *et al.*, Nature **394**, 241 (1997).
16. H.-T. Janka, T. Eberl, M. Ruffert, and C. L. Fryer, Astrophys. J. Lett. **527,** L39 (1999).
17. J. M. Kommers, W. H. G. Lewin, C. Kouveliotou, *et al.*, Astrophys. J. **533**, 696 (2000).
18. J. M. Kommers, W. H. G. Lewin, C. Kouveliotou, *et al.*, Astrophys. J., Suppl. Ser. **134**, 385 (2001).
19. T. Koshut, W. S. Pasiesas, C. Kouveliotou, *et al.*, Astrophys. J. **463**, 570 (1996).
20. C. Kouveliotou, C. A. Meegan, G. J. Fishman, *et al.*, Astrophys. J. Lett. **413**, L101 (1993).
21. C. Kouveliotou, G. J. Fishman, C. A. Meegan, *et al.*, Mon. Nature **2**, 72 (1994).
22. C. Kouveliotou, J. Van Paradijs, G. J. Fishman, *et al.*, Nature **379**, 799 (1996).
23. C. Kouveliotou, S. Dieters, T. Strohmayer, *et al.*, Nature **392**, 235 (1998).
24. C. Kouveliotou, T. Strohmayer, K. Hurley, *et al.*, Astrophys. J. Lett. **510**, L115 (1999).
25. M. I. Kudryavtsev and S. I. Svertilov, Pis'ma Astron. Zh. **14**, 216 (1988) [Sov. Astron. Lett. **14**, 90 (1988)].
26. M. I. Kudryavtsev, V. M. Pankov, A. V. Bogomolov, *et al.*, in *Proceedings of the 24th ICRC, Rome, Finito di stampare nel luglio, 1995* (Arti Grafiche Editoriali, Urbino, 1995), Vol. 3, p. 567.
27. M. I. Kudryavtsev, V. M. Pankov, A. V. Bogomolov, *et al.*, Izv. Vyssh. Uchebn. Zaved. Radiofiz. **39**, 1539 (1996).
28. M. I. Kudryavtsev, S. I. Svertilov, and O. V. Morozov, Pis'ma Astron. Zh. **28**, 331 (2002) [Astron. Lett. **28**, 287 (2002)].
29. S. R. Kulkarni, S. G. Djorgovski, D. A. Frail, *et al.*, Nature **393**, 35 (1998).
30. V. M. Lipunov, K. A. Postnov, M. E. Prokhorov, *et al.*, Astrophys. J. **454**, 593 (1995).
31. P. Madau, M. Della Valle, and N. Panagia, Mon. Not. R. Astron. Soc. **297**, L17 (1988).
32. A. I. MacFadyen, S. E. Woosley, and A. Heger, Astrophys. J. **550**, 410 (2001).
33. R. S. Mallozzi, W. S. Paciesas, G. N. Pendleton, *et al.*, Astrophys. J. **454**, 597 (1995).
34. E. P. Mazets, S. V. Golenetskiĭ, V. N. Il'inskiĭ, *et al.*, Astrophys. Space Sci. **80**, 3 (1981).

35. C. A. Meegan, G. N. Pendleton, M. S. Briggs, *et al.*, Astrophys. J., Suppl. Ser. **106**, 65 (1996).
36. I. G. Mitrofanov, Adv. Space Res. **22**, 1077 (1998).
37. J. P. Norris, R. J. Nemiroff, J. D. Scargle, *et al.*, Astrophys. J. **424**, 540 (1994).
38. W. S. Pasiesas, C. A. Meegan, G. N. Pendleton, *et al.*, Astrophys. J., Suppl. Ser. **122**, 465 (1999).
39. W. S. Pasiesas, C. A. Meegan, G. N. Pendleton, *et al.*, Astrophys. J., Suppl. Ser. **122**, 497 (1999).
40. W. S. Pasiesas, C. A. Meegan, G. N. Pendleton, *et al.*, http://www.batse.msfc.nasa.gov/batse/grb/catalog/4b/ (2001).
41. B. Paczynski, Astrophys. J. Lett. **308**, L43 (1986).
42. M. Rowan-Robinson, Astrophys. Space Sci. **266**, 291 (1999).
43. T. Totani, Astrophys. J. Lett. **486**, L71 (1997).
44. T. Totani, Astrophys. J. **511**, 41 (1999).
45. J. Van Paradijs, P. J. Groot, T. Galama, *et al.*, Nature **386**, 686 (1997).
46. G. Vasisht and F. V. Gotthelf, Astrophys. J. Lett. **486**, L129 (1997).
47. R. A. M. J. Wijers, J. S. Bloom, J. S. Bagla, and P. Natarajan, Mon. Not. R. Astron. Soc. **294**, L13 (1998).
48. P. M. Woods, C. Kouveliotou, J. Van Paradijs, *et al.*, Astrophys. J. **517**, 431 (1999).
49. Ya. B. Zel'dovich and I. D. Novikov, *Structure and Evolution of the Universe* (Nauka, Moscow, 1975).

Translated by V. Astakhov

Astronomy Letters, Vol. 29, No. 5, 2003, pp. 289–297. Translated from Pis'ma v Astronomicheskiĭ Zhurnal, Vol. 29, No. 5, 2003, pp. 334–342.

Correlation Properties of the Galaxies in the Local Supercluster

A. V. Tikhonov[1] and D. I. Makarov[2*]

[1] *Astronomical Institute, St. Petersburg State University, Universitetskii pr. 28, St. Petersburg, 198504 Russia*

[2] *Special Astrophysical Observatory, Russian Academy of Sciences, Nizhnii Arkhyz, 369167 Russia*

Received October 28, 2002

Abstract—The apparatus of a correlation gamma function is used to analyze the spatial clustering of galaxies in the Local Supercluster. In particular, we analyzed a sample corrected for the peculiar velocities of the Local Supercluster galaxies by using our original technique for separating groups of galaxies. It turned out that the peculiar velocities did not significantly distort the gamma function even for relatively small sample sizes. The distribution of the galaxies obeys a power-law decrease in density with an index of 0.6–0.7. We found evidence for a luminosity dependence of the degree of galaxy clustering within the volume under study. © *2003 MAIK "Nauka/Interperiodica"*.

Key words: *galaxies, groups and clusters of galaxies, intergalactic gas.*

INTRODUCTION

Galaxy clustering is observed over a wide range of scales. Describing the form and amplitude of the clustering of matter on all of the observable scales is of great importance in reproducing the initial conditions that led to the observed variety of structures in the course of evolution.

Tikhonov *et al.* (2001) showed that a power-law decrease of the correlation gamma function with an index of 0.9–1.5 (different for different objects) is observed in a wide range of scales, from 30 kpc (the size of a large galaxy) to 30–40 Mpc. On these scales (30–40 Mpc), the gamma function constructed from various samples of galaxies and clusters exhibits a break. This break implies a change in the clustering regime: the scales of a more uniform distribution of the luminous matter are reached. The results were obtained from various independent samples of galaxies, clusters, and superclusters.

Here, we restricted our study to a sample of galaxies of the Local Superclaster to trace the pattern of change in the correlation properties of the distribution of galaxies within an individual cluster—a structure that is definitely within a uniformity cell. As is well known, because of the large peculiar velocity dispersion of the cluster galaxies, the cluster turns out to be highly elongated along the radial coordinate (the so-called "God's fingers" on the survey maps of galaxies). This observational effect distorts the correlation properties of the galaxy distribution in space. We can solve this problem and estimate the extent to which God's fingers affect the correlation pattern of the entire distribution by separating groups of galaxies (according to a certain criterion) from a galaxy sample distorted by significant peculiar velocities.

DESCRIPTION OF THE LOCAL SUPERCLUSTER

John Herschel was the first to describe what we now call the Local Supercluster. He suggested that the observed concentration of nebulas forms a spherical system centered on Virgo and that our Galaxy is one of the peripheral members of this system. De Vaucouleurs (1953, 1958) was the first to suggest that the observed concentration is a real spatial structure in the distribution of galaxies. By analogy with the distribution of stars in disk galaxies, he called this structure a Supergalaxy and later changed the name to the Local Supercluster (de Vaucouleurs 1958), which has been used until now.

Numerous studies (Tully and Fisher 1987; Lahav *et al.* 2000) showed that the Local Supercluster is a filamentary structure that extends to more than $40h^{-1}$ Mpc and is roughly centered on the Virgo cluster of galaxies. Galaxies are concentrated into several clusters (the most prominent of which are Virgo, Ursa Major, and Fornax), groups, and filaments, which outline nearby voids. The Local Group lies on the outskirts of the Supercluster in a small filament that extends from Fornax to Virgo. Figure 1 shows the sky distribution of Local Supercluster galaxies. A complex peculiar velocity field is observed inside the Local Supercluster. This field is inconsistent with the simple model of a spherically symmetric fall of matter to

*E-mail: dim@sao.ru

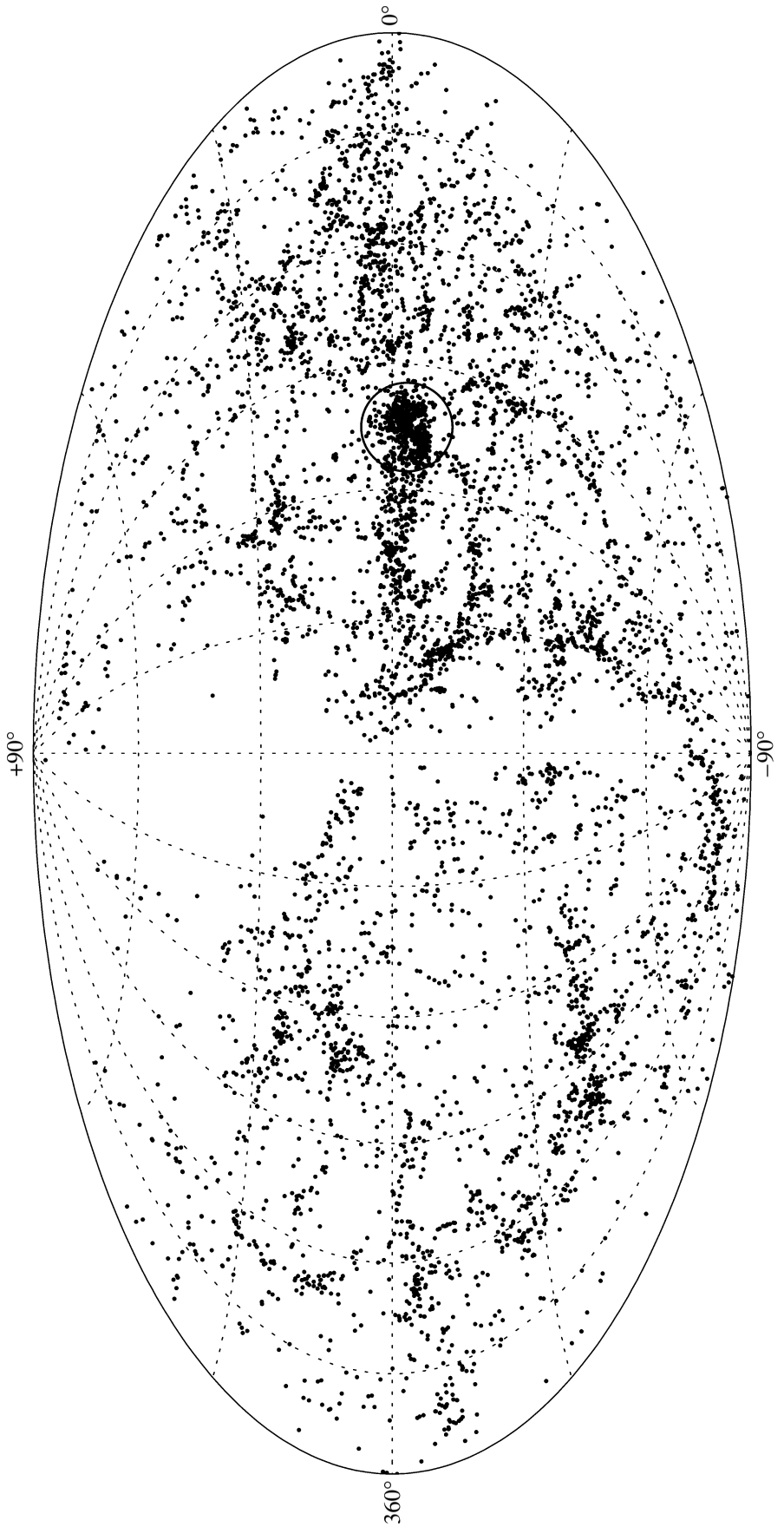

Fig. 1. The distribution of Local Supercluster galaxies (with velocities lower than 3000 km s^{-1}) in Supergalactic coordinates. The Virgo cluster of galaxies is marked. A concentration of galaxies toward the Supercluster plane is clearly seen.

the Virgo cluster (Karachentsev and Makarov 2001). Currently available numerical simulations of the Local Supercluster (Cen 1994; Klypin *et al.* 2001) lead us to the same conclusion. Therefore, the validity of using the correction of the line-of-sight velocities of galaxies for their fall to the Virgo cluster is called into question and we did not apply this correction here.

Enormous density contrasts, ranging from the concentration of galaxies at the Supercluster center to their absence in the Local Void, are observed in the volume of the Local Supercluster.

THE PROCEDURE FOR CONSTRUCTING A SAMPLE OF GALAXY GROUPS

Makarov and Karachentsev (2000) compiled a catalog of groups of galaxies in the Local Supercluster using the new group separation criterion suggested by Karachentsev (1994). The group separation algorithm is based on the condition that the total energy for a physical pair of galaxies is negative.

This condition can be written as the ratio of the kinetic and gravitational energies

$$\frac{T}{\Omega} = \frac{V^2 R}{2G\sum \mathfrak{M}} < 1, \qquad (1)$$

where R is the spatial distance between the galaxies, V is the space velocity difference, $\sum \mathfrak{M}$ is the total mass of the galaxies, and G is the gravitational constant.

However, because of projection effects, this condition does not allow false pairs with a small line-of-sight velocity difference to be excluded from the catalog. Therefore, condition (1) should be supplemented with the condition of a maximum possible distance between the galaxies at which they can still be considered to be a gravitationally bound system. The so-called zero-velocity surface that separates the volume of gravitational contraction from the expanding space (the Hubble flow) (Sandadge 1986) is such a natural boundary. In the spherically symmetric case, this condition can be written as

$$\frac{\pi^2 R^3 H^2}{8G\sum \mathfrak{M}} < 1, \qquad (2)$$

where H is the Hubble constant.

The procedure for group separation consisted of several steps. First, pairs that satisfied criteria (1) and (2) were selected. Next, pairs with common galaxies were combined into groups. And, finally, groups were merged if their centers were a gravitationally bound pair.

We estimated the masses of the galaxies from their luminosities by taking into account the dependence of the mass/luminosity ratio on galaxy type. The total galaxy mass was determined from the formula

$$\mathfrak{M} = \kappa \mathfrak{M}_{25}, \qquad (3)$$

where $1/\kappa$ is the proportionality coefficient between the total mass and that contained within the standard galaxy radius $\mathfrak{M}_{25}$ (Hoffman *et al.* 1996; Broelis and Rhee 1997).

The algorithm described above was applied to a sample of galaxies from the LEDA database (Paturel *et al.* 1996) supplemented with recent observations. We selected galaxies with velocities $V_{\rm LG} < 3000$ km s^{-1} relative to the Local Group centroid. We also excluded the "zone of avoidance" of the Milky Way $|b| < 10^\circ$.

The final list contained data for 6321 galaxies.

We corrected the apparent magnitudes of the galaxies for Galactic extinction by using new IRAS/DERBE maps (Schlegel *et al.* 1998). All photometric corrections (with an allowance made for absorption and the inclination of the galaxy to the line of sight) were made in the same way as that adopted in the LEDA database (Paturel *et al.* 1996). We reduced the line-of-sight velocities of the galaxies to the apex determined by Karachentsev and Makarov (1996) and used the Hubble constant $H_0 = 70$ km s^{-1} Mpc^{-1}.

As a result, we separated 839 groups containing 3472 galaxies, which account for 55% of the sample of galaxies under study.

A DESCRIPTION OF THE CORRELATION GAMMA FUNCTION

The correlation gamma function or the conditional density function (Pietronero *et al.* 1988; Coleman and Pietronero 1992) was used mostly in statistical physics to analyze structures with large-scale density correlations and scale invariance (fractality). Pietronero with colleagues (Sylos Labini *et al.* 1996a, 1996b, 1998; Montuori *et al.* 1997) were the first to use this function to study the spatial distribution of galaxies and clusters.

The essence of calculating the gamma function is to measure the variation of the mean sample density with distance (volume). The differential ($\Gamma(r)$) and integral ($\Gamma^*(r)$) gamma functions for a given r are defined by the formulas

$$\Gamma(r) = \frac{1}{N}\sum_{i=1}^{N} \frac{1}{4\pi r^2 \Delta} \int_r^{r+\Delta} n(r_i - r')dr', \qquad (4)$$

$$\Gamma^*(r) = \frac{1}{N}\sum_{i=1}^{N} \frac{3}{4\pi r^3} \int_0^{r} n(r_i - r')dr', \qquad (5)$$

where $n(r) = \frac{1}{\tilde{N}} \sum_{i=1}^{\tilde{N}} \delta(r_i - r)$ is the number density; N is the number of sample objects involved in the calculations as the centers of spheres; $\tilde{N}$ is the number of objects in the sample; $\tilde{N}$ is constant, whereas N varies with r (see below for a description of the algorithm); and Δ is the thickness of the spherical layer (it is assumed to be small in the definition and finite in practice: $\Delta = 0.3$–4 Mpc, depending on the sample).

The integral function ($\Gamma^*(r)$) averages the contributions from different scales. Therefore, if the distribution exhibits monofractal properties (Feder 1988), it smoothes the fluctuations and allows the dimension of the distribution to be measured more accurately than does the differential gamma function. At the same time, the integral function is characterized by inertia—it is moderately sensitive to changes of the distribution type. The differential function reveals the change of the distribution type better than the integral function does. In this sense, it is more informative, but at the same time is more prone to fluctuations.

In contrast to the widely used two-point correlation function (ξ function), the gamma function is calculated without any a priori assumptions about the universal mean density and the distribution of objects beyond the geometrical boundaries of the sample. In the volume of the Local Supercluster, we definitely have a sample in which the universal mean matter density in the Universe cannot be measured. Consequently, the mean density cannot be used explicitly or implicitly (as is done in calculations with various modifications of the two-point correlation function) for a practical implementation of the computational algorithm. Besides, the results of ξ analysis significantly depend on how the problem of the sample boundaries is solved and on selection effects.

The gamma-function algorithm was first suggested as an alternative to the ξ function. The authors abandoned the selection function (Coleman and Pietronero 1992), which was used to fill sample regions far removed in radial coordinate with a systematically underestimated population of faint galaxies. Gamma-analysis is performed only within the geometrical boundary of a homogeneous sample.

Thus, in studying the clustering of galaxies in the volume that we chose, reliable information can be obtained by the gamma-function method.

CONSTRUCTING A WORKING VOLUME-LIMITED SAMPLE

After separating galaxy groups, we assigned equal coordinates and distances to their constituents. A group of galaxies is not involved in our analysis on equal footing with an isolated galaxy—we perform a kind of weighing (the population of the group affects its contribution to the calculations). This procedure will lead to the total loss of information on the distribution of galaxies in each group, but at the same time, the form of the correlation function will not be distorted by God's fingers. We added isolated galaxies, i.e., galaxies that were not included in groups, to the resulting sample.

Based on the positions of the galaxies in Fig. 2, which shows the absolute magnitude–distance ($M_{\rm abs} - R$) diagram, we chose the following sample parameters: the radial boundary $R_{\rm lim} = 43h^{-1}$ Mpc and the minimum absolute magnitude for an object to be included in the working sample, $M^0_{\rm abs} = -17\overset{m}{.}5$. Thus, only objects from the total list with $M_{\rm abs} < M^0_{\rm abs}$, i.e., those brighter than the faintest and most distant object of the sample with an absolute magnitude $M^0_{\rm abs}$, remain in the sample. This ensures that the sample is homogeneous in luminosity (any other sample object is seen from each object).

In our analysis, we divided the list into two parts, northern and southern, in Galactic latitude $|b_{\rm gal}| = 10^\circ$.

RESULTS

Results of the Gamma Statistics

(1) The northern ($b_{\rm gal} > 10^\circ$) sample contains 2646 galaxies brighter than $M_{\rm abs} < -17\overset{m}{.}5$ in the B band. On small scales up to $\approx 3.2h^{-1}$ Mpc (Fig. 3a), the information on the correlation properties of the sample is distorted by virial motions inside the groups and clusters. On larger scales, the density shows a power-law decrease with a slope of 0.56 ± 0.01 (where $\sigma = 0.01$ is the error of the linear fit) up to $20h^{-1}$ Mpc, i.e., up to the statistical significance limit of the sample determined by the gamma-function algorithm.

(2) The southern ($b_{\rm gal} < -10^\circ$) part of the sample also exhibits a density decrease up to $20h^{-1}$ Mpc with a slope of 0.70 ± 0.03 (Fig. 3b). In the southern part, the combination of galaxies into groups completely leveled out the small-scale correlations up to $2.5h^{-1}$ Mpc.

The case without galaxy grouping shows a well-defined power-law dependence of the density on distance in the entire range of our calculations.

(3) The northern part of the sample without galaxy grouping shows a power-law density decrease with a slope of 0.75 ± 0.02 also in the entire range of our gamma-function calculations and a slope of 0.64 ± 0.01 when fitted in the range $(3$–$20)h^{-1}$ Mpc, i.e., as in case 1 (Fig. 4a).

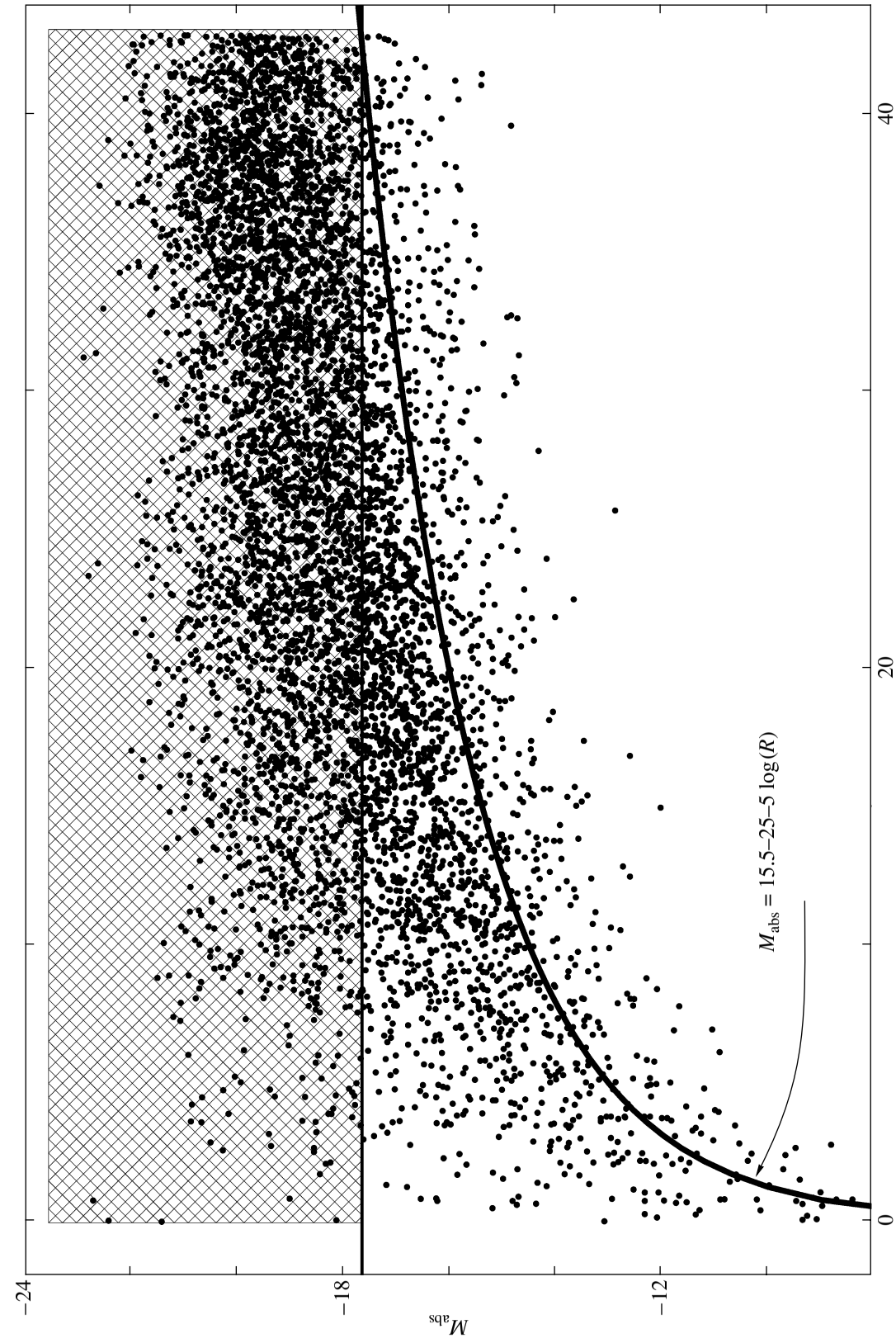

Fig. 2. Constructing a volume-limited sample for the Local Supercluster galaxy survey to an apparent magnitude of $m_{lim} = 15^m.5$.

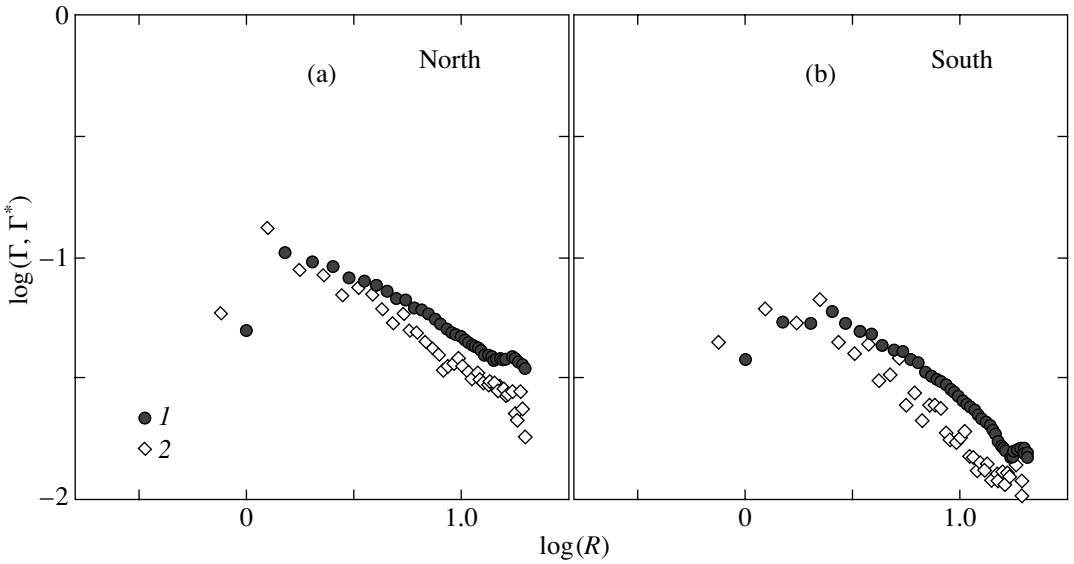

Fig. 3. The gamma function for Local-Supercluster galaxies with group separation. The variations of the integral (*1*) and differential (*2*) gamma functions are shown: (a) the northern part, $N = 2656$, $R_s = 20h^{-1}$ Mpc; (b) the southern part, $N = 1341$, $R_s = 21h^{-1}$ Mpc.

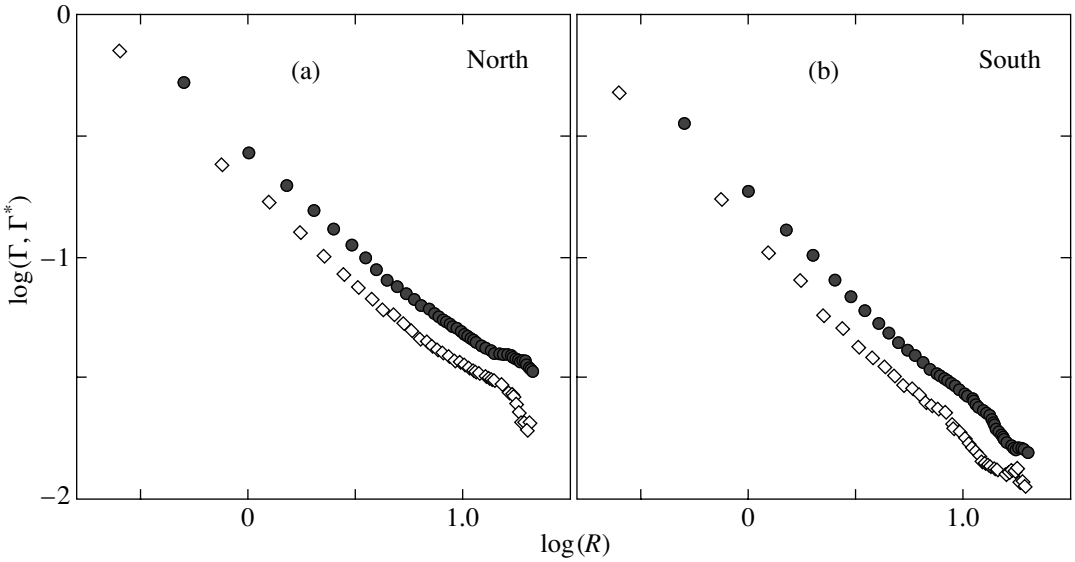

Fig. 4. The gamma function for the uncorrected sample of Local-Supercluster galaxies: (a) the northern part, $N = 2656$, $R_s = 20h^{-1}$ Mpc; (b) the southern part, $N = 1338$, $R_s = 21h^{-1}$ Mpc. The notation is the same as in Fig. 3.

(4) The southern part of the uncorrected sample of the Local-Supercluster volume shows a slope of 0.84 ± 0.02 for the entire range of our gamma-function calculations and a slope of 0.80 ± 0.01 for the ranges of scales corresponding to case 2 (Fig. 4b).

Note that starting from the characteristic scale determined by the velocity dispersion in groups of galaxies, the gamma functions for the northern and southern samples with separated groups are virtually identical to those constructed from the corresponding samples uncorrected for peculiar velocities. Thus, the distortion of the three-dimensional pattern by peculiar velocities is significant only up to a scale of $(3–4)h^{-1}$ Mpc. Since the maximum velocity dispersion in small groups of Local-Supercluster galaxies is 287 km s^{-1} (Makarov and Karachentsev 2000), one might expect the distortions of the density field due to the virial motions of galaxies inside groups to have an effect up to scales of $\sim$4 Mpc. Nevertheless, our result (the form of the gamma function) is not so obvious.

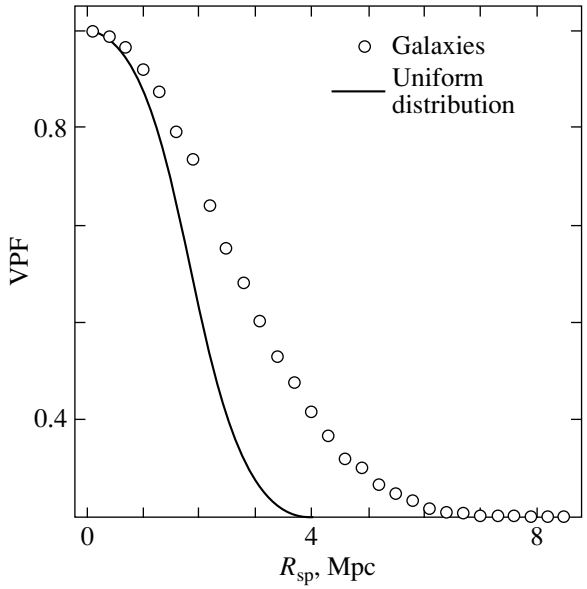

Fig. 5. The function VPF constructed for the northern part of the sample with separated groups of Local-Supercluster galaxies and for a random realization: $N = 2656$ and R_{sp} is the radius of the sphere.

The gamma function is an integrated characteristic of the volume, and the fact that this function is not distorted on scales larger than the characteristic velocity dispersion of the galaxies in groups is of great methodological importance in selecting regions to which the gamma statistics can be applied.

The observed difference between the conditional probability amplitudes for the northern and southern samples is determined by the different numbers of galaxies of the corresponding sky regions. The number of galaxies within our geometrical boundaries of the galaxy samples in the southern hemisphere is approximately half that in the northern hemisphere. This is because our Galaxy is located on the outskirts of the Local Supercluster, virtually in its plane, and most of the Local-Supercluster galaxies are located in the northern sky (see Fig. 1).

Constructing the Void Probability Function

The void probability function (VPF) (Borgani 1995) underlies the technique for studying voids. It belongs to the category of methods for studying the general characteristics of galaxy-free regions, as distinct from the methods used to study the morphology of particular voids. The VPF measures the probability $P_0(V)$ that a sphere placed at random within the geometrical sample boundaries will contain none of the sample galaxies. For a point Poisson process (a completely uncorrelated distribution), $P_0(V) = \exp(-nV)$, where n is the galaxy number density. Deviations of $P_0(V)$ from this law indicate a clustering of the sample.

We used the VPF in this rigorous version of the void criterion (the complete absence of galaxies within the sphere), because some of the Local-Supercluster regions were analyzed in detail to search for dwarf galaxies that belong to groups or surround them.

The VPF constructed for the northern part of the sample with separated groups differs significantly from the VPF constructed for a uniform distribution in the same region, thereby confirming (independently of the gamma analysis) that the distribution of galaxies in the Local Supercluster is essentially nonuniform (Fig. 5).The mean distance between the objects in this volume is $D_{mean} = (V/N)^{1/3} = 3.73h^{-1}$ Mpc. It determines the maximum scale of the spheres con-

Parameters of the gamma function for various luminosity-limited samples of Local-Supercluster galaxies

M_{abs}	North		South	
	N	γ	N	γ
−17.5	2656	0.56	1341	0.70
−18.0	2286	0.54	1145	0.73
−18.5	1847	0.56	947	0.71
−19.0	1406	0.61	730	0.66
−19.5	950	0.64	534	0.68
−20.0	569	0.68	324	0.73
−20.5	298	0.90	189	0.80

taining no sample objects that can be placed in the sample obtained by using a random distribution of the same mean density as the galaxy sample. This scale is slightly larger than the mean distance (see the VPF in Fig. 5 constructed for a random realization). In contrast, empty spheres with a radius of up to $9h^{-1}$ Mpc can be accommodated in the actual sample.

The mean distance between objects completely characterizes a uniform distribution. At the same time, it says almost nothing about the correlated distribution of galaxies that we have in the Local Supercluster sample.

The Gamma-Function for Various Luminosity-Limited Samples of Local-Supercluster Galaxies

To determine how the slope of the gamma function and, accordingly, the clustering of objects changes as one passes to more luminous galaxies within the sample volume, we performed a gamma analysis for the northern and southern parts of the sample with galaxy grouping for various limiting absolute magnitudes of the galaxies in the same volume (up to $43h^{-1}$ Mpc) starting from $M_{\rm lim} = -17^m.5$ for the volume-limited sample. The results of our calculations are given in the table.

The largest error of the linear fit is $\sigma_\gamma = 0.04$. Since the samples constructed in this way overlap in the brightest galaxies, they are not completely independent.

We may conclude that the variations in the slope of the gamma function for galaxies with luminosities lower than $M_{\rm abs} \approx -20^m$ are insignificant. The slope of the gamma function for the brightest galaxies in the volume ($M_{\rm abs} < -20^m.5$) varies significantly, suggesting that the galaxies in the Local Supercluster are segregated in luminosity. It thus follows that bright galaxies are clustered more strongly than faint galaxies and that low-luminosity galaxies exhibit the same type of distribution. Unfortunately, the gamma function for brighter galaxies is difficult to measure because of the poor statistics. Remarkably, an abrupt change in the slope as one passes to brighter galaxies is observed at $M_{\rm abs}$ close to the characteristic magnitude M^* in the galaxy luminosity function. This conclusion is consistent with the results of the studies in which the segregation of galaxies by luminosity was reported (see, e.g., Guiricin *et al.* 2001).

CONCLUSIONS

(1) The distribution of Local-Supercluster galaxies is nonuniform in the entire sample volume. There is a power-law decrease in density with increasing distance from the sample galaxies. The formal fractal dimensions for the northern and southern parts are $D \approx 2.4$ and $D \approx 2.3$, respectively. These values are larger than those for nearby (<7 Mpc) galaxies of the Local Volume ($D \approx 1.8$; Tikhonov *et al.* 2001), which implies a weaker clustering of objects in the volume up to $43h^{-1}$ Mpc and corresponds to the fraction of the empty space in the Local Volume and the Local-Supercluster volume (the fraction of the galaxy-free space is much larger in the immediate vicinity of our Galaxy).

(2) More luminous and, generally, more massive galaxies are clustered more strongly than less luminous galaxies. Galaxies fainter than $M_{\rm abs} \approx -20^m$ show the same type of distribution. A segregation in luminosity arises for galaxies brighter than $M_{\rm abs} \approx -20^m.5$.

(3) Using information on the groups of galaxies does not significantly change the results of the gamma analysis for the northern and southern samples. This implies that the velocity dispersion in clusters has no significant effect on the results for the galaxy samples covering larger volumes (e.g., CfA2 and SSRS2) either.

ACKNOWLEDGMENTS

We are grateful to I.D. Karachentsev for his attention to this work and for helpful remarks. This work was supported in part by the Ukrainian State Foundation for Basic Research, project no. F7/267-2001.

REFERENCES

1. S. Borgani, Phys. Rep. **251**, 1 (1995).
2. A. H. Broelis and M. H. Rhee, Astron. Astrophys. **324**, 877 (1997).
3. R. Cen, Astrophys. J. **424**, 22 (1994).
4. P. H. Coleman and L. Pietronero, Phys. Rep. **213**, 311 (1992).
5. G. de Vaucouleurs, Astron. J. **58**, 30 (1953).
6. G. de Vaucouleurs, Astron. J. **63**, 253 (1958).
7. B. Feder, in *Fractals in Physics*, Ed. by R. Pietronero and E. Tosatti (North-Holland, Amsterdam, 1986; Mir, Moscow, 1988).
8. G. Giuricin, S. Samurovic, M. Girardi, *et al.*, Astrophys. J. **554**, 857 (2001).
9. G. L. Hoffman, E. E. Salpeter, B. Farhat, *et al.*, Astrophys. J., Suppl. Ser. **105**, 269 (1996).
10. I. D. Karachentsev, Astron. Astrophys. Trans. **6**, 1 (1994).
11. I. D. Karachentsev and D. I. Makarov, Astron. J. **111**, 794 (1996).
12. I. D. Karachentsev and D. I. Makarov, Astrofizika **44**, 5 (2001).
13. A. Klypin, Y. Hoffman, A. V. Kravtsov, and S. Gottlober, astro-ph/0107104 (2001).

14. O. Lahav, B. X. Santiago, A. M. Webster, *et al.*, Mon. Not. R. Astron. Soc. **312**, 166 (2000).
15. D. I. Makarov and I. D. Karachentsev, Astron. Soc. Pac. Conf. Ser. **209**, 40 (2000).
16. M. Montuori, F. Sylos Labini, and A. Amici, astro-ph/9705123 (1997).
17. G. Paturel, L. Bottinelli, H. Di Nella, *et al.*, Catalogue of Principal Galaxies: PGC-ROM, Saint-Genis Laval, Observatoire de Lyon, 1996.
18. L. Pietronero, A. Erzan, and C. Everts, Phys. Rev. Lett. **61**, 861 (1988).
19. A. Sandage, Astrophys. J. **307**, 1 (1986a).
20. D. J. Schlegel, D. P. Finkbeiner, and M. Davis, Astrophys. J. **500**, 525 (1998).
21. F. Sylos Labini, L. Pietronero, and M. Montuori, Physica A **226**, 195 (1996b).
22. F. Sylos Labini, L. Pietronero, and M. Montuori, astro-ph/9701156 (1996).
23. F. Sylos Labini, M. Montuori, and L. Pietronero, Phys. Rep. **293**, 61 (1998).
24. R. B. Tully and J. R. Fisher, *Atlas of Nearby Galaxies* (Cambrige Univ., Cambrige, 1987).
25. A. V. Tikhonov, D. I. Makarov, and A. I. Kopylov, Bull. Spets. Astrofiz. Obs. **50**, 39 (2001).

Translated by A. Dambis

Astronomy Letters, Vol. 29, No. 5, 2003, pp. 298–303. Translated from Pis'ma v Astronomicheskiĭ Zhurnal, Vol. 29, No. 5, 2003, pp. 343–338.

Soft X-ray Sources at the Centers of the Elliptical Galaxies NGC 4472 and NGC 4649

D. A. Soldatenkov*, A. A. Vikhlinin, and M. N. Pavlinsky

Space Research Institute, Russian Academy of Sciences, Profsoyuznaya ul. 84/32, Moscow, 117810 Russia

Received December 20, 2002

Abstract—Analysis of recent observations of the elliptical galaxies NGC 4472 and NGC 4649 with the Chandra X-ray space telescope has revealed faint soft X-ray sources at their centers. The sources are located at the galactic centers, to within 1″, and are most likely associated with the radiation from the supermassive black holes that are assumed to be at the optical centers of these galaxies. Interest in these and several other similar objects stems from the unusually low luminosity of the supermassive black hole embedded in a dense interstellar medium. The sources have soft energy spectra in the Chandra energy range 0.2–10 keV. The source is detected at a 3σ confidence level only in the range 0.2–0.6 keV with a luminosity of $\sim 6 \times 10^{37}$ erg s^{-1} in NGC 4649 and in the range 0.2–2.5 keV with a luminosity of $\sim 1.7 \times 10^{38}$ erg s^{-1} in NGC 4472. © *2003 MAIK "Nauka/Interperiodica"*.

Key words: *elliptical galaxies NGC 4472 and NGC 4649, supermassive black holes, X-ray radiation, Chandra telescope.*

INTRODUCTION

Supermassive black holes, whose masses in massive galaxies can reach $\sim 10^8$–$10^{10} M_\odot$, are currently assumed to be at the centers of many galaxies. This assumption is observationally confirmed by numerous studies of the stellar dynamics in central galactic regions (see, e.g., Magorrian *et al.* 1998; Gebhardt *et al.* 2000; Kormendy and Richstone 1995). According to these studies, the measured stellar velocity dispersions at the centers of most galaxies are too high and can be explained by the existence of supermassive black holes. Being embedded in a dense medium, these objects must actively accrete the surrounding material, resulting in a considerable luminosity of the central galactic region. Quasars, blazars, and radio galaxies are believed to be different manifestations of the activity of the central supermassive black hole.

The dilemma known for several years is that, despite the predicted tremendous masses of the black holes at the galactic centers, the relatively high density of the interstellar matter at the galactic center, and, accordingly, the high accretion rate, the luminosities of the nuclei of many galaxies are many orders of magnitude lower than those predicted by standard disk accretion models. For instance, in the elliptical galaxies NGC 4472 and NGC 4649 discussed below, optical observations indicate the existence of black holes with masses $\sim 3 \times 10^9 M_\odot$ and $\sim 4 \times 10^9 M_\odot$, respectively (Magorrian *et al.* 1998). The luminosity of the nuclei of these galaxies calculated using the formula of Bondi (1952) with a 10% efficiency of energy release of the total accreted mass and with the parameters of the interstellar medium derived below is $\sim 5 \times 10^{44}$ erg s^{-1} for NGC 4472 and $\sim 7 \times 10^{44}$ erg s^{-1} for NGC 4649. Actually, however, the luminosities of the nuclei of these galaxies are much lower.

X-ray observations of these galaxies with the ROSAT telescope (Irwin and Sarazin 1996; Trinchieri *et al.* 1997) and their optical observations with the Hubble Space Telescope (Byun *et al.* 1996) found no evidence of activity of the central source whatsoever. Radio observations (Condon *et al* 1991; Wrobel 1991) provide the only evidence of galactic nuclear activity. They revealed radio sources at the centers of these galaxies and radio lobes in the galaxy NGC 4472.

There are theoretical models that explain such a low luminosity of the accreting black holes in galaxies with low-luminosity nuclei: the model with an advection-dominated accretion flow (Narayan and Yi 1995a, 1995b; Abramowicz *et al.* 1995) and the model with a convection-dominated accretion flow (Narayan *et al.* 2000; Quataert and Gruzinov 2000). The strictest predictions of these models refer to the radio and X-ray ranges, in which the theory is tested observationally (Di Matteo *et al.* 1999). Therefore, of considerable interest are the data that

*E-mail: sold@hea.iki.rssi.ru

have recently been obtained with the Chandra X-ray space telescope, which appreciably surpasses the preceding ROSAT and ASCA X-ray telescopes in its parameters.

Here, we analyze the data obtained with the Chandra telescope, which detected faint soft X-ray sources at the centers of the massive elliptical galaxies NGC 4472 and NGC 4649. The most plausible interpretation of the nature of these sources is a manifestation of the activity of the central black hole. To all appearances, this is the first observation of X-ray radiation from supermassive black holes that are embedded in a relatively dense interstellar medium and that are in quiescence.

DATA ANALYSIS

To analyze the image of the galaxy NGC 4472, we used the observations carried out on June 12, 2000, with an exposure of ~40 000 s and data of the same duration obtained on April 20, 2000, for the galaxy NGC 4649. The ACIS S3 detector was used in all observations. Our exposures were corrected with an allowance made for the most recent calibration data. Subsequently, we applied a filtering procedure, which rejected most of the events associated with charged particles. We also corrected the effective area of the ACIS S3 detector by taking into account the degradation of the quantum efficiency of the instrument, which is particularly pronounced at energies below 1 keV.[1]

During the observations, we recorded an enhancement of the charged-particle background with a duration of ~7000 s for NGC 4472 and ~8000 s for NGC 4649. The bulk of the charged-particle flux was removed by the filtering procedure. However, the remaining flux during the background enhancement can be comparable to the total photon flux from the observed galaxies. Since below we are concerned only with a small region in the central, bright part of the galaxy, the background enhancement will in no way affect the results of our measurements.

At low energies, the Chandra angular resolution deteriorates from 0.5″ to ~1″. Since one pixel on the ACIS S3 detector corresponds to 0.5″, faint soft X-ray sources are most noticeable when the image is grouped twice. Accordingly, the size of one image pixel becomes 1″. The subsequent analysis was carried out only for such images.

In the Chandra energy range (0.2–10 keV), the radiation from elliptical galaxies is mainly attributable to the thermal radiation from a hot interstellar gas. The radiation from low-mass binary systems with a compact object gives a smaller contribution. In addition, the radiation from an active central supermassive black hole can be observed; it can be comparable to all of the remaining radiation from the galaxy. In the galaxies NGC 4472 and NGC 4649 under study, the gas radiation is symmetric relative to the galactic center (Fig. 1) and no typical manifestations of the galactic nuclear activity are observed, although there is a small displacement of the central, bright region of galactic gas in NGC 4472 to the north from the optical center of the galaxy.

Our subsequent analysis of the radiation from the central galactic regions is performed in the energy ranges 0.2–0.6, 0.6–1.2, 1.2–2.5, and 2.5–10 keV. This breakdown of the energy range is explained by different contributions from different interstellar gas radiation mechanisms. In the first and third ranges, bremsstrahlung and free–bound transitions on ions of heavy elements mainly contribute to the gas radiation. In the second range, bound–bound transitions on ions of heavy elements mainly contribute to the spectrum. The bulk of the interstellar gas radiation at a temperature $T \sim 1$ keV is accounted for precisely by these lines in the range 0.6–1.2 keV. In the fourth range 2.5–10 keV, there is virtually no interstellar gas radiation.

Analyzing the brightness profiles in the ranges 0.2–0.6, 0.6–1.2, and 1.2–2.5 keV (Fig. 2), we can conclude that there is a faint soft X-ray source with an angular size of ~1″ at the galactic centers. Indeed, the brightness profile of the interstellar gas in the ranges 0.6–1.2 and 1.2–2.5 keV is well described by the so-called beta model (Cavaliere and Fusco-Femiano 1976):

$$I(r) = \frac{I_0}{(1 + r^2/r_c^2)^{3\beta-0.5}}, \qquad (1)$$

where I_0 is the surface brightness at the galactic center, β and r_c are some parameters of the fit, and r is the distance to the galactic center. For a spherically symmetric gas distribution, the gas density and surface brightness are uniquely related. Consequently, the gas surface brightness in the range 0.2–0.6 keV is also described by model (1) and the peak in the brightness profile at the galactic center is not associated with the gas radiation.

However, we can assume that the gas brightness profile is described not by model (1) but by a similar model with a pronounced peak at the galactic center. The peaks observed at the galactic center in the range 0.6–1.2 keV are then not attributable to the radiation from the central object but represent ordinary interstellar gas radiation. In this case, the absence of a central peak in the range 0.6–1.2 keV can be explained by the resonant scattering of radiation by

[1] asc.harvard.edu/cal/Links/Acis/acis/Cal.prods/qeDeg/index.html

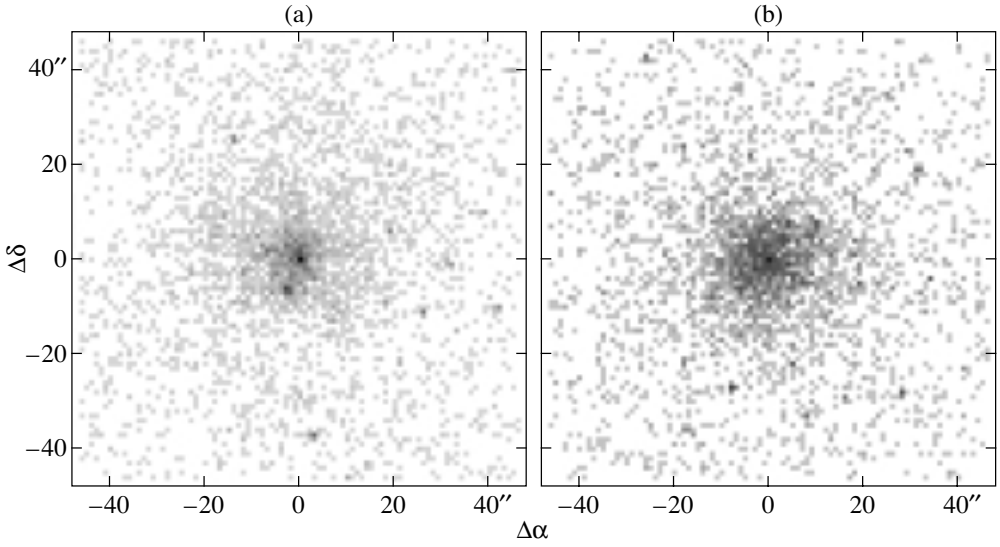

Fig. 1. Detector images of the galaxies NGC 4472 (a) and NGC 4649 (b) in the range 0.2–0.6 keV. The image pixel size is 1″.

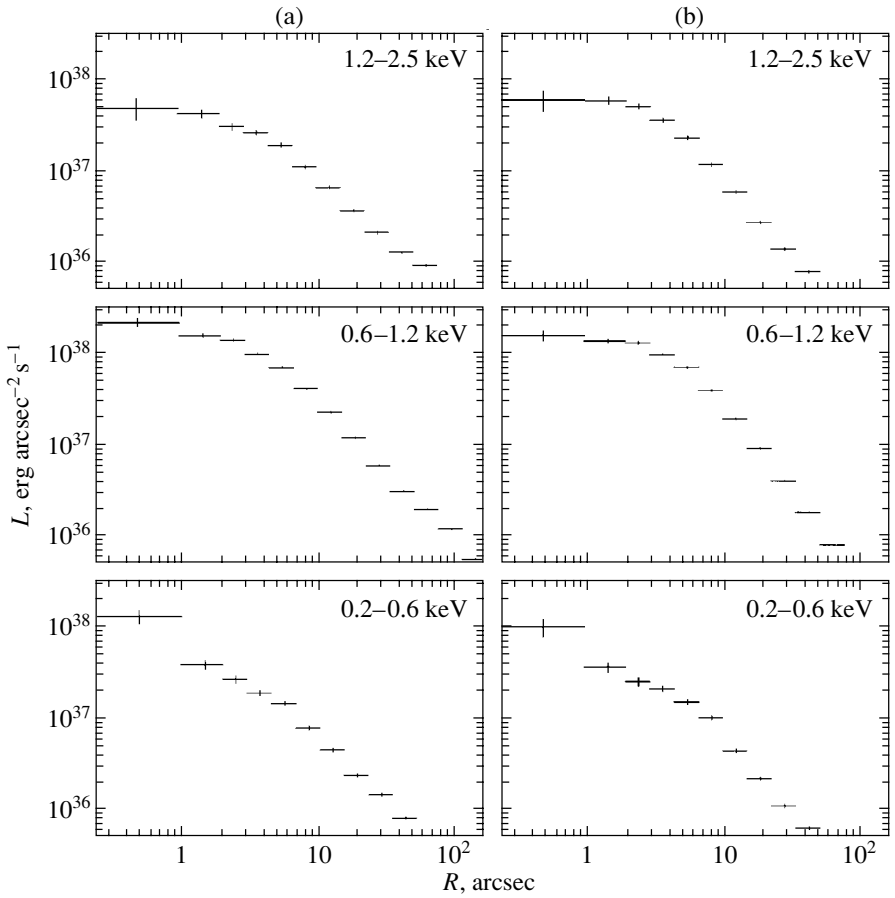

Fig. 2. Surface brightness profiles for the galaxies NGC 4472 (a) and NGC 4649 (b) in the energy ranges 0.2–0.6, 0.6–1.2, and 1.2–2.5 keV.

ions of heavy elements—an expected effect that results in a blurring of the central gas region and an illumination of the peripheral regions. However, this assumption can be rejected, because no central peak is observed in the 1.2–2.5-keV brightness profile, where the contribution from resonance lines is small.

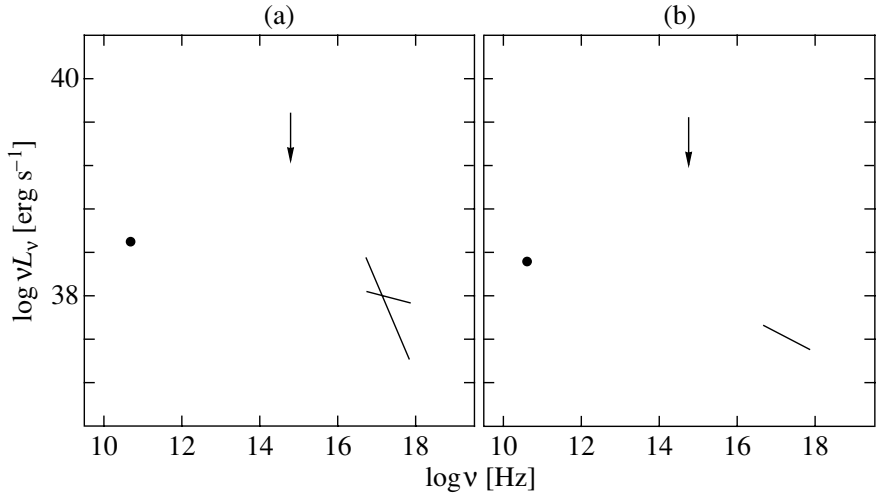

Fig. 3. Radio (dots) and X-ray (lines) fluxes from the central sources in the galaxies NGC 4472 (a) and NGC 4649 (b) and upper limits on the optical luminosity (arrows).

The observed sources are located at the centers of the X-ray images of the galaxies. To identify the X-ray center with the optical center, we can compare the positions of point X-ray sources and optical globular clusters obtained by the Hubble Space Telescope. In general, point X-ray sources are low-mass accreting binary systems, a considerable fraction of which are located in globular clusters. For instance, in one of the galaxies studied, NGC 4472, about 40% of the point X-ray sources are associated with globular clusters (Kundu *et al.* 2002). Comparison of the optical and X-ray images shows that the X-ray and optical centers of the galaxies coincide to within 1″.

THE SOURCE LUMINOSITIES

The galactic gas luminosity in the central pixel can be determined either by describing the surface brightness of the galactic nucleus by model (1) with the exception of the center itself or by determining the mean luminosity from the eight pixels adjacent to the center. In turn, knowing the gas luminosity at the galactic center, we can determine the source luminosities.

The flux from the central sources themselves is low. Over the entire period of our observations in the range 0.2–0.6 keV, it was 22^{-6}_{+7} detector events for NGC 4472 and 11^{-5}_{+6} events for NGC 4649, where the errors are given for a 68% confidence interval (Gehrels 1986). In both cases, the statistical significance of the detection is not lower than 3σ. In the range 0.6–2.5 keV, the flux is statistically significant at a 3σ level only for the source in NGC 4472 and is 29^{-11}_{+12} for the entire period of our observations. In the range 2.5–10 keV, the total flux from the entire central 1″ region in the galaxies is only a few events. Such a low flux from the sources does not allow an accurate judgment about their spectra to be made.

The effective area of the ACIS detector in the range 0.2–0.6 keV is small and has a sawtooth shape with sharp dips. Therefore, the most accurate method of determining the source 0.2–0.6 keV luminosities is to model the detector response to an appropriate spectral model. A reasonably expected spectrum in the range under study is a power law. By modeling the detector response to a power-law spectrum in the XSPEC code with an allowance made for galactic absorption, we can determine the conversion factor from the number of detector events from the source to its luminosity. Similarly, we can derive the event number–luminosity conversion factor for the range 0.6–2.5 keV by using the same power-law model parameters as those in the 0.2–0.6 keV band. As regards the 2.5–10-keV luminosity, the thermal radiation from the galactic gas with a temperature $T \sim 1$ keV is weak here. Given the smooth shape of the effective area at energies 2.5–10 keV, the fluxes can be calculated directly by dividing the photon en-

Luminosities of the central sources

Object	$L_{0.2-0.6}$, 10^{37} erg s^{-1}	$L_{0.6-2.5}$, 10^{37} erg s^{-1}	$L_{2.5-10.0}$, 10^{37} erg s^{-1}
NGC 4472	$9.2^{+2.8}_{-2.4}$	$7.3^{+2.9}_{-2.6}$	<3.4
NGC 4649	$6.0^{+3.2}_{-2.6}$	<3.4	$4.6^{+4.7}_{-3.1}$

ergy by the effective area. The results of our calculations are presented in the table; in our calculations, the distance to the two galaxies was assumed to be 15.3 Mpc (Faber *et al.* 1997). If the ratio of the 0.6–2.5 and 0.2–0.6-keV fluxes is described by an effective power-law slope, then we obtain the following photon indices: 2.5±0.4 for NGC 4472 and >2.2 for NGC 4649. Figure 3 shows the power-law models with the derived parameters of the photon index and, for comparison, the source radio luminosities at a frequency of 4.3×10^{10} Hz and the upper limits on the optical flux at 5.45×10^{14} Hz taken from Di Matteo *et al.* (1999).

In conclusion, we can give the interstellar-gas parameters required to estimate the accretion rate: the gas temperature and density. The gas density at the galactic centers can be determined by using model (1) for the galactic-gas surface brightness and by describing its spectrum by the mekal model of radiation from an optically thin plasma (Mewe *et al.* 1985, 1986; Kaastra 1992; Liedahl *et al.* 1995) in the XSPEC code (for details, see Voevodkin *et al.* (2002)). Our calculations yield the gas densities $\rho_g = (1.0 \pm 0.1) \times 10^{-24}$ g cm^{-3} at the center of NGC 4472 and $\rho_g = (1.1 \pm 0.1) \times 10^{-24}$ g cm^{-3} at the center of NGC 4649. The gas temperature within 2″ is 0.66±0.02 keV in NGC 4472 and 0.86±0.02 keV in NGC 4649.

CONCLUSIONS

We have analyzed the data on the elliptical galaxies NGC 4649 and NGC 4472 that have recently been obtained with the Chandra orbiting X-ray telescope. Our analysis of the surface brightness of these galaxies suggests the presence of faint X-ray sources at their centers. The most plausible interpretation of the luminosities of these sources is the activity of a supermassive black hole at the galactic center, because the X-ray radiation from the material being accreted onto the massive center must be observed. The sources that we observe are located at the optical centers of the galaxies with the minimum possible error. Note that the spectra of the central sources are considerably softer than those for most of the other objects in the immediate vicinity, which are compact binary sources. Meanwhile, we cannot completely rule out the interpretation of the observed central sources as being radiation from binary systems. In this case, our analysis remains of current interest: if we take the measured fluxes from the sources as an upper limit on the flux from a supermassive black hole, then the derived bounds will be an order of magnitude lower than those obtained previously from ROSAT data (Di Matteo *et al.* 1999).

A peculiar feature of the central sources in the galaxies under study is their low luminosity for supermassive black holes embedded in a dense medium. Our main result is the very detection of such faint sources at the centers of the elliptical galaxies NGC 4472 and NGC 4649 by the Chandra telescope. In the observable range 0.2–10 keV, the sources are detected at a 3σ confidence level only in the 0.2–0.6-keV band in NGC 4649 with a luminosity of $\sim 6 \times 10^{37}$ erg s^{-1} and in the 0.2–2.5 keV band in NGC 4472 with a luminosity of $\sim 1.7 \times 10^{38}$ erg s^{-1}. At present, these sources provide the most dramatic evidence of the discrepancy between predictions of standard accretion models and X-ray observations. It is hoped that analysis of the X-ray data on these galaxies will be useful for testing theories that explain the deficit of the luminosity in the nuclei of some galaxies.

ACKNOWLEDGMENTS

This work was supported by the Russian Foundation for Basic Research (project no. 00-02-17124), the Program "Nonstationary Astronomical Phenomena" of the Russian Academy of Sciences, the Ministry of Industry and Science of the Russian Federation (scientific school 00-19-96649), and a grant of the Sixth Expertise Competition of the Commission for Work with Young Scientists of the Russian Academy of Sciences.

REFERENCES

1. M. Abramowicz, X. Chen, and R. Taam, Astrophys. J. **452**, 379 (1995).
2. H. Bondi, Mon. Not. R. Astron. Soc. **112**, 195 (1952).
3. Y. Byun, C. Grillmair, S. Faber, *et al.*, Astron. J. **111**, 1889 (1996).
4. A. Cavaliere and R. Fusco-Femiano, Astron. Astrophys. **49**, 137 (1976).
5. J. Condon, D. Frayer, and J. Broderick, Astron. J. **101**, 362 (1991).
6. T. Di Matteo, A. Fabian, M. Rees, *et al.*, Mon. Not. R. Astron. Soc. **305**, 492 (1999).
7. S. Faber, S. Tremaine, E. Ajhar, *et al.*, Astron. J. **114**, 1771 (1997).
8. K. Gebhardt, R. Bender, G. Bower, *et al.*, Astrophys. J. **539**, L13 (2000).
9. N. Gehrels, Astrophys. J. **303**, 336 (1986).
10. J. Irwin and C. Sarazin, Astrophys. J. **471**, 683 (1996).
11. J. Kaastra, *An X-Ray Spectral Code for Optically Thin Plasmas* (Internal SRON-Leiden Report, updated version 2.0) (1992).
12. J. Kormendy and D. Richstone, Ann. Rev. Astron. Astrophys. **33**, 581 (1995).
13. A. Kundu, T. Maccarone, and S. Zepf, Astrophys. J. **574**, L5 (2002).

14. D. Liedahl, A. Osterheld, and W. Goldstein, Astrophys. J. **438**, L115 (1995).
15. J. Magorrian, S. Tremaine, D. Richstone, *et al.*, Astron. J. **115**, 2285 (1998).
16. R. Mewe, E. Gronenschild, and G. van den Oord, Astron. Astrophys., Suppl. Ser. **62**, 197 (1985).
17. R. Mewe, J. Lemen, and G. van den Oord, Astron. Astrophys., Suppl. Ser. **65**, 511 (1986).
18. R. Narayan and I. Yi, Astrophys. J. **444**, 231 (1995a).
19. R. Narayan and I. Yi, Astrophys. J. **452**, 710 (1995b).
20. R. Narayan, I. Igumenshchev, and M. Abramowicz, Astrophys. J. **539**, 798 (2000).
21. E. Quataert and A. Gruzinov, Astrophys. J. **539**, 809 (2000).
22. G. Trinchieri, G. Fabbiano, and D. Kim, Astron. Astrophys. **318**, 361 (1997).
23. A. A. Voevodkin, A. A. Vikhlinin, and M. N. Pavlinsky, Pis'ma Astron. Zh. **28**, 417 (2002) [Astron. Lett. **28**, 366 (2002)].
24. J. Wrobel, Astron. J. **101**, 127 (1991).

Translated by G. Rudnitskii

Astronomy Letters, Vol. 29, No. 5, 2003, pp. 304–310. Translated from Pis'ma v Astronomicheskiĭ Zhurnal, Vol. 29, No. 5, 2003, pp. 349–355.

Peculiar Features of the Velocity Field of OB Associations and the Spiral Structure of the Galaxy

A. M. Melnik*

Sternberg Astronomical Institute, Universitetskii pr. 13, Moscow, 119992 Russia

Received November 22, 2002

Abstract—Some of the peculiar features of the periodic velocity-field structure for OB associations can be explained using the Roberts–Hausman model, in which the behavior of a system of dense clouds is considered in a perturbed potential. The absence of statistically significant variations in the azimuthal velocity across the Carina arm probably results from its sharp increase behind the shock front, which is easily blurred by distance errors. The existence of a shock wave in the spiral arms and, at the same time, the virtually free motion of OB associations in epicycles can be reconciled in the model of particle clouds with a mean free path of 0.2–2 kpc. The velocity field of OB associations exhibits two appreciable nonrandom deviations from an ideal spiral pattern: a 0.5-kpc displacement of the Cygnus- and Carina-arm fragments from one another and a weakening of the Perseus arm in quadrant III. However, the identified fragments of the Carina, Cygnus, and Perseus arms do not belong to any of the known types of spurs.

Key words: *kinematics and dynamics, Milky Way Galaxy, spiral pattern, OB associations.*

INTRODUCTION

Here, we analyze some of the peculiar features or defects of the periodic velocity-field structure for OB associations (Melnik *et al.* 2001). First, we found no statistically significant variations in the azimuthal residual velocity across the Carina arm, although we clearly see its variations across the Cygnus and Perseus arms. Second, OB associations exhibit the features of both collisional and collisionless motions. Third, the displacement of individual arm fragments from one another such that they do not form a single smooth spiral arm and the gaps in the spiral structure should be explained.

Some of the peculiar features listed above can be explained by using the model of Roberts and Hausman (1984), in which the behavior of a system of dense clouds is considered in a perturbed potential. There is ample theoretical and observational evidence for the existence of small, unaccounted molecular gas condensations, from which giant molecular complexes are formed at certain times (Solomon *et al.* 1985; Pringle *et al.* 2001).

The response of a subsystem of elementary particle clouds to the propagation of a density wave over the stellar disk was first considered by Levinson and Roberts (1981). They assumed that clouds could collide inelastically with each other and coalesce in some cases. In contrast to a continuous gaseous medium, which responds to a potential perturbation by an abrupt density jump, a subsystem of dense particle clouds exhibits smoother variations in gas-dynamical parameters across spiral arms (Levinson and Roberts 1981).

Roberts and Hausman (1984) considered the behavior of a subsystem of clouds with a velocity dispersion of $\Delta u = 6$ km s^{-1} and showed that the local cloud–cloud collision frequency increases sharply in spiral arms due to the crowding of cloud orbits in arms. This increase inevitably gives rise to a shock wave even in systems with a large cloud mean free path (see case G, $p = 2$ kpc in the above paper).

The study of molecular clouds in the Galaxy is complicated by the fact that, in general, we do not know their distances and observe their distribution in the (l, V_{LSR}) plane. However, the spiral structure of the Galaxy is difficult to analyze in the (l, V_{LSR}) plane and virtually impossible in the inner regions (Kwan and Veides 1987; Adler and Roberts 1992). Constructing and analyzing the velocity field of young stars, which, on average, have the same velocities as their parent molecular clouds, give a unique opportunity for studying the velocity field of molecular clouds and the Galactic spiral structure.

*E-mail: anna@sai.msu.ru

1063-7737/03/2905-0304$24.00

ANALYSIS OF THE VELOCITY FIELD OF OB ASSOCIATIONS

The Periodic Velocity-Field Structure of OB Associations

Analysis of the velocity field of OB associations within 3 kpc of the Sun revealed periodic variations in the radial residual velocity component V_R along the Galactic radius vector with a scale length of $\lambda = 2 \pm 0.2$ kpc and amplitude $f_R = 7 \pm 2$ km s^{-1} (Melnik *et al.* 2001). Figure 1a shows the distribution of the radial residual velocities V_R of OB associations along the Galactocentric distance. The filled and open circles represent the associations located in the regions $0° < l < 180°$ and $180° < l < 360°$, respectively. This was done in order to separate the initial parts of the arms in quadrants I and II from their extensions in quadrants III and IV. The periodic variations of the two velocity components were assumed to be in the shape of sine waves. The parameters of the sine waves were determined by solving the equations for the line-of-sight velocities and proper motions of OB associations in two regions: $30° < l < 180°$ and $180° < l < 360°$ (for more details, see Melnik *et al.* 2001). The minima in the radial residual velocity (Fig. 1) distribution determine the kinematical locations of the arm fragments, which we call the Carina (open circles, $R = 6.5$ kpc), Cygnus (filled circles, $R = 6.8$ kpc), and Perseus (filled circles, $R = 8.2$ kpc) arms.

In Fig. 1a, we see no second minimum in the radial velocity distribution in the region $180° < l < 360°$ (open circles). This second minimum should have corresponded to the extension of the Perseus arm in quadrant III. The local decrease in V_R is observed at a Galactocentric distance of $R = 8.5$ kpc, but it does not reach negative values.

As regards the azimuthal velocity field, periodic variations in the azimuthal residual velocity component V_θ with an amplitude of $f_\theta = 7 \pm 2$ km s^{-1} are observed in the region $30° < l < 180°$, where the Cygnus and Perseus arms are located (Fig. 1b). The positions of the minima in the distributions of the radial (Fig. 1a) and azimuthal (Fig. 1b) residual velocities, which determine the kinematic locations of the Cygnus and Perseus arms, coincide within the error limits. At the same time, no significant variations in the azimuthal residual velocity were found in the region $180° < l < 360°$ where the Carina arm lies and where the imaginary extension of the Perseus arm could be located.

The interarm distance of $\lambda = 2$ kpc yields a mean arm pitch angle of $i = 5°$ for the two-armed model of the spiral pattern. The Galactocentric distance of the Sun was assumed to be $R_0 = 7.1$ kpc (Rastorguev *et al.* 1994; Dambis *et al.* 1995; Glushkova *et al.* 1998).

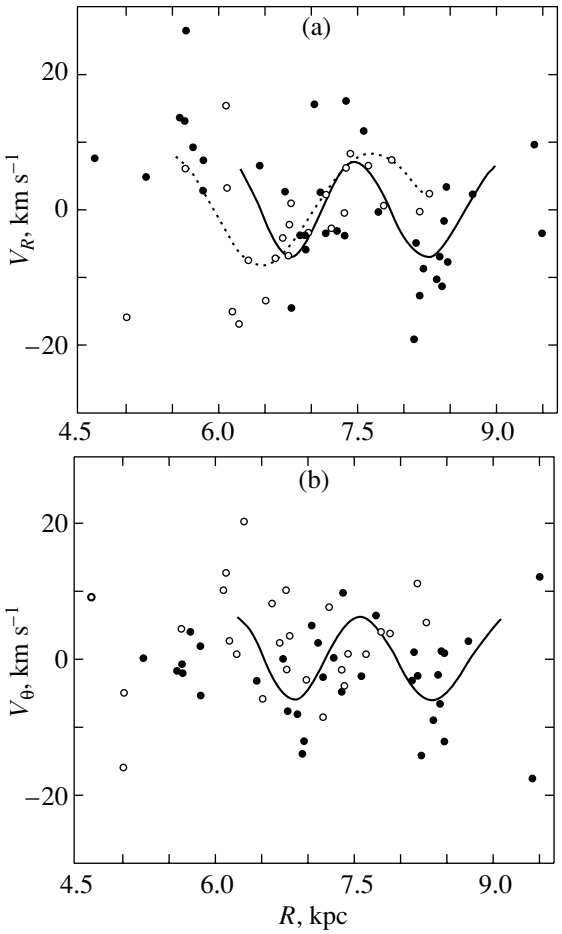

Fig. 1. The distribution of the (a) radial (V_R) and (b) azimuthal (V_θ) residual velocities of OB associations in Galactocentric distance R. OB associations located in the regions $0° < l < 180°$ and $180° < l < 360°$, which are represented by filled and open circles, respectively. The sine-wave parameters were determined by solving the equations for line-of-sight velocities and proper motions in two regions: $30° < l < 180°$ (solid line) and $180° < l < 360°$ (dotted line).

The Profiles of Cloud-Velocity Variations in a Shock Wave

The coincidence of the positions of the minima in the radial and azimuthal velocity distributions in the Cygnus and Perseus arms suggest the existence of a shock wave and cloud–cloud collisions. In a shock wave, extremely negative values of the perturbations of the two velocity components must be reached at the same phase at the shock front (Roberts 1969; Roberts and Hausman 1984), while for a collisionless system the minima in the radial and azimuthal velocity distributions must be shifted by $\pi/2$ in the wave phase (Lin *et al.* 1969). For $\lambda = 2$ kpc, a phase change of $\Delta\chi = \pi/2$ corresponds to a 0.5-kpc displacement across the arm and can undoubtedly be detected.

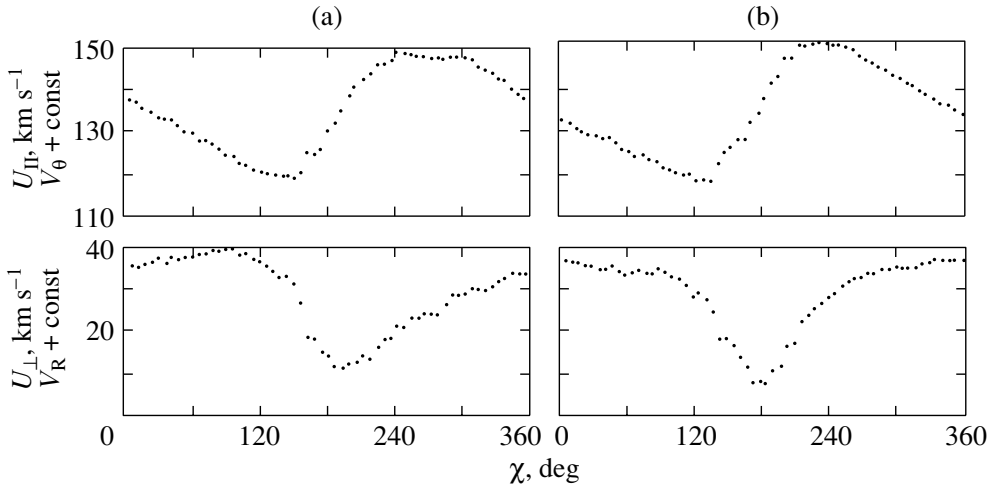

Fig. 2. Variations in the cloud velocity components perpendicular ($U_\perp$) and parallel ($U_\parallel$) to the shock front with spiral-wave phase χ for cloud systems with a mean free path of (a) $p = 0.2$ kpc and (b) $p = 1.0$ kpc (b) (Roberts and Hausman 1984, Fig. 13).

Consider the variations in the two components of the mean cloud velocity perpendicular ($U_\perp$) and parallel ($U_\parallel$) to the shock front with the wave phase, as obtained by Roberts and Hausman (1984) for models of cloud subsystems with different mean free paths: $p = 0.2$ kpc and $p = 1.0$ kpc (Figs. 2a, 2b). For tightly wound arms, the Galactic radius vector is almost perpendicular to the spiral arms. Therefore, the variation in the mean velocity of a particle ensemble perpendicular to the shock front ($U_\perp$), which is commonly used in gas dynamics, is identical to the variations in the radial residual velocity, implying that $V_R = U_\perp +$ const. A similar relation also holds for the velocity component $U_\parallel$ parallel to the shock front whose variation corresponds to the variation in the azimuthal residual velocity $V_\theta = U_\parallel +$ const. The wave phase changes in the direction perpendicular to the spiral arm and for tightly wound arms this direction virtually coincides with the direction of the Galactic radius vector. A change in the wave phase χ from 0° to 360° corresponds to an increase in the Galactocentric distance R by an amount close to λ.

As we see from a comparison of Figs. 2a and 2b, the profiles of the cloud-velocity variations become more symmetric and the positions of the minima in the radial and azimuthal velocity distributions are shifted from one another with increasing mean free path (i.e., with decreasing importance of collisions). Cloud–cloud collisions cause the asymmetric changes in the profiles of the radial and azimuthal velocities, leading to the coincidence of their minima at the shock front (Roberts and Hausman 1984).

Behind the shock front, where the star formation is most intense, the azimuthal velocity varies with Galactocentric distance twice as fast as the radial velocity (Fig. 2a). Indeed, at the shock front ($\chi = 180°$), the two velocity components reach their minima and at the conditional outer arm boundary ($\chi = 270°$), the azimuthal component already reaches its maximum, whereas the radial component increases only to zero (the mean between the peaks in Fig. 2a). Since the abrupt velocity variations with distance are easily blurred by distance errors, the variations in the azimuthal component behind the shock front are more difficult to detect. This may be the reason why we found no statistically significant variations in the azimuthal residual velocity across the Carina arm, although the variations in the radial component across this arm are clearly seen. The variations in the azimuthal velocity across the Carina arm can be simply blurred by distance errors. This removes the serious logical contradiction, because the absence of variations in azimuthal velocity across the Carina arm cannot be explained by any theoretical models.

The fact that we, nevertheless, see the variations in the azimuthal velocity across the Cygnus and Perseus arms can be explained by their privileged positions. The Perseus arm is located in the outer region of the Galaxy where objects with erroneous distances have greatly different line-of-sight velocities and can be eliminated from the sample. This cannot be done for objects of the Carina arm ($l = 280°–310°$), because the line-of-sight velocity variations with distance in this direction are small. The same difficulty also concerns the Cygnus arm ($l = 75°–100°$), but it is, on average, closer to the Sun than the Perseus and Carina arms, which significantly facilitates its study.

The Location of the Corotation Radius

The fact that radial residual velocities of most (70%) of the rich OB-associations are directed toward the Galactic center definitely indicates that the region under study is located within the corotation radius (Melnik *et al.* 2001). We considered OB associations with more than 30 stars in the catalog of OB associations by Blaha and Humphreys (1989) to be rich. The model of particle clouds allows us to easily explain the logical relationship between the kinematics of rich OB associations and their locations relative to the corotation radius. Let us assume that the star formation in rich OB associations was more intense precisely because of the increase in the frequency of cloud–cloud collisions. The locations of rich OB associations must then coincide with the location of the shock front. And only within the corotation radius does the location of the shock front correspond to the minimum in the cloud radial velocity distribution. Therefore, all of the region under study must be located within the corotation radius or, in other words, the corotation radius in the Galaxy must lie beyond the region under study, i.e., beyond the Perseus arm. This implies that the angular velocity of the spiral pattern Ω_p must be lower than the mean angular velocity of the Galactic rotation at the Perseus-arm distance. Taking the rotation-curve parameters from Melnik *et al.* (2001), we obtain the following constraint on Ω_p in absolute units: $\Omega_p < 25$ km s^{-1} kpc^{-1}.

The Mean Free Path of Molecular Clouds and the Axial Ratio of the Velocity Ellipsoid for OB Associations

An analysis of the kinematics of OB associations (Dambis *et al.* 2001) shows that the axial ratio of the velocity ellipsoid for OB associations in the radial and azimuthal directions in the Galaxy is $\sigma_u : \sigma_v = 8.2 : 5.8 = 1.4$. This value is close to the ratio of the amplitudes of the radial and azimuthal velocities for epicyclic motion, $2\Omega/\kappa = 1.6$, where κ is the epicyclic frequency. An axial ratio of the velocity ellipsoid close to the Lindblad ratio $2\Omega/\kappa$ was also obtained for young clusters (Zabolotskikh *et al.* 2002), implying that the clouds out of which young stars are born move almost freely in epicycles. Therefore, the clouds collide only at the shock front, whereas behind the front and in the interarm space they undergo no collisions and move ballistically. This implies that the cloud mean free path behind the shock front must be larger than the epicycle scale size. For a subsystem with a velocity dispersion of $\Delta u = 6$ km s^{-1}, the epicycle radius in an unperturbed region of the Galactic disk is $X \approx 0.2$ kpc. Therefore, for a mean free path $p > 0.2$ kpc, cloud–cloud collisions will occur mostly at the shock front, which is also confirmed by the direct computations of cloud orbits performed by Hausman and Roberts (1984). Note that the local mean free path depends on cloud density and its values in the arm and the interarm region can differ by more than a factor of 6 (Levinson and Roberts 1981).

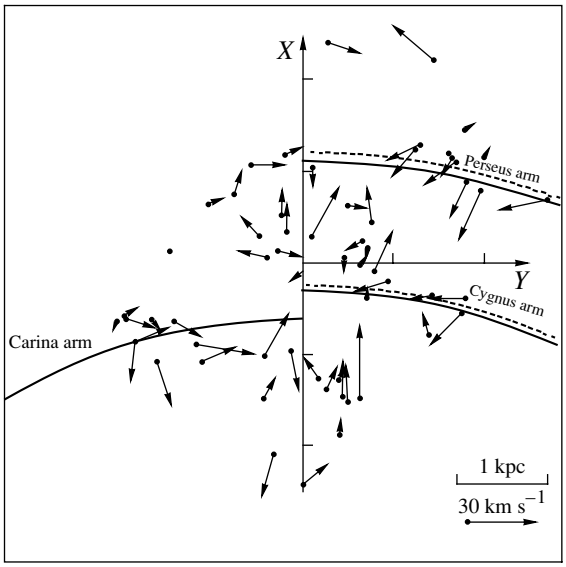

Fig. 3. The residual-velocity field for OB associations in a projection onto the Galactic plane. The X axis is directed away from the Galactic center and the Y axis is in the direction of the Galactic rotation. The Sun is at the coordinate origin. The circular arcs correspond to the minimum radial (solid line) and azimuthal (dashed line) residual velocities of OB associations and determine the kinematic positions of the Carina, Cygnus, and Perseus arms.

Deviations from an Ideal Spiral Pattern

Figure 3 shows the velocity field of OB associations in projection onto the Galactic plane. The circular arcs in this figure correspond to the minima in the radial (solid line) and azimuthal (dashed line) residual velocity distributions and determine the kinematic positions of the Carina, Cygnus, and Perseus arms. Both deviations from an ideal spiral pattern—the displacement of the Cygnus and Carina arm fragments relative to each other such that they do not form a single, smooth spiral arm and the absence of the Perseus arm extension in quadrant III—are clearly seen in Fig. 3. The extension of the Perseus arm in quadrant III shows up neither in kinematics nor in an increase in the density of young stars.

The kinematic position of the Carina arm ($R = 6.5 \pm 0.1$ kpc) is displaced relative to the Cygnus arm ($R = 6.8 \pm 0.1$ kpc) by 0.3 kpc. This displacement was obtained for the model of ring arms. Its statistical significance is 2σ. The displacement increases

to 0.5 kpc for the model of trailing spiral arms even with a small pitch angle $i = 5°$. Its statistical significance also increases. In contrast, the displacement decreases for the model of leading arms. The problem is that a trailing arm cannot be drawn through the complexes of young objects in Carina and Cygnus, but these complexes fall nicely on a leading arm (Fig. 3).

SPIRAL ARMS AND SPURS

The main puzzle of the Galactic spiral structure in the solar neighborhood lies in the appreciable nonrandom deviations from an ideal spiral pattern. The images of other galaxies often show deviations from a smooth spiral pattern on short and intermediate scales, which are usually called spurs. The element of chaos introduced by spurs into the spiral structure of galaxies can also be used, in principle, to explain the defects in the Galactic spiral pattern. Let us use the definition of a spur given by Roberts and Hausman (1984) as a region of intense star formation located far from the line of minimum potential and consider various spur generation mechanisms.

Roberts and Hausman (1984) showed that the possible long delay of star formation behind the shock front leads to a blurring of the spiral arms identified by a concentration of young stars and to the appearance of spurs. The successive star formation in the Galaxy produced by supernova explosions (Gerola and Seiden 1978) also facilitates the formation of spurs. However, in the presence of a density wave, the cloud velocity field has a characteristic periodic structure and neither the successive formation nor the delay of star formation has any effect on this field (Roberts and Hausman 1984). Moreover, they could facilitate the detection of a periodic velocity-field structure by revealing the cloud velocities and distances at different spiral-wave phases. The fragments of the Carina, Cygnus, and Perseus arms that we identified cannot be spurs of this type, by any means. A comparison of their kinematics with the computed velocity field (Roberts and Hausman 1984) clearly indicates that they are located near the line of minimum potential. The complex of young objects in Sagittarius whose kinematics or, more specifically, the radial residual velocity of young stars directed away from the Galactic center (Fig. 3) is suggestive of its interarm location must be called a spur by the definition of Roberts and Hausman.

Roberts and Stewart (1987) found another spur generation mechanism. They showed that for a large mean free path, individual fragments of the spiral pattern can temporarily shift in phase from each other, while the global spiral pattern of the cloud subsystem can exhibit ruggedness and gaps. The shift of the cloud density maximum (collective sloshing) relative to the potential minimum is produced by the tuning of the epicyclic motions of individual clouds (Roberts and Stewart 1987). For collisionless models, the displacement of individual arm fragments relative to each other can reach 20% of the interarm distance, while for a system with a mean free path of $p = 0.2$ kpc it does not exceed 5%. However, the collective sloshing mechanism can no longer explain the 0.5 kpc displacement of the kinematic positions of the Carina and Cygnus arm fragments. The Galactic cloud system is undoubtedly collisional and, consequently, this mechanism cannot produce large deviations from a smooth spiral pattern.

Weaver (1970) found another type of spur similar to the branches at the outer arm edges. Elmegreen (1980) found their mean pitch angle to be $60° \pm 10°$. Weaver (1970) and Elmegreen (1980) believe that the Orion region is such a spur in our Galaxy. Strong gas compression in the spiral arm, which can trigger the growth of perturbations in a direction almost perpendicular to the arm, can be responsible for the appearance of such spurs (Balbus 1988; Kim and Ostriker 2002). However, the Carina, Cygnus, and Perseus arm fragments that we identified do not belong to this type of spurs either. First, no other spiral arms from which these fragments could appear as spurs are observed. Second, the Cygnus and Perseus arm fragments are definitely elongated in the azimuthal direction (Fig. 3).

Yet another type of spurs in the interarm space was found by Contopoulos and Grosbell (1986, 1988) when studying the nonlinear effects in high-order resonances between the epicyclic frequency and the relative rotation rate of the spiral pattern. The spurs and gaps in the spiral structure near corotation are produced by nonlinear effects, which lead to a difference in the shapes and orientations of the periodic orbits inside and outside the 4/1 resonance ($\kappa/(\Omega - \Omega_p) = 4/1$). The orbits outside the 4/1 resonance can be oriented in such a way that the maximum of their crowding may not coincide with the spiral arm. However, nonlinear effects arise in the case of high potential perturbation amplitudes and must be observed in galaxies with large arm pitch angles $i > 30°$ (Contopoulos and Grossbell 1986). The tightly would spiral pattern of our Galaxy ($i = 5°$) cannot, in principle, undergo nonlinear effects near corotation.

Thus, none of the spur type listed above can explain the peculiar features of the Galactic spiral structure, more specifically, the deviations from an ideal spiral pattern. The potential perturbation itself is, probably, not an ideal monochromatic spiral wave.

Some authors (Byrd 1983; Byrd *et al.* 1984) consider the spurs produced by the gravitation of a massive complex rotating in the galactic disk (gravitational spurs). However, such spurs differ from the spiral-arm fragments only in their length and perturbation amplitude. Both are produced by a gravitational potential perturbation and are located near the potential minimum.

CONCLUSIONS

Some of the peculiar features of the periodic velocity-field structure for OB associations (Melnik *et al.* 2001) can be explained by using the model of Roberts and Hausman (1984), in which the behavior of a system of dense clouds is considered in a perturbed potential. The absence of statistically significant variations in the azimuthal velocity across the Carina arm probably results from its sharp increase behind the shock front, which is easily blurred by distance errors. The existence of a shock wave in spiral arms and, at the same time, the virtually free motion of OB associations in epicycles can be reconciled in the model of particle clouds with a mean free path of 0.2–2 kpc. The velocity field of OB associations exhibits two appreciable nonrandom deviations from an ideal spiral pattern: a 0.5-kpc displacement of the Cygnus- and Carina-arm fragments from one another and a weakening of the Perseus arm in quadrant III. Nevertheless, the identified fragments of the Carina, Cygnus, and Perseus arms in this paper do not belong to any of the known types of spurs. The perturbation of the Galactic potential is probably not a monochromatic spiral wave.

The spiral arms of our Galaxy are often compared with those of the Andromeda galaxy. Both galaxies have a tightly wound spiral pattern and similar streaming motions. The mean interarm distance of $\lambda = 3$ kpc observed in the Andromeda galaxy at distances $R = 6$–16 kpc corresponds to a mean pitch angle of $i = 7°$ (Arp 1964; Braun 1991). The spiral pattern of the Galaxy in the solar neighborhood has similar parameters, $\lambda = 2$ kpc and $i = 5°$ (Melnik *et al.* 1999, 2001). The change in the velocity of neutral and molecular hydrogen clouds across the spiral arms in the Andromeda galaxy is 10–20 km s^{-1} (Braun 1991; Neininger *et al.* 2001), which is close to the velocity of the streaming motions of young stars in our Galaxy. In addition, the distribution of H II regions in the Andromeda galaxy also exhibits deviations of the individual arm fragments from an ideal monochromatic spiral pattern (Considere and Athanassoula 1982; Braun 1991).

ACKNOWLEDGMENTS

I am grateful to A.V. Zasov for the discussion and helpful remarks, which contributed to a substantial improvement of the paper. I wish to thank I.I. Pasha, A.S. Rastorguev, and Yu.N. Efremov for useful advice and remarks. This work was supported by the Russian Foundation for Basic Research (project nos. 02-02-16667 and 00-02-17804), the Council for the Program of Support of Leading Scientific Schools (project no. 00-15-96627), and the Federal Research and Technology Program "Astronomy."

REFERENCES

1. D. S. Adler and W. W. Roberts, Astrophys. J. **384**, 95 (1992).
2. H. Arp, Astrophys. J. **139**, 1045 (1964).
3. S. A. Balbus, Astrophys. J. **324**, 60 (1988).
4. C. Blaha and R. M. Humphreys, Astron. J. **98**, 1598 (1989).
5. R. Braun, Astrophys. J. **372**, 54 (1991).
6. G. G. Byrd, Astrophys. J. **264**, 464 (1983).
7. G. G. Byrd, B. F. Smith, and R. H. Miller, Astrophys. J. **286**, 62 (1984).
8. S. Considere and E. Athanassoula, Astron. Astrophys. **111**, 28 (1982).
9. G. Contopoulos and P. Grosbol, Astron. Astrophys. **155**, 11 (1986).
10. G. Contopoulos and P. Grosbol, Astron. Astrophys. **197**, 83 (1988).
11. A. K. Dambis, A. M. Melnik, and A. S. Rastorguev, Pis'ma Astron. Zh. **21**, 331 (1995) [Astron. Lett. **21**, 291 (1995)].
12. A. K. Dambis, A. M. Melnik, and A. S. Rastorguev, Pis'ma Astron. Zh. **27**, 68 (2001) [Astron. Lett. **27**, 58 (2001)].
13. D. M. Elmegreen, Astrophys. J. **242**, 528 (1980).
14. H. Gerola and P. E. Seiden, Astrophys. J. **223**, 129 (1978).
15. E. V. Glushkova, A. K. Dambis, A. M. Melnik, and A. S. Rastorguev, Astron. Astrophys. **329**, 514 (1998).
16. M. A. Hausman and W. W. Roberts, Astrophys. J. **282**, 106 (1984).
17. W.-T. Kim and E. C. Ostriker, Astrophys. J. **570**, 132 (2002).
18. J. Kwan and F. Valdes, Astrophys. J. **315**, 92 (1987).
19. F. H. Levinson and W. W. Roberts, Astrophys. J. **245**, 465 (1981).
20. C. C. Lin, C. Yuan, and F. H. Shu, Astrophys. J. **155**, 721 (1969).
21. A. M. Melnik, A. K. Dambis, and A. S. Rastorguev, Pis'ma Astron. Zh. **25**, 602 (1999) [Astron. Lett. **25**, 518 (1999)].
22. A. M. Melnik, A. K. Dambis, and A. S. Rastorguev, Pis'ma Astron. Zh. **27**, 611 (2001) [Astron. Lett. **27**, 521 (2001)].

23. N. Neininger, Ch.Nieten, M. Guelin, *et al.*, *Proceedings of 205th Symp. of the IAU Galaxies and Their Constituents at the Highest Angular Resolutions,* Ed. by R. T. Schilizzi, S. Vogel, *et al.* (PASP, San Francisco, 2001), p. 352.
24. J. E. Pringle, R. J. Allen, and S. H. Lubow, Mon. Not. R. Astron. Soc. **327**, 663 (2001).
25. A. S. Rastorguev, O. V. Durlevich, E. D. Pavlovskaya, and A. A. Filippova, Pis'ma Astron. Zh. **20**, 688 (1994) [Astron. Lett. **20**, 591 (1994)].
26. W. W. Roberts, Astrophys. J. **158**, 123 (1969).
27. W. W. Roberts and G. R. Stewart, Astrophys. J. **314**, 10 (1987).
28. W. W. Roberts and M. A. Hausman, Astrophys. J. **277**, 744 (1984).
29. P. M. Solomon, D. B. Sanders, and A. R. Rivolo, Astrophys. J. Lett. **292**, L19 (1985).
30. H. Weaver, *Proceedings of 39th IAU Symp. Interstellar Gas Dynamics,* Ed. by H. Habing (Reidel, Dordrecht, 1970), p. 22.
31. M. V. Zabolotskikh, A. S. Rastorguev, and A. K. Dambis, Pis'ma Astron. Zh. **28**, 516 (2002) [Astron. Lett. **28**, 454 (2002)].

Translated by A. Dambis

Astronomy Letters, Vol. 29, No. 5, 2003, pp. 311–320. Translated from Pis'ma v Astronomicheskiĭ Zhurnal, Vol. 29, No. 5, 2003, pp. 356–366.

The Line-of-Sight Velocities of OB Associations and Molecular Clouds in a Wide Solar Neighborhood: The Streaming Motions of Stars and Gas in the Perseus Arm

T. G. Sitnik*

Sternberg Astronomical Institute, Universitetskii pr. 13, Moscow, 119992 Russia

Received November 15, 2002

Abstract—We compare the line-of-sight velocities of stars in OB associations within 3 kpc of the Sun and the molecular clouds closest to them. The Perseus arm is used as an example to show that the line-of-sight velocity ranges in which OB-association stars, molecular clouds, and H II regions ionized by these association stars are observed overlap. The streaming motions produced by density waves in the $(l, V_{\rm LSR})$ plane were found to lead to an inversion of the distances to objects of the Perseus arm and the interarm space beyond this arm. © *2003 MAIK "Nauka/Interperiodica".*

Key words: *Galactic structure, OB associations, molecular clouds, line-of-sight velocities, residual motions.*

INTRODUCTION

Here, we compare the available line-of-sight velocity observations for stars of the OB associations within 3 kpc of the Sun with the distribution of CO emission in the $(l, V_{\rm LSR})$ plane.

It is undoubtedly of considerable interest to compare the currently available line-of-sight velocity ($V_{\rm LSR}$) observations for young stars and molecular clouds. The interstellar medium is difficult to study because there are no direct distance estimates independent of the line-of-sight velocity (the observed gas parameter). The simplest way of localizing the gas in space is to assume that the Galactic rotation is circular. However, Burton (1971) pointed out that the streaming gas motions produced by spiral density waves should be taken into account, because a purely circular rotation did not describe the observations of neutral hydrogen in the $(l, V_{\rm LSR})$ plane.

Thus, disregarding streaming motions when estimating the kinematic distances can lead to errors in the localization of clouds. At the same time, due to the residual motions, the identification of clouds in the (l, V) plane becomes controversial, because a molecular cloud observed in some velocity range $\Delta V_{\rm LSR}$ can be a superposition of disk clouds that are located at different distances along the line of sight and that have different residual velocities $V_{\rm res}$ (e.g., Liszt and Burton 1981; Adler and Roberts 1992).

Our analysis of the CO-emission distribution performed below is based on the possible physical and genetic relationship between molecular clouds and the OB associations closest to them, whose distances and residual velocities are known. To a first approximation, the bright CO emission features were taken as clouds (Dame *et al.* 2001). Previously (Sitnik *et al.* 2001), we analyzed the residual line-of-sight motions of molecular clouds in the Cygnus arm. Below, we attempt to determine the changes made by streaming motions to the distribution of molecular clouds in the outer Galaxy.

The results of previous residual-velocity studies for OB associations that will be used below are described in the section entitled "A Short Distance Scale...." In the section entitled "The Line-of-Sight Velocity Distribution...," we perform a comparative analysis of the observed line-of-sight velocities for stars of the OB associations and the molecular clouds closest to them and investigate the effect of residual motions on the positions of these outer Galactic objects in the $(l, V_{\rm LSR})$ plane. In conclusion, we summarize our results and draw conclusions about the changes made by streaming motions to the large-scale $(l, V_{\rm LSR})$ distribution of molecular clouds.

THE SHORT DISTANCE SCALE, ROTATION CURVE, AND RESIDUAL VELOCITIES OF OB ASSOCIATIONS

The propagation of density waves in the disks of rotating galaxies gives rise to streaming motions of young stars and gas and produces a peculiar field of residual velocities $V_{\rm res}$ (Lin *et al.* 1969;

*E-mail: sitnik@sai.msu.ru

1063-7737/03/2905-0311$24.00

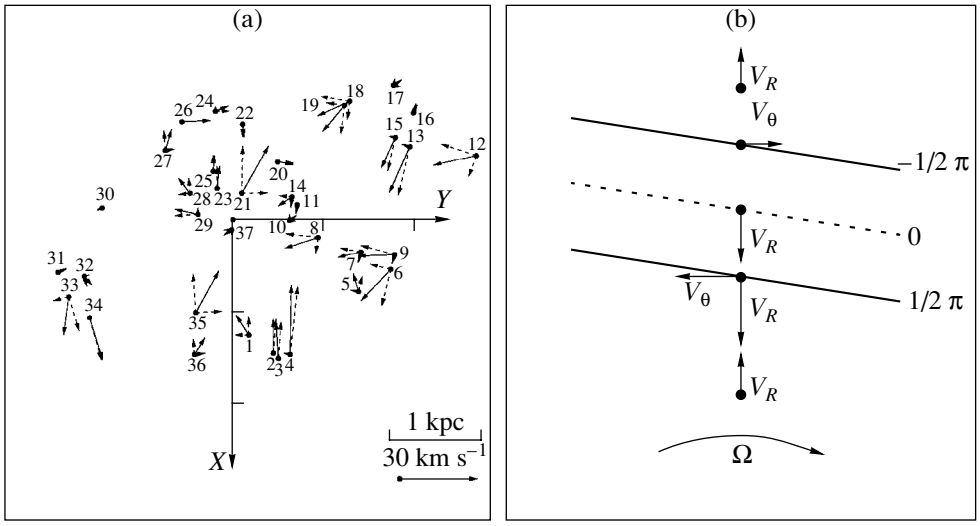

Fig. 1. (a) The observed residual velocity field of the OB associations within 3 kpc of the Sun. The dashed lines represent the radial (V_R) and azimuthal (V_θ) residual space velocities. The numbers correspond to the association numbers in Table 1. The X axis is directed toward the Galactic center. (b) The expected residual velocity field in a shock spiral density wave within the corotation radius. The vectors V_R and V_θ indicate changes in the radial and azimuthal residual velocities, respectively; the angular velocity Ω indicates the sense of Galactic rotation.

Roberts 1969). The residual velocities are determined relative to the frame of reference that uniformly rotates with the linear velocity $V_{\rm gal}$ (the mean circular rotation velocity of the Galaxy at a given distance from its center) and are calculated as $V_{\rm res} = V_{\rm obs} - V_{\rm gal} - V_{\rm ap}$, where $V_{\rm obs}$ is the observed heliocentric velocity and $V_{\rm ap}$ is the velocity of the Sun toward the apex. The field of residual space velocities $V_{\rm res}$ for the OB associations within 3 kpc of the Sun is shown in Fig. 1a (Melnik *et al.* 1998, 2001; Sitnik and Melnik 1999). The detected streaming motions of the OB associations are in good agreement with predictions of the theory of shock spiral density waves (Fig. 1b).

In studying the streaming motions of molecular clouds and their localization in space, we rely on the photometric distances and residual line-of-sight velocities $V_{r,\rm res}$ of neighboring OB associations. Columns 1–15 of Table 1 give, respectively, the association numbers and names; Galactic coordinates; photometric distances; Galactocentric distances; the median line-of-sight velocities of the OB associations ($V_{\rm LSR}$); residual line-of-sight velocities ($V_{r,\rm res}$); stellar line-of-sight velocity dispersions ($\sigma_{V_{\rm LSR}}$); residual space velocities along the Galactic radius, V_R, in the azimuthal direction, V_θ, and perpendicular to the Galactic plane, V_Z; the number of association stars with measured radial velocities (n_r) and proper motions (n_l); and the total number of association stars (N). For a convenient comparison, the line-of-sight velocities of OB-association stars (as well as the interstellar gas) were corrected for the solar motion toward the standard apex. A detailed description of how the median residual velocities of the OB associations were determined was given by Melnik *et al.* (1998, 2001) and Sitnik and Melnik (1999). The initial data—the line-of-sight velocities and proper motions of OB-association member stars (Blaha and Humphreys 1989)—were taken from the catalog of Barbier-Brossat and Figon (2000) and the Hipparcos catalog.

The Rotation Curve

The residual velocities of the OB associations given in Table 1 were determined by Melnik *et al.* (2001). These authors used the Galactic rotation curve obtained by analyzing the space velocities of OB associations. The rotation curve has the following parameters: the angular velocity of the disk at the solar distance is $\Omega(R_0) = 30$ km s^{-1} kpc^{-1}; the first and second derivatives of the angular velocity with respect to the Galactocentric distance are $\Omega'(R_0) = -5.0$ km s^{-1} kpc^{-2} and $\Omega''(R_0) = 1.5$ km s^{-1} kpc^{-3}. The velocity components of the Sun relative to the centroid of the OB associations are $V_X = -7.5$ km s^{-1} and $V_Y = 11.2$ km s^{-1}. The z velocity component of the Sun relative to the centroid of young stars was taken to be $V_Z = 7$ km s^{-1} (Rastorguev *et al.* 1999).

The Distance Scale

We used the short distance scale that was initially obtained for Cepheids (Berdnikov 1987; Berdnikov *et al.* 1996) to study the residual velocities

Table 1

	Association	l	b	r, kpc	$R_{\rm gal}$	$V_{\rm LSR}$, km s^{-1}	$V_{r,\rm res}$, km s^{-1}	$\sigma_{V_{\rm LSR}}$, km s^{-1}	V_R, km s^{-1}	V_θ, km s^{-1}	V_Z, km s^{-1}	n_r	n_l	N
1	Sgr OB1	7.6	−0.8	1.3	5.8	1.8	−8.1	12.1	7.3	−5.4	1.0	37	29	66
2	Ser OB1	16.7	0.1	1.5	5.7	8.9	−12.5	20.0	13.0	−0.9	1.4	17	12	43
3	Ser OB2	18.2	1.6	1.6	5.6	10.4	−13.4	14.5	13.7	−1.9	−3.7	7	5	18
4	Sct OB2	23.2	−0.5	1.6	5.7	4.0	−24.0	20.0	26.3	−2.3	4.9	6	6	13
5	Vul OB1	60.4	0.0	1.6	6.5	21.1	−5.0	14.7	6.4	−3.3	6.1	9	8	28
6	Cyg OB3	72.8	2.0	1.8	6.8	8.0	−7.4	9.5	−14.5	−7.8	−4.0	30	18	42
7	Cyg OB1	75.8	1.1	1.5	6.9	3.6	−8.1	8.9	−3.9	−8.3	1.2	34	14	71
8	Cyg OB9	77.8	1.8	1.0	7.0	−2.5	−11.7	8.6	−5.8	−12.2	0.2	10	8	32
9	Cyg OB8	77.9	3.4	1.8	7.0	−3.9	−13.3	11.0	−3.9	−13.9	12.8	9	10	21
10	Cyg OB7	89.0	0.0	0.6	7.1	5.8	2.5	9.3	2.5	2.4	3.7	21	28	29
11	Cep OB2	102.1	4.6	0.7	7.3	−3.9	−0.8	6.7	−3.2	−0.1	2.8	37	47	59
12	Cep OB1	104.2	−1.0	2.8	8.2	−46.2	−16.8	7.4	−8.7	−14.3	3.1	17	24	58
13	Cas OB2	112.0	0.0	2.1	8.1	−39.9	−13.8	11.0	−19.0	−3.3	6.2	7	5	41
14	Cep OB3	110.4	2.6	0.7	7.4	−12.0	−6.0	3.9	−3.9	−4.9	0.5	18	15	26
15	Cas OB5	116.1	−0.5	2.0	8.2	−36.8	−10.0	7.2	−12.7	−2.7	−11.2	16	13	52
16	Cas OB4	120.1	−0.3	2.3	8.5	−29.1	3.0	8.6	3.4	0.8	−6.4	7	7	27
17	Cas OB8	129.2	−1.1	2.3	8.7	−29.5	3.4	9.9	2.3	2.5	−3.7	14	9	43
18	Per OB1	134.7	−3.2	1.8	8.5	−40.2	−13.2	7.0	−7.8	−12.2	−5.5	81	63	167
19	Cas OB6	135.0	0.8	1.8	8.4	−39.1	−13.1	8.2	−11.2	−6.8	−3.8	12	13	46
20	Cam OB1	141.1	0.9	0.8	7.7	−9.3	3.2	9.4	−0.4	6.2	0.3	30	33	50
21	Per OB2	160.3	−16.5	0.3	7.4	15.0	19.2	4.5	16.0	9.6	−0.9	7	7	7
22	Aur OB1	173.9	0.1	1.1	8.2	−10.2	−4.8	14.0	−4.9	0.8	−2.7	26	20	36
23	Ori OB1	206.9	−17.7	0.4	7.4	8.3	7.1	7.9	8.2	0.5	0.3	62	59	70
24	Gem OB1	189.0	2.2	1.2	8.3	4.1	1.7	5.0	2.2	5.2	3.9	18	17	40
25	Mon OB1	202.1	1.1	0.6	7.6	8.6	5.8	13.0	6.3	0.5	1.8	7	7	7
26	Mon OB2	207.5	−1.6	1.2	8.2	6.3	−4.7	12.5	−0.4	10.9	−0.5	26	18	32
27	CMa OB1	224.6	−1.6	1.1	7.9	16.5	3.6	16.1	7.2	3.5	−7.0	8	10	17
28	Col 121	238.5	−8.4	0.6	7.4	10.8	6.7	7.0	5.9	−4.1	0.1	10	13	13
29	Vel OB2	262.1	−8.5	0.4	7.2	6.9	8.7	9.7	2.2	−8.7	0.8	13	12	13
30	Vel OB1	264.9	−1.4	1.5	7.4	7.0	1.7	4.4	−0.5	−1.9	−2.5	18	18	46
31	Car OB1	286.5	−0.5	2.0	6.8	−16.6	−3.3	8.2	0.8	3.4	−2.2	39	18	126
32	Car OB2	290.4	0.1	1.8	6.7	−18.8	−1.8	8.5	−4.3	2.2	0.3	22	12	59
33	Cru OB1	294.9	−1.1	2.0	6.5	−14.8	8.0	8.9	−13.5	−6.1	−0.2	33	19	76
34	Cen OB1	304.2	1.4	1.9	6.2	−25.6	5.0	14.5	−16.8	0.6	−2.4	32	32	103
35	Ara OB1A	337.7	−0.9	1.1	6.1	−32.9	−18.2	20.6	15.4	10.0	−3.8	8	10	53
36	Sco OB1	343.7	1.4	1.5	5.6	−23.2	−7.1	15.3	6.0	4.2	1.1	28	16	76
37	Sco OB2	351.3	19.0	0.1	7.0	5.4	4.2	2.3	−3.3	−3.1	0.7	10	10	10

of OB associations. Using the short distance scale made it necessary to reconcile the distance scales for Cepheids and OB stars. The distances to the associations were assumed to be $r = 0.8r_{\rm BH}$ (Sitnik and Melnik 1996; Dambis *et al.* 2001), where $r_{\rm BH}$ are the photometric distances from the catalog of Blaha and Humphreys (1989). In general, the short distance scale agrees with the photometric distances to the OB associations in the Galactic northern hemisphere estimated by Garmany and Stencel (1992). It should be noted that the difference between r and $r_{\rm BH}$ is no larger than the error in the photometric distances to associations. The distance to the Galactic center was assumed to be $R_0 = 7.1 \pm 0.5$ kpc (Rastorguev *et al.* 1994; Dambis *et al.* 1995; Glushkova *et al.* 1998).

The Streaming Motions of OB Associations

The following conclusions can be drawn from the analysis of Table 1 (see also Melnik *et al.* 1998, 2001; Sitnik and Melnik 1999).

(1) Three regions are confidently identified in the solar neighborhood: the fragments of the Perseus (Cep OB1; Per OB1; and Cas OB2, OB5, and OB6), Cygnus (Cyg OB1, OB3, OB8, and OB9; and Cep OB2 and OB3), and Carina (Cen OB1, Cru OB1, Car OB2) arms in which the radial residual velocity of the OB associations, V_R, is directed toward the Galactic center and is from approximately -19 to -4 km s^{-1} (Fig. 1a, Table 1). The streaming motions toward the Galactic center are a distinctive feature of the wave arms within the corotation radius (Lin *et al.* 1969; Roberts 1969). Therefore, there is reason to believe that the Perseus, Cygnus, and Carina arms observed near the Sun were produced by density waves and are within the corotation radius.

(2) The azimuthal velocities of the above associations change their magnitude and direction inside the arms: from V_θ from approximately -14 to -7 km s^{-1} near the inner boundary (opposite to the Galactic rotation) to $V_\theta \sim +2$ km s^{-1} near the outer boundary (along the Galactic rotation), as expected in theory (Lin *et al.* 1969; Roberts 1969).

(3) Almost a third of the rich OB associations ($N > 30$) have the kinematics characteristic of the interarm space, i.e., the radial residual velocity directed away from the Galactic center (with the azimuthal velocity along the Galactic rotation). The interarm associations include Ori OB1, Gem OB1, Per OB2, Mon OB1 and OB2, Cma OB1, Coll 121, Sco OB1, Sgr OB1, and Ser OB1 and OB2 (usually assigned to the Orion and Sagittarius arms), as well as Cas OB8 and OB4, Car OB1, Vul OB1, Ara OB1a, and Sco OB1 (Fig. 1b; see also Sitnik and Melnik 1999; Melnik *et al.* 2001). For the overwhelming majority of these associations, $V_R \leq 5$ km s^{-1}.

It should be noted that, in general, associations with small radial residual motions are difficult to unambiguously assign to an arm or the interarm space because, within the error limits and depending on the adopted rotation curve and distance scale, their $V_{\rm R}$ can be directed both toward and away from the Galactic center (Sitnik and Melnik 1999). Therefore, such associations would be more appropriate to call associations near the outer boundary of the arm.

The Line-of-Sight Residual Velocities of OB Associations

Since the proper motions of interstellar clouds are not known, below we consider the streaming motions of associations and clouds only along the line of sight ($V_{r,\rm res} = V_{\rm LSR} - V_{\rm gal}$, where $V_{\rm LSR}$ is the observed line-of-sight velocity relative to the local standard of rest). In most directions, the line-of-sight residual velocity $V_{r,\rm res}$ is a superposition of the radial and azimuthal residual velocities (Fig. 1a).

In the range $30° < l < 330°$, the observed line-of-sight velocity dispersion for the overwhelming majority of the associations is $\sigma < 10$ km s^{-1} (Table 1). The mean line-of-sight velocity dispersion for the OB associations in this range that have at least ten stars with measured $V_{\rm LSR}$ is $\sigma \sim 8.5$ km s^{-1}.

The largest line-of-sight velocity dispersion for OB-associations stars, $\sigma \sim 10$–20 km s^{-1}, is observed toward the Galactic center ($330° < l < 30°$). Several factors contribute to the dispersion: the existing velocity dispersion in the parent clouds, errors in the individual line-of-sight velocities, and localization errors. In the latter case, stars at different distances can be combined into a single association. This may be the reason why the line-of-sight velocity dispersion of the OB associations toward the Galactic center is large (Melnik *et al.* 1998).

Whereas the residual line-of-sight velocities of the OB associations in the inner Perseus, Cygnus, and Carina arms are larger than or of the order of the dispersion, $V_{r,\rm res} \geq \sigma_{V_{\rm LSR}}$ (Table 1), these velocities $V_{r,\rm res}$ of the associations near the outer boundaries of the arms are generally smaller than the dispersion. This is partly because the residual velocity $V_{\rm res}$ in the arms decreases in magnitude with increasing distance from the spiral shock front while changing its direction. At the same time, the line-of-sight velocity dispersion is largely determined by the initial conditions—the line-of-sight velocity dispersion in the parent clouds.

In the part of the Galaxy under study (except for the direction toward the Galactic center), the largest (in magnitude) line-of-sight streaming velocities are observed in the associations of the inner Perseus and Cygnus arms (Table 1). It is in these regions that

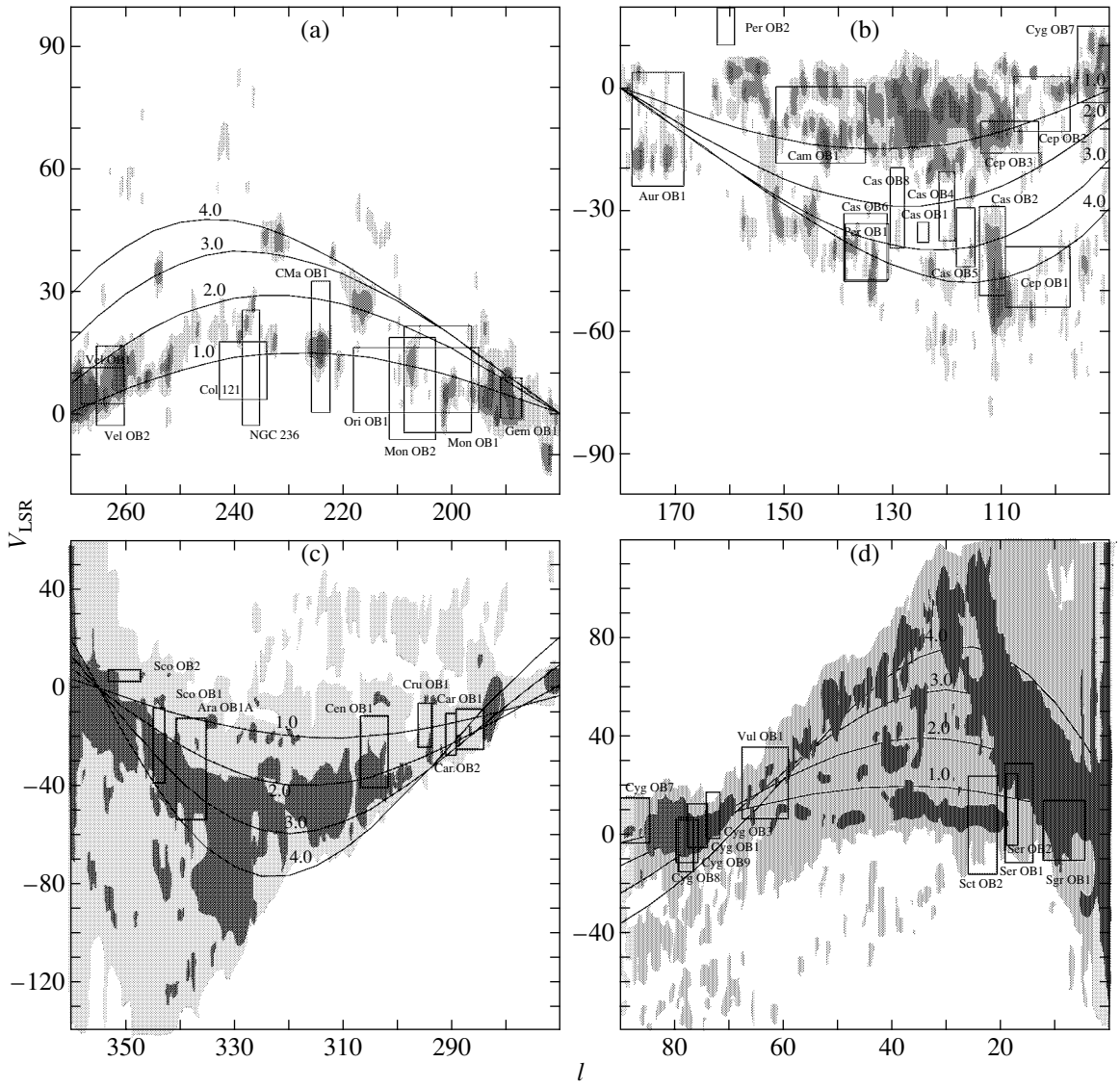

Fig. 2. The distributions of CO emission summed in the range of Galactic latitudes from −2° to +2° and OB associations in the (l, V_{LSR}) plane. The associations are represented by rectangles with the sides equal to the angular size and the stellar line-of-sight velocity dispersion of the association (see Table 1). The family of curves determines the heliocentric distances for different line-of-sight velocities of the Galactic rotation (the distances, in kpc, are indicated by numbers near the curves). The line-of-sight velocities of molecular clouds, OB associations, and Galactic rotation were corrected for the solar motion toward the standard apex. The CO-emission isophotes correspond to the following levels of $\log \int T_{mb} db$: 0.2, 0.1–0.2, and from −1.5 to 0.1 K arcdeg (a, b) and 0.2 and from −1.5 to 0.1 K arcdeg (c, d) (Dame *et al.* 2001). The brightest CO-emission regions correspond to the darkest shaded features.

the possible displacements of interstellar clouds in the (l, V_{LSR}) plane due to spiral density waves should be searched for.

THE LINE-OF-SIGHT VELOCITY DISTRIBUTION OF MOLECULAR CLOUDS AND OB-ASSOCIATION STARS

The line-of-sight velocity distributions of CO emission (Dame *et al.* 2001) and OB associations in the range of Galactic longitudes $l \sim 0°$–$360°$ are shown in Fig. 2. (The CO emission was summed in a $b = \pm 2°$ strip; 10 of the 37 associations in Table 1 are outside of this layer.) Also shown in the figure is the family of curves that determine the line-of-sight velocity of the Galactic rotation $V^*_{r,\mathrm{gal}}$ at each longitude for various heliocentric distances. To compare V_{LSR} and $V_{r,\mathrm{gal}}$, we applied a correction attributable to the difference between the velocity of the standard solar motion ($V_X = 10$ km s^{-1}, $V_Y = 15$ km s^{-1}, $V_Z = 7$ km s^{-1}) and the solar velocity obtained by

analyzing the motion of OB associations (see above). Therefore, the line-of-sight velocities $V_{\rm LSR}$ of molecular clouds and OB-association stars shown in Fig. 2, as well as $V^*_{r,\rm gal} = V_{r,\rm gal} + \Delta V_{\rm ap}$, were corrected for the solar motion toward the standard apex.

We see from Fig. 2 that, in general, the distribution of OB associations in the $(l, V_{\rm LSR})$ plane matches the distribution of CO emission. Most of the associations (Cyg OB1, OB3, OB8, and OB9; Cen OB1; Cru OB1; Cep OB1 and OB3; Cas OB2 and OB6) with the residual motions characteristic of the inner arms are projected onto giant molecular clouds. Note that some interarm associations (Cas OB8 and OB4, Car OB1, and Cma OB1) and the Car OB2 association in the outer arm are located in regions of reduced CO emission.

Molecular clouds have been repeatedly associated with OB associations (see, e.g., Dame *et al.* 1986). Giant molecular clouds near OB associations within 3 kpc of the Sun were identified by Efremov and Sitnik (1988). The boundaries of the bright CO emission features near the Perseus arm associations in the $(l, V_{\rm LSR})$ plane and the level of brightness from which they were determined according to the data of Dame *et al.* (2001) are given in columns 2–4 in Table 2. The molecular clouds of the Cygnus arm identified by the data of Leung and Thaddeus (1992) were studied in detail by Sitnik *et al.* (2001). In order not to lose the molecular clouds near far associations, they were identified at a lower level (see Fig. 2b and Table 2). Unfortunately, the available data do not allow the molecular clouds to be properly identified at the same level at which the velocity dispersion of OB-association stars was determined. In addition, molecular clouds are destroyed during star formation and under the ionizing radiation and winds from OB stars. Therefore, only cloud remnants are observed near associations. We only see from Fig. 2 that the line-of-sight velocity ($V_{\rm LSR}$) dispersion of OB-association stars and the velocity spread in bright parts of the nearest molecular clouds are at least of the same order of magnitude.

Since the stars of several OB associations move mainly with the same $V_{\rm LSR}$ as the molecular clouds onto which they are projected, the clouds and the associations may be assumed to be at the same or, at least, close Galactocentric distances. However, as was noted above, different molecular clouds that are located at different distances ($V_{r,\rm gal}$) and, accordingly, have different $V_{r,\rm res}$ can be observed at the same velocity $V_{\rm LSR}$ ($V_{\rm LSR} = V_{r,\rm gal} + V_{r,\rm res}$). Therefore, to assign photometric distances to molecular clouds, we used the H II regions that result from the propagation of ionization fronts in the interstellar medium. If an H II region was produced by OB-association stars and is projected onto a molecular cloud in the $(l, V_{\rm LSR})$ plane, then we can assume with confidence that the cloud is also located near this association. Columns 5–8 of Table 2 give Galactic coordinates and line-of-sight velocities of the H II regions ionized by stars of the associations in the second quadrant (Georgelin and Georgelin 1976; Sharpless 1959; Blaha and Humphreys 1989). We see from Tables 1 and 2 that, in general, the H II regions around the stars of an association are observed in the same line-of-sight velocity range as the stars of this association and the nearest molecular clouds.

Thus, to a first approximation, we can assign the photometric distances and residual line-of-sight velocities of the neighboring associations to the molecular clouds.

Figure 2 shows the distributions of CO emission and OB associations for the entire solar neighborhood, while we study in detail only the behavior of molecular gas in the Perseus arm.

The Effect of Streaming Motions on the Localization of Molecular Clouds in the Perseus Arm (Second Quadrant)

The spiral arms in the CO-emission distribution can be best traced in the range $l \sim 90°$–$180°$ (Fig. 2b) (Cohen *et al.* 1980; Casoli *et al.* 1984; Dame *et al.* 1986). Here, two chains of molecular clouds with OB associations projected onto them are observed at kinematic distances $R_{\rm kin} \leq 1$–1.5 kpc and $R_{\rm kin} \sim 2$–5 kpc. The near molecular clouds and the Cyg OB7 and Cep OB2 and OB3 associations are attributed to the Cygnus–Cepheus arm; the far molecular clouds and the Per OB1, Cas OB6, Cas OB2 and OB5, Cep OB1, and Aur OB1 associations are attributed to the Perseus arm.

Because of the large streaming line-of-sight motions ($V_{r,\rm res} \sim$ from -15 to -10 km s^{-1}), which coincide in direction with the Galactic rotation velocity $V^*_{r,\rm gal}$, the OB associations in the inner Perseus arm are observed at line-of-sight velocities that correspond to larger kinematic distances from the Sun than the kinematic distances to Cas OB4 and OB8 (Fig. 2b, Table 1). In contrast, the photometric distances to Cas OB4 and OB8, which, besides, have the residual kinematics typical of the objects near the outer boundary, are larger. Thus, these far Cas OB4 and OB8 associations with small residual motions at $V_{r,\rm res} \sim 3$ km s^{-1} (against $V^*_{r,\rm gal}$) are displaced only slightly in the $(l, V_{\rm LSR})$ plane and, curiously, are located in the interarm space between the Perseus and Local arms rather than beyond the Perseus arm.

However, the molecular clouds of the Perseus arm in the $(l, V_{\rm LSR})$ plane must also be displaced by streaming motions toward larger distances. At

Table 2

Association	Δl_{CO}	ΔV_{LSR}, km s^{-1}	$\log \int T_{mb} db$, K arcdeg [12]	H II region	l	b	V_{LSR}, km s^{-1}
Cep OB2	–	–	–	S131	99.3	3.8	−2.2
							−14.3
				S140	106.8	5.3	−10.0
Cep OB1	108.0–109.0	−58 to −48	≥0.1	S132	103.0	0.7	−50.9
				S142	107.1	−0.9	−35.8
Cep OB3				S155	110.2	2.6	−15.1
Cas OB2	109.5–112.0	−60 to −35	≥0.1	S157	111.2	−0.7	−37.7
				S157A	111.3	−0.7	−46.0
				S162	112.2	0.2	−42.3
Cas OB5	113.5–114.5	−50 to −40	≥0.1				
Cas OB4	117.5–119	−40 to −30	<0.1	S173	119.4	−0.9	−37.0
Cas OB8	128.5–129.5	−40 to −30	<0.1				
Cas OB6	133.5–134.0	−50 to −40	≥0.1	S190	133.7	1.0	−38.7
							−40.7
							−46.0
							−44.0
	136.5–137	−42 to −36	≥0.1	S199	137.5	1.1	−36.6
							−36.9
Cam OB1				S202	140.6	1.9	−18.9
				S205	148.5	−0.2	−18.2

the same time, the clouds of the interarm space beyond this arm must be displaced toward smaller distances, although only slightly. As a result, the clouds of the Perseus arm and the interarm space beyond it can "switch places," as was the case with the associations. Therefore, the observed (l, V_{LSR}) distribution of molecular clouds in the Perseus arm cannot be treated as a concentration of molecular clouds toward the outer edge of this arm, as follows from a comparison of only the photometric distances to the associations with kinematic distances to the clouds.

There is also independent evidence that the bright molecular–dust clouds of the Perseus arm are not farther than the associations, as it may seem from a kinematic distance estimate $R_{kin} \geq 2.5$ kpc (see Fig. 2b). According to Neckel and Klare (1980), the interstellar extinction in the direction $l \sim 90°–140°$ is highest in the Local arm (i.e., within 1 kpc). In several directions (in particular, toward Cas OB2 and OB6, with which the molecular clouds are associated), a second increase in the interstellar extinction A_V is observed at a distance up to $R_{phot} \sim 2$ kpc, indicating that the clouds are localized in front of these associations. According to Blaha and Humphreys (1989), a small increase in A_V is observed for the stars that are located near the molecular–dust clouds associated with Cas OB2 and OB6 ($R_{phot} \leq 2$ kpc). Unfortunately, there are no stars of these associations toward the clouds. Studies of the dust distribution toward the H II regions IC 1795 and IC 1805 ionized by Cas OB6 stars also showed that the bulk of the extinction is attributable to foreground dust clouds (Kolesnik 1987, 1988).

Thus, if the distribution of molecular clouds in Fig. 2b is considered in terms of a purely circular Galactic rotation, then the kinematic distances to the molecular clouds of the Perseus arm turn out to be much larger than not only the photometric distances to the associations associated with them but also the kinematic distances to the molecular clouds onto which the interarm associations beyond this arm are projected. A correction for the streaming motions

(and the interstellar extinction) displaces the molecular clouds, along with the associations of the Perseus arm, into the inner part of this arm and the molecular clouds onto which the far interarm associations onto which they are projected into a region near the outer boundary or beyond the Perseus arm.

A similar inversion of the near and far molecular clouds in the $(l, V_{\rm LSR})$ plane was previously found in the Cygnus arm (Sitnik *et al.* 2001). A correction for the streaming motions of stars and gas here decreased the distance by ~2 kpc (by a factor of 3) to one of the clouds and changed their relative positions with respect to the Sun.

Molecular Clouds in the Outer Galaxy (Third Quadrant)

The spiral structure in the third quadrant is identified neither by the spatial distribution of associations nor by their residual motions (Fig. 2a). All of the associations Gem OB1, Mon OB1 and OB2, Cma OB1, Vela OB1, and Ori OB1, with the possible exception of Coll 121 and Vela OB2, have kinematics typical of the interarm space (see Table 1) and do not belong to the extension of the Perseus arm expected in the third quadrant. However, all of the above associations are observed within $R \leq 1.5$ kpc, whereas the Perseus arm lies much farther.

Most of the associations in the third quadrant completely or partially lie outside the CO-emission layer shown in Fig. 2a (Table 1). Therefore, comparing the distributions of OB associations and molecular clouds, we note only the following. The bulk of the CO emission in the region $l \sim 180°-270°$ is emitted in the range $\Delta V_{\rm LSR} \sim 0-30$ km s^{-1} (Fig. 2a). The stars of all of the associations shown in Fig. 2a, including Gem OB1, Mon OB1 and OB2, Cma OB1, and Vela OB1 located, at least partially, within $-2° \leq b \leq 2°$ (Table 1) move with the same line-of-sight velocities. Because of the small residual velocities ($V_{r,\rm res} \sim 2-4$ km s^{-1}) compared to the line-of-sight velocity dispersion, the displacement of Gem OB1, Cma OB1, Vela OB1, and the interarm clouds associated with them in the $(l, V_{\rm LSR})$ plane is invisible (Fig. 2a). A large line-of-sight velocity dispersion ($\sigma \sim 13$ km s^{-1}) is observed in the Mon OB1 and OB2 associations, which are located at different distances (0.6 and 1.2 kpc) but are projected onto each other both in the plane of the sky and the $(l, V_{\rm LSR})$ plane. This dispersion, as well as the same median line-of-sight velocities, of these associations located at different distances from the Sun may be attributable to the erroneous assignment of stars in the near association to the far association and vice versa. Therefore, the isolated and, at first glance, clearly identifiable molecular clouds in Fig. 2a onto which Mon OB1 and OB2 are projected can actually be both a superposition of the clouds at different distances along the line of sight associated with each of the associations and a separate cloud near one of them. The analysis of the optical extinction by Neckel and Klare (1980) gave no unique answer.

CONCLUSIONS

Our analysis of the streaming motions of OB associations and associated molecular clouds has indicated that spiral density waves can significantly change the distribution of these objects in the $(l, V_{\rm LSR})$ plane. The observed distribution depends on the relationship between $V^*_{r,\rm gal}$ and $V_{r,\rm res}$. In turn, the magnitude and direction of $V_{r,\rm res}$ depend on the position of the object being studied in the arm cross section or in the interarm space, on the orientation of the arm or the interarm space relative to the line of sight. A knowledge of the line-of-sight velocities and distances for OB associations, as well as their residual space velocities, allowed the residual motions of the molecular clouds near these associations to be estimated. The most favorable conditions for studying the residual motions were found in the Perseus and Cygnus arms, because $V_{r,\rm res}$ for the OB associations and molecular clouds in the inner parts of these arms is at a maximum.

The spiral arms in the Galaxy are often identified by the spatial concentration of OB associations, H II regions, molecular clouds, or clouds of neutral hydrogen. However, since peculiar streaming motions are characteristic of the wave arms, a wave arm must be identified primarily by its kinematics. Studies of the streaming motions of associations showed that only two thirds of the OB associations are in the arms (Melnik *et al.* 2001). These associations are associated with giant molecular clouds by which, according to many researchers (e.g., Dame *et al.* 2001), the spiral structure can be traced in the $(l, V_{\rm LSR})$ plane. Nevertheless, not only OB associations but also many molecular clouds identified by the CO-emission distribution are observed outside the arms as well (e.g., in the third quadrant).

The following main conclusion can be drawn from our comparative analysis of the $(l, V_{\rm LSR})$ distributions of OB assocuiations and molecular clouds in a large-scale solar neighborhood. In general, the line-of-sight velocity ranges in which the stars of an OB association, the H II regions ionized by stars of this association, and the nearest molecular clouds are observed overlap (Tables 1 and 2; Fig. 2; see also Sitnik *et al.* 2001). This result is to be expected, because it is a consequence of the physical and genetic relationship between these objects. Note also that the large stellar line-of-sight velocity dispersion ($\sigma_{V_{\rm LSR}} \sim$

13–20 km s^{-1}) for a number of associations (Ser OB1 and OB2, Sct OB2, Vul OB1, Aur OB1, Mon OB1 and OB2, Cma OB1, Cen OB1, Ara OB1A, and Sco OB1) can imply that not all of the stars are members of these associations.

The streaming motions in the Perseus arm attributable to density waves made the following changes to the $(l, V_{\rm LSR})$ distribution of CO emission (Fig. 2).

(1) The distances to objects of the Perseus arm and the interarm space are inverted. For example, the Perseus arm associations are observed at line-of-sight velocities that correspond to larger kinematic distances than the kinematic distances to the actually far interarm associations beyond this arm. Thus, in the $(l, V_{\rm LSR})$ plane, not only the associations of the Perseus arm and the interarm space beyond it but also the molecular clouds associated with them can switch places. In this case, the population of the Perseus arm proves to be displaced toward larger distances by ~ 2 kpc because of streaming motions, while the far interarm OB associations beyond the Perseus arm and the molecular clouds associated with them fall into the region between the Perseus and Cygnus–Cepheus arms.

(2) It may seem from comparison of the distances, the photometric ones to OB associations and the kinematic ones to molecular clouds, that the molecular clouds are concentrated in the $(l, V_{\rm LSR})$ plane to the outer boundary of the Perseus arm. (This conclusion has previously been reached repeatedly, including by the author.) However, the equal line-of-sight velocities of the OB associations and the associated molecular clouds, as well as the corrections for streaming motions and interstellar extinction, suggest that these objects are at the same distances.

(3) An anomalously large CO surface density contrast (25 : 1) is observed in the Perseus arm and the interarm space in front of this arm (Digel *et al.* 1996). The region of reduced CO surface density in the range $l \sim 120°$–$140°$, $V_{\rm LSR} \sim 20$–30 km s^{-1} (Fig. 2b), could be formed in part due to the inversion noted in (1). This means that the CO clouds (along with the associations) of the Perseus arm were swept out of this region in the $(l, V_{\rm LSR})$ plane by streaming motions toward larger distances, while the far clouds that must fall here are either few in number or the CO emission from these clouds is below the sensitivity threshold of the survey by Dame *et al.* (2001).

Previously, Sitnik *et al.* (2001) detected the streaming motions of OB stars, molecular clouds, and ionized hydrogen in the Cygnus arm, which also led to an inversion of the distances to the two complexes of stars and gas identified here. Thus, one of the molecular cloud complexes was displaced toward larger distances by $\sim$2 kpc, while the other complex was displaced only slightly. Given the line-of-sight velocities of the Galactic rotation and the residual line-of-sight velocities of the Cen OB1 and Cru OB1 or Sgr OB1, Ser OB1 and OB2, and Sct OB2 associations, one might expect the molecular clouds associated with these associations in the $(l, V_{\rm LSR})$ plane to be brought closer to the Sun by streaming motions with $V_{r,\rm res} \sim 5$–8 km s^{-1} and $V_{r,\rm res} \sim (-24)$–(-8) km s^{-1}, respectively (see Table 1, Figs. 2a and 2d).

Thus, our comparative analysis of the $(l, V_{\rm LSR})$ distributions of OB associations and molecular clouds suggests a significant effect of streaming motions and confirms that they should be taken into account when transforming the observational data for interstellar clouds in the $(l, V_{\rm LSR})$ plane into a spatial distribution. The observed large-scale distribution of CO emission in the $(l, V_{\rm LSR})$ plane can be explained in terms of the theory of spiral density waves based on the detected large-scale periodicity of the variations in the residual velocities of OB associations in space because of streaming motions. I would like to note that the radial or azimuthal expansions of the large-scale (comparable to the arm cross section) gaseous envelopes around young associations with a velocity no higher than 20 km s^{-1} could actually result from the residual motions produced by density waves.

ACKNOWLEDGMENTS

This study was supported by the Russian Foundation for Basic Research (project nos. 01-02-16118 and 02-02-16667) and the Federal Research and Technology Program (project no. 40.022.1.1.1102). I am grateful to K.V. Bychkov, G.M. Rudnitskii, and A.S. Rastorguev for helpful remarks and particularly to A.M. Melnik for numerous helpful discussions and help in preparing the materials.

REFERENCES

1. D. S. Adler and W. W. Roberts, Astrophys. J. **384**, 95 (1992).
2. M. Barbier-Brossat and P. Figon, Astron. Astrophys., Suppl. Ser. **142**, 217 (2000).
3. L. N. Berdnikov, Perem. Zvezdy **22**, 505 (1987).
4. L. N. Berdnikov, A. K. Dambis, and O. V. Vozyakova, Astron. Astrophys., Suppl. Ser. **143**, 211 (2000).
5. C. Blaha and R. M. Humphreys, Astron. J. **98**, 1598 (1989).
6. W. B. Burton, Astron. Astrophys. **10**, 76 (1971).
7. F. Casoli, F. Combes, and M. Gerin, Astron. Astrophys. **133**, 99 (1984).
8. R. S. Cohen, H. I. Cong, T. M. Dame, and P. Thaddeus, Astrophys. J. **239**, L53 (1980).
9. A. K. Dambis, A. M. Melnik, and A. S. Rastorguev, Pis'ma Astron. Zh. **21**, 331 (1995) [Astron. Lett. **21**, 291 (1995)].

10. A. K. Dambis, A. M. Melnik, and A. S. Rastorguev, Pis'ma Astron. Zh. **27**, 68 (2001) [Astron. Lett. **27**, 58 (2001)].
11. T. M. Dame, H. Ungerechts, R. S. Cohen, *et al.*, Astrophys. J. **322**, 706 (1987).
12. T. M. Dame, D. Hartmann, and P. Thaddeus, Astrophys. J. **547**, 792 (2001).
13. S. W. Digel, D. A. Lyder, A. J. Philbrick, *et al.*, Astrophys. J. **458**, 561 (1996).
14. Yu. N. Efremov and T. G. Sitnik, Pis'ma Astron. Zh. **14**, 817 (1988) [Sov. Astron. Lett. **14**, 347 (1988)].
15. C. D. Garmany and R. E. Stencel, Astron. Astrophys., Suppl. Ser. **94**, 214 (1992).
16. J. P. Georgelin and J. M. Georgelin, Astron. Astrophys. **49**, 57 (1976).
17. E. V. Glushkova, A. K. Dambis, A. M. Melnik, and A. S. Rastorguev, Astron. Astrophys. **239**, 514 (1998).
18. L. N. Kolesnik, Kinemat. Fiz. Neb. Tel **3**, 62 (1987).
19. L. N. Kolesnik, Kinemat. Fiz. Neb. Tel **4**, 13 (1988).
20. H. O. Leung and P. Thaddeus, Astrophys. J., Suppl. Ser. **81**, 267 (1992).
21. C. C. Lin, C. Yuan, and F. H. Shu, Astrophys. J. **155**, 721 (1969).
22. Y. S. Liszt and W. B. Burton, Astrophys. J. **243**, 778 (1981).
23. A. M. Melnik, T. G. Sitnik, A. K. Dambis, *et al.*, Pis'ma Astron. Zh. **24**, 689 (1998) [Astron. Lett. **24**, 594 (1998)].
24. A. M. Melnik, A. K. Dambis, and A. S. Rastorguev, Pis'ma Astron. Zh. **27**, 611 (2001) [Astron. Lett. **27**, 521 (2001)].
25. Th. Neckel and G. Klare, Astron. Astrophys., Suppl. Ser. **42**, 251 (1980).
26. A. S. Rastorguev, O. V. Durlevich, E. D. Pavlovskaya, and A. A. Filippova, Pis'ma Astron. Zh. **20**, 688 (1994) [Astron. Lett. **20**, 591 (1994)].
27. A. S. Rastorguev, E. V. Glushkova, A. K. Dambis, and M. V. Zabolotskikh, Pis'ma Astron. Zh. **25**, 689 (1999) [Astron. Lett. **25**, 595 (1999)].
28. W. W. Roberts, Astrophys. J. **158**, 123 (1969).
29. S. Sharpless, Astrophys. J., Suppl. Ser. **4**, 257 (1959).
30. T. G. Sitnik and A. M. Melnik, Pis'ma Astron. Zh. **22**, 471 (1996) [Astron. Lett. **22**, 422 (1996)].
31. T. G. Sitnik and A. M. Melnik, Pis'ma Astron. Zh. **25**, 194 (1999) [Astron. Lett. **25**, 156 (1999)].
32. T. G. Sitnik, A. M. Melnik, and V. V. Pravdikova, Astron. Zh. **78**, 40 (2001) [Astron. Rep. **45**, 34 (2001)].
33. The Hipparcos and Tycho Catalogues, European Space Agency **1–20** (1997).

Translated by V. Astakhov

Astronomy Letters, Vol. 29, No. 5, 2003, pp. 321–335. Translated from Pis'ma v Astronomicheskiĭ Zhurnal, Vol. 29, No. 5, 2003, pp. 367–383.

Mechanisms of the Vertical Secular Heating of a Stellar Disk

N. Ya. Sotnikova* **and S. A. Rodionov**

Astronomical Institute, St. Petersburg State University,
Universitetskii pr. 28, Petrodvorets, St. Petersburg, 198904 Russia

Received November 30, 2002

Abstract—We investigate the nonlinear growth stages of the bending instability in stellar disks with exponential radial density profiles. We found that the unstable modes are global (the wavelengths are larger than the disk scale lengths) and that the instability saturation level is much higher than that following from a linear criterion. The instability saturation time scales are of the order of one billion years or more. For this reason, the bending instability can play an important role in the secular heating of a stellar disk in the z direction. In an extensive series of numerical N-body simulations with a high spatial resolution, we were able to scan in detail the space of key parameters (the initial disk thickness z_0, the Toomre parameter Q, and the ratio of dark halo mass to disk mass $M_\mathrm{h}/M_\mathrm{d}$). We revealed three distinct mechanisms of disk heating in the z direction: bending instability of the entire disk, bending instability of the bar, and heating on vertical inhomogeneities in the distribution of stellar matter. © *2003 MAIK "Nauka/Interperiodica".*

Key words: *galaxies, groups and clusters of galaxies, intergalactic gas.*

STELLAR RELAXATION IN THE DISKS OF SPIRAL GALAXIES

According to the theory of stellar evolution, the correlation between the spectral types of stars in the solar neighborhood and their kinematic parameters found more than half a century ago (Parenago 1950) is the reflection of another correlation—between the stellar age and the random velocity dispersion (for a review of the currently available data, see, e.g., Fuchs *et al.* 2000). The latter correlation has the following pattern: the velocity dispersion for old stars is, on average, larger than that for young stars. All stars are born with a small spread in random velocities (about 5–10 km s^{-1}). In this case, the increase in the velocity dispersion with time (dynamic heating) is the reflection of a random scattering of stars (continuous or occasional) by massive objects or large-scale density inhomogeneities.

Two pioneering studies (Spitzer and Schwarzshild 1951, 1953), in which large gaseous structures discovered twenty years later as giant molecular clouds (GMCs) from CO observations were postulated as scattering objects, were based on this idea. Subsequently, other relaxation mechanisms, for example, interaction with close satellites, were also suggested. The latter mechanism relies on observational data, according to which the disks of galaxies in interacting systems are a factor of 1.5 or 2 thicker than the disks of isolated galaxies (Reshetnikov and Combes 1997). Its efficiency is confirmed by numerical simulations (Walker *et al.* 1999; Velazquez and White 1999).

For isolated galaxies, apart from scattering by GMCs, the heating on inhomogeneities in the distribution of stellar matter that arise during the development of internal instabilities in the disk itself is commonly considered. The heating can be produced by transient spiral arms or a growing bar and by bending instability.

In suggesting a particular dynamic heating mechanism, the following two well-established observational facts should be borne in mind.

(1) The stellar velocity dispersion depends on time as $\sigma_\mathrm{tot} \propto t^\alpha$, where σ_tot is the three-dimensional velocity dispersion and $\alpha \approx 0.33$–0.5 (Fuchs *et al.* 2000; Binney *et al.* 2000).

(2) The ratio of the vertical and radial stellar velocity dispersions is $\sigma_z/\sigma_R < 1$.

The second fact requires an explanation. It is well known that in an equilibrium axisymmetric galaxy in the absence of the third integral of motion, σ_z and σ_R must be equal at a given point of the disk (see, e.g., Saslaw 1985). Observational data indicate that this is not the case. The σ_z/σ_R ratio for stars in the solar neighborhood does not depend on their spectral type (and, hence, on their age) and is $\sigma_z/\sigma_R = 0.53 \pm 0.07$ (see, e.g., Dehnen and Binney 1998). Until recently, no similar data have been available for external galaxies. At present, this ratio is known for two more

*E-mail: NS2217@NS2217.spb.edu

nearby galaxies:[1] $\sigma_z/\sigma_R = 0.70 \pm 0.19$ for NGC 488 (morphological type Sb) (Gerssen *et al.* 1997) and $\sigma_z/\sigma_R = 0.85 \pm 0.1$ for NGC 2985 (morphological type Sab) (Gerssen *et al.* 2000); i.e., it increases as one passes to earlier-type galaxies.

Spitzer and Schwarzshild (1951, 1953) showed that when stars are scattered by GMCs, the stellar velocity dispersion increases as $\sigma_{\rm tot} \propto t^{1/3}$; i.e., the exponent corresponds to the lower limit of this quantity, which is still in agreement with observational data. If, however, we take into account the fact that the GMCs are confined in a thin layer and the stars lie outside this layer most of the time, then the efficiency of the relaxation mechanism associated with GMCs becomes even lower: $\sigma_{\rm tot} \propto t^{0.25}$ (Lacey 1984). At the same time, GMCs are capable of effectively converting the energy of random motions in the disk plane into the energy of random motions in the perpendicular direction. Lacey (1984) found that when stars are scattered by GMCs, a ratio $\sigma_z/\sigma_R \approx 0.8$ is rapidly established. This ratio is much larger than the value observed for the solar neighborhood, although it is close to that obtained for the galaxy NGC 2985. However, no CO-line emission was detected for this galaxy (see, e.g., Merrifield *et al.* 2001).

As regards the spiral arms, numerical simulations (the first numerical results were obtained by Sellwood and Carlberg 1984) and analytical calculations (Binney and Lacey 1988; Jenkins and Binney 1990; Jenkins 1992) show good agreement between the theoretical and observational age–velocity dispersion relations. However, the following should be remembered: in the above theoretical studies, the spiral arms were assumed to effectively scatter stars only in the disk plane. Additional mechanisms are commonly invoked to convert part of the energy in the disk plane into the energy of vertical motions. The combined effect from spiral arms and GMCs yields a result that is in good agreement with observational data (Binney and Lacey 1988), but this does not rule out other vertical disk heating mechanisms. For isolated galaxies, bending instability can serve as such a mechanism. In addition, as we show below, spiral arms are capable of producing density inhomogeneities in the z direction. The interaction of stars with these density enhancements also result in an increase of σ_z.

Here, we study in detail the nonlinear growth stages of bending instability and show that it can be responsible for the secular increase of the stellar velocity dispersion in the vertical direction.

[1] In both cases, we give galaxy-averaged data.

BENDING INSTABILITY AS A MECHANISM OF THE SECULAR HEATING OF STELLAR DISKS

The Linear Theory

Stellar disks are known to be unstable against the formation of spiral arms and bars. In addition, conditions for the growth of bending instability exist in thin equilibrium disks. This instability arises in systems with highly anisotropic particle motions and is similar to the fire-hose instability in plasma.

The bending instability of an infinitely thin gravitating layer with a nonzero velocity dispersion was first investigated by Toomre (1966). Toomre is believed to have been sceptical about his results. Therefore, they were published in a barely accessible paper and only several years ago did they become widely known after their detailed presentation by Merrit and Sellwood (1994). The bending instability of flat stellar systems has been rediscovered several times. Kulsrud *et al.* (1971) independently obtained a result similar to that of Toomre (1966). As regards equilibrium cold disks (with a zero velocity dispersion), Hunter and Toomre (1969) showed that they (in contrast to hot disks) are stable against the growth of bending perturbations. This fact had long been misused as an argument against any astrophysical applications related to bending instability. Only in 1977 did Polyachenko and Shukhman construct an exact linear theory for a homogeneous thin layer with a nonzero stellar velocity dispersion. A more realistic model of a thin layer with the vertical density profile described by the function $\mathrm{sech}^2(z/z_0)$ was analyzed by Araki (1985).[2]

Toomre (1966) was the first to derive the dispersion relation for long-wavelength ($\lambda = 2\pi/k \gg h$, where $2h$ is the layer thickness) bending perturbations

$$\omega^2 = 2\pi G\Sigma|k| - \sigma_x^2 k^2, \qquad (1)$$

where Σ is the surface density of the layer stars and σ_x^2 is the velocity dispersion along a particular coordinate in the layer plane. It follows from Eq. (1) that perturbations with wavelengths $\lambda > \lambda_J \equiv \sigma_x^2/G\Sigma$ are stable, because $\omega^2 > 0$ in this range.

Short-wavelength perturbations

$$\lambda < \lambda_2 \approx h\frac{\sigma_x}{\sigma_z} = h\alpha,$$

where

$$\alpha \equiv \sigma_x/\sigma_z \qquad (2)$$

[2] The presentation of the results of this analysis by Sellwood and Merritt (1994) made it accessible for a wide circle of researchers.

is the control parameter of the bending instability, must also be stable. In this case, the time of one vertical stellar oscillation, $t_\perp = h/\sigma_z$, is longer than the time it takes for the star to traverse one wavelength, $t_\parallel = \lambda/\sigma_x$. Therefore, the star traverses a distance of several wavelengths in the time $t_\perp$. As a result, a mismatch in the coherent particle motion arises, causing the perturbation to decay. Intermediate-wavelength ($\lambda_2 < \lambda < \lambda_J$) perturbations are unstable; the bending only grows.

When $\lambda_2 = \lambda_J$, the instability region disappears and the disk becomes stable against bending perturbations of any wavelengths. The following analytical estimate is valid for the parameter α defined by formula (2) in the linear approximation (Toomre 1966; Kulsrus *et al.* 1971; Polyachenko and Shukhman 1977; Araki 1985)

$$\lambda_2 = \lambda_J \quad \text{for} \quad \alpha = \alpha_{\rm cr} \approx 3.0$$

or

$$(\sigma_z/\sigma_x)_{\rm cr} \approx 0.3. \qquad (3)$$

The instability is completely suppressed for $\sigma_z/\sigma_x > 0.3$ and grows for $\sigma_z/\sigma_x < 0.3$.

Stars are born out of a gaseous medium and initially have low random velocities. The increase of the velocity dispersion in the radial and azimuthal directions through scattering by spiral density waves can lead to an anisotropy of the particle motions in the plane and in the vertical direction. As a result, bending instability can develop in the disk; this instability causes an increase in σ_z to the level corresponding to instability saturation and an increase in the stellar-disk thickness. The linear criterion gives a low instability saturation level (3). However, as was mentioned above, $\sigma_z/\sigma_R \approx 0.5$ in the solar neighborhood. That is why Toomre was sceptical about his discovery. However, the following two things should be remembered. First, $(\sigma_z/\sigma_R)_{\rm cr} \approx 0.3$ was obtained from a linear analysis. Numerical studies of the nonlinear growth stages of bending instability (Raha *et al.* 1991; Sellwood and Merritt 1994; Merrit and Sellwood 1994; and our numerical results) show that the instability is saturated at much larger σ_z/σ_R. Second, the growth rate of the instability is very low. The saturation time scales are several billion years.

For these two reasons, bending instability can play an important role in the secular disk heating in the z direction.

The Numerical Model

A high spatial resolution in the z direction is required to properly simulate the growth of bending instability in numerical simulations. In the N-body problem, this is possible only for a large number of gravitationally interacting particles. In the first numerical models, N was taken to be 100 000 (Raha *et al.* 1991; Sellwood and Merritt 1994; Merrit and Sellwood 1994). We used a considerably larger number of particles, $N = 300\,000$–$500\,000$, which made it possible to reach a higher resolution and to trace the evolution of the stellar disk on time scales of about 5 Gyr. In addition, our model of a disk galaxy is much more realistic: we considered a rotating disk with an exponential density profile and assumed the existence of an additional spherical component (a dark halo). Finally, we scanned in detail the space of control parameters (see the next section) and found many of the growth features of bending instability that were overlooked in both the linear analysis and the numerical simulations.

In our numerical simulations, we simulated the evolution of an isolated disk galaxy by using an algorithm that is based on the data structuring in the form of an hierarchical tree[3] (Barnes and Hut 1986). Its implementation was taken from the NEMO package (http://astro.udm.edu/nemo; Teuben 1995). The package was adapted to personal computers and significantly expanded by including original data analysis and visualization programs.

In specifying a galaxy model, we separated two subsystems: the stellar disk and the spherically symmetric component (a dark halo). Star formation was disregarded. The disk was represented as a system of gravitating bodies with R and z density profiles, which corresponds to the observed brightness profiles for spiral galaxies:

$$\rho_{\rm d}(R,z) = \frac{M_{\rm d}}{4\pi h^2 z_0} \exp\left(-\frac{R}{h}\right) {\rm sech}^2\left(\frac{z}{z_0}\right), \quad (4)$$

where h is the exponential disk scale length, z_0 is the typical scale of density variation in the z direction, and $M_{\rm d}$ is the total disk mass.

The spherical component was described in terms of the external static potential

$$\Phi_{\rm h}(r) = -\frac{v_\infty^2}{2} \ln(r^2 + a_{\rm h}^2), \qquad (5)$$

where $a_{\rm h}$ is the typical scale and v_∞ is the velocity of a particle on a circular orbit in this potential for $r \to \infty$ (v_∞ can be expressed in terms of the halo mass within a sphere of a given radius and parameter $a_{\rm h}$).

We specified the initial particle velocities (the rotation velocity and the random component) on the basis of equilibrium Jeans equations using a standard technique with a specified dependence $\sigma_R^2 \propto \Sigma(R)$, where $\Sigma(R)$ is the disk star surface density (see, e.g., Hernquist 1993).

[3] This scheme is called a tree method.

Initial parameters of the numerical models

$M_h(4h)/M_d(4h)$	z_0, kpc	Q		
		1.5	2.0	2.2
3.0	0.1	9_1	12	
1.5	0.1	24	27_1	33
0.85	0.1	22	23	31
	0.25	28	29, 29_1	
0.6	0.1	8, 8_1	11, 11_1, 11_2, 11_3	20
	0.25	21		
	0.3		26, 26_1	
	0.4	30		
	0.5		32	

All of the parameters specified in a numerical simulation can be divided into three groups: input parameters of the algorithm for solving the N-body problem, parameters of the initial model, and control parameters of the problem (the parameters that significantly affect the processes under consideration).

(1) Parameters of the algorithm are as follows: $\delta t = 0.5 \times 10^6$ yr (0.25×10^6 yr) is the integration step; $T_{\rm end} = 3000$–5000 Myr is the total integration time, $\theta = 0.7$ is the parameter responsible for the accuracy of calculating the force (see, e.g., Hernquist 1987); in addition, in our computations, we took not one but the first two terms in the Laplace expansion of the potential: the monopole and quadrupole terms (Hernquist 1987); $\varepsilon = 0.02$ kpc is the potential smoothing parameter.

(2) Parameters of the initial model are as follows: $h = 3.5$ kpc is the exponential disk scale length; $a_h = 2$ kpc is the dark-halo scale parameter; and $M_d = (4$–$8) \times 10^{10} M_\odot$ is the disk mass.

(3) Control parameters of the problem. Let us consider them in more detail.

(A) $z_0 = 0.1$–0.5 kpc is the initial disk half-thickness (this quantity can be related to the initial velocity dispersion σ_z by assuming that the system is vertically isothermal, $\sigma_z^2 = \pi G z_0 \Sigma(R)$). Since we are concerned with the increase of the stellar velocity dispersion in the z direction, we constructed an initially thin equilibrium galaxy with a small value of z_0. This, in turn, implies a small velocity dispersion in the z direction. Next, we observed the development of bending instability, which leads to stellar relaxation. By varying z_0, we were able to determine the instability saturation level independent of the initial conditions.

The assumption that the system is isothermal and the dependence $\sigma_R^2 \propto \Sigma(R)$ taken from empirical considerations yields the relation $\sigma_z/\sigma_R = \text{const}$ for the initial time. The ratio σ_z/σ_R has always been lower than the value that follows from the linear criterion for bending instability. As a result, we were able to subsequently analyze the instability saturation level for various R.

(B) $Q_{8.5} = 1.5$–2.2 is the Toomre parameter (Toomre 1964) at $R_{\rm ref} = 8.5$ kpc (this quantity characterizes the initial radial velocity dispersion at this radius $R_{\rm ref}$). It follows from the dependence $\sigma_R^2 \propto \Sigma(R)$ that

$$Q = \sigma_R/\sigma_R^{\rm cr} \propto \Sigma^{1/2}\frac{\kappa}{\Sigma} \propto \kappa(R)\exp(R/2h),$$

where κ is the epicyclic frequency; i.e., in contrast to σ_z/σ_R, Q is not constant for the entire disk. The function $Q(R)$ for an exponential disk has a broad maximum in the range $h < R < 3h$ (see Fig. 1 in Hernquist 1993). Specifying Q at $R_{\rm ref} \approx 2.5h \approx 8.5$ kpc gives the condition $Q(R) \geq Q_{8.5}$. This condition, in turn, ensures a level of stability against perturbations in the disk plane that is not lower than the level specified at $R_{\rm ref}$.

We were concerned with two cases:

— a large value of $Q_{8.5} \approx 2.0$ or, in other words, a large initial radial velocity dispersion at which the formation of a bar in the disk is suppressed; this allows the development of bending instability to be traced in pure form (without the influence of a bar).

— a moderate value of $Q_{8.5} \approx 1.5$; in this case, the disk is unstable against the growth of a bar mode and we were able to investigate the influence of a bar on the relaxation in the z direction.

(C) $M_h(4h)/M_d(4h) = 0.6$–3.0 is the ratio of dark-halo mass to disk mass within a sphere of radius $4h$. The spherical component is a stabilizing factor during the development of bending instability; we consider its influence on the secular galaxy heating in the section entitled "Stellar relaxation in models...."

For our computations, we used PC-compatible computers of the Astronomical Institute of St. Petersburg State University. Some of the numerical simulations were carried out in cluster mode. The table gives the numbers of all of the models analyzed below.[4]

[4] The models with equal control parameters have different random realizations of the initial conditions—particle positions and random velocities.

Results of the Numerical Simulations

We carried out a large series of stellar-dynamics simulations and studied the growth of bending instability in thin stellar disks as a function of the control parameters of the problem. Analysis of the results of our computations revealed three distinct mechanisms of stellar relaxation in the vertical direction. The following system of units is used in all of the figures that illustrate our conclusions: the unit of time is 1 Myr, the unit of velocity is 978 km s^{-1}, and the unit of length is 1 kpc.

Large-scale bending instability of the disk. The large-scale bending instability of the entire disk is the first galaxy heating mechanism. It is most typical of galaxies with low-mass spherical components that are initially hot in the plane, i.e., of galaxies in which the formation of a bar was suppressed (for bar-mode suppression mechanisms, see, e.g., the monograph of Binney and Tremaine 1987).

Below, we describe the scenario for the development of bending instability using Model 26_1 as an example. All of the key evolutionary features of the stellar disk that were shown by this model were also observed in other hot models.

If we decompose $\overline{z(R)}$ (the mean particle deviation from the $z = 0$ plane) into Fourier harmonics, $\bar{z}_m(R) = A_m \exp(-im\varphi)$, then we can calculate the amplitudes of the first three harmonics ($m = 0$ is the axisymmetric bending or, alternatively, the bell mode; $m = 1$ is the bending mode; and $m = 2$ is the saddle-type mode). The change of A_m with time describes the various bending formation stages shown in Figs. 1 and 2 (left panels). These stages are more clearly distinguished in the color two-dimensional histograms that can be found at http://www.astro.spbu.ru/staff/seger/articles/warps_2002/fig1_web.html. In these histograms, the mean disk particle deviation from the $z = 0$ plane is represented by different colors (the shades of yellow and blue indicate upward and downward deviations, respectively). We see in Figs. 1 and 2 (as in the two-dimensional histograms) that a large-scale bending is produced in the galaxy at a time $t \approx 200$ Myr. At $t \approx 400$ Myr, the bending amplitude reaches its local maximum. The bending perturbation wavelength (the radial extent) is comparable to the disk scale length. The bending is not axisymmetric; the amplitude of the zero mode, i.e., the mode with the azimuthal number $m = 0$, is small, at least less than the amplitudes of other harmonics. This relationship between the harmonic amplitudes is preserved until $t \approx 800$ Myr.

Next, a steadily growing axisymmetric bending mode ($m = 0$) is clearly revealed, while all of the still large (in amplitude) nonaxisymmetric modes ($m = 1$ and $m = 2$) are displaced to the galactic periphery. Subsequently ($t = 800$–1200 Myr), the nonaxisymmetric bending modes are gradually damped, while the axisymmetric bending reaches its maximum ($t = 1000$ Myr).

For the subsequent 1500 Myr of its evolution, the disk freezes in a shape similar to the shape of circles on water. A similar vertical disk structure, with box-shaped iosphotes in central regions, was also observed in the numerical simulations of Sellwood and Merritt (1994) for initially hot Kuzmin–Toomre disk models and in other simulations in which the bar formation was suppressed through a large Toomre parameter Q (Patsis *et al.* 2002). In our computations, the amplitude of the axisymmetric bending slowly decreased and, to all appearances, the bending must subsequently disappear altogether.

Two evolutionary stages of the bending can be separated in this model: the initial stage with a nonaxisymmetric bending and the main stage with an axisymmetric bending.

Let us turn to the plot of the vertical (σ_z) and radial (σ_R) velocity dispersions against time (Fig. 3a). The value of σ_z approximately doubled in time $t = 3000$ Myr. Two times of rapid increase in the velocity dispersion σ_z can be distinguished: one at $t \approx 500$ Myr (the time the amplitude of the initial nonaxisymmetric bending reaches its maximum) and the other at $t \approx 1000$–1200 Myr (the time the amplitude of the main axisymmetric bending reaches its maximum). As we see, the two times of change in σ_z are closely related to the characteristic growth stages of bending instability. Such a relationship exists in all of the models without bars in which bending instability developed. Thus, we can conclude that in this model, the bending instability is responsible for the increase in σ_z; when the bell ($m = 0$) mode appears, the energy of the random stellar velocity in the disk plane is converted most effectively into the energy of random vertical motions.

Note that the integrated quantities σ_z and σ_R calculated for the entire galaxy were used to construct the plots in Fig. 3. These quantities allow us to judge only the general run of the processes in the disk. Figure 4 shows the radial profiles of the azimuthally averaged σ_z for various times. We see that the relaxation effect is most pronounced for central regions.

In Fig. 5, the σ_z/σ_R ratio is plotted against R for several times (here, we also averaged σ_z/σ_R in concentric rings). We can conclude from our data that the saturation level of the bending instability in a region of about two exponential disk scale lengths in size (about 7–7.5 kpc) is much higher than its level predicted by the linear criterion (3). For these regions, $\sigma_z/\sigma_R \approx 0.4$–$0.8$.

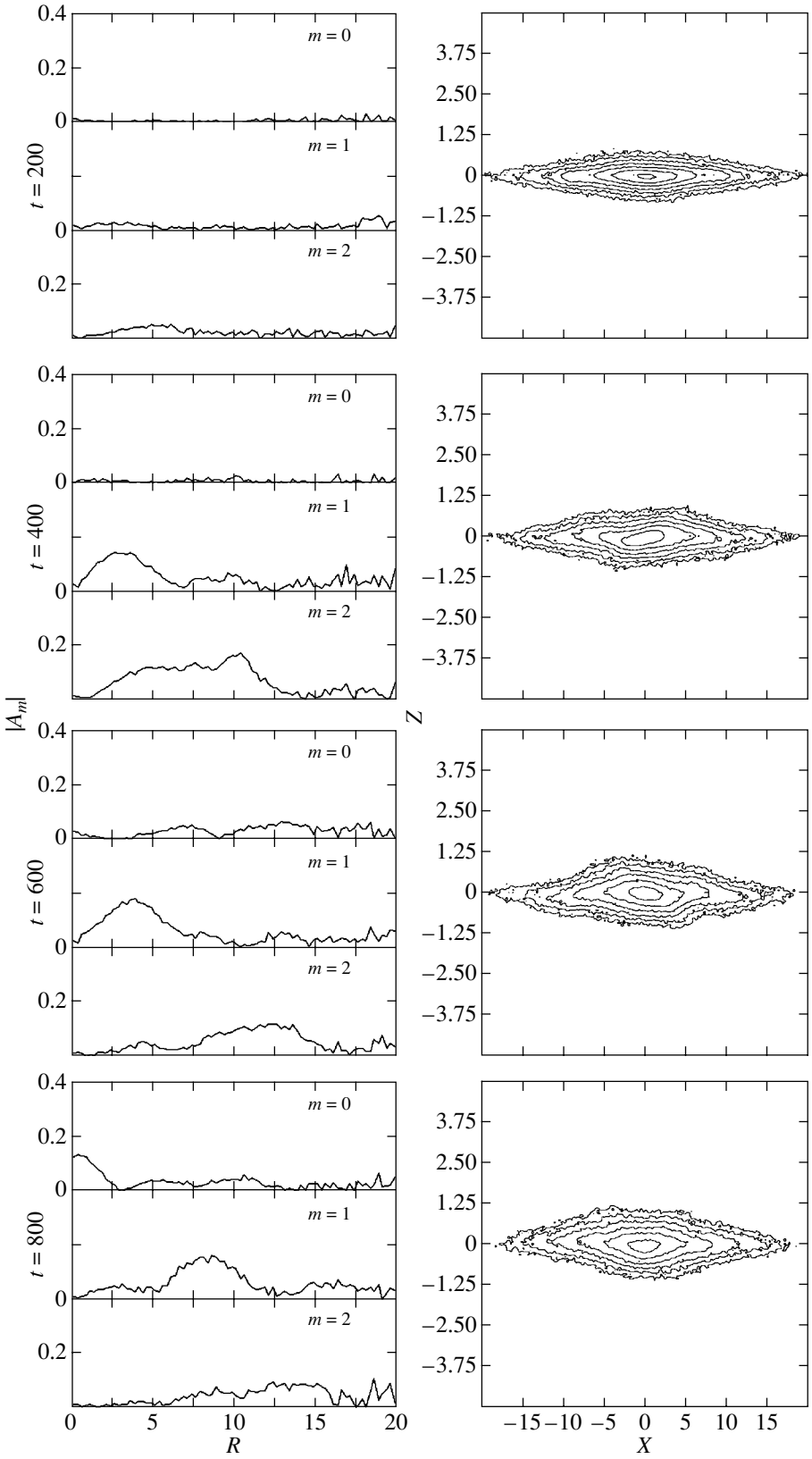

Fig. 1. Model 26_1. Early evolutionary stages of the bending. The left frames: the radial distribution of the amplitude of the first three harmonics ($m = 0, 1, 2$) for the bending perturbation for several times. The right frames: an edge-on view of the galaxy—the isophotal distribution. The horizontal and vertical frame sizes are 40 and 10 kpc, respectively; i.e., the vertical scale was increased by a factor of 4!

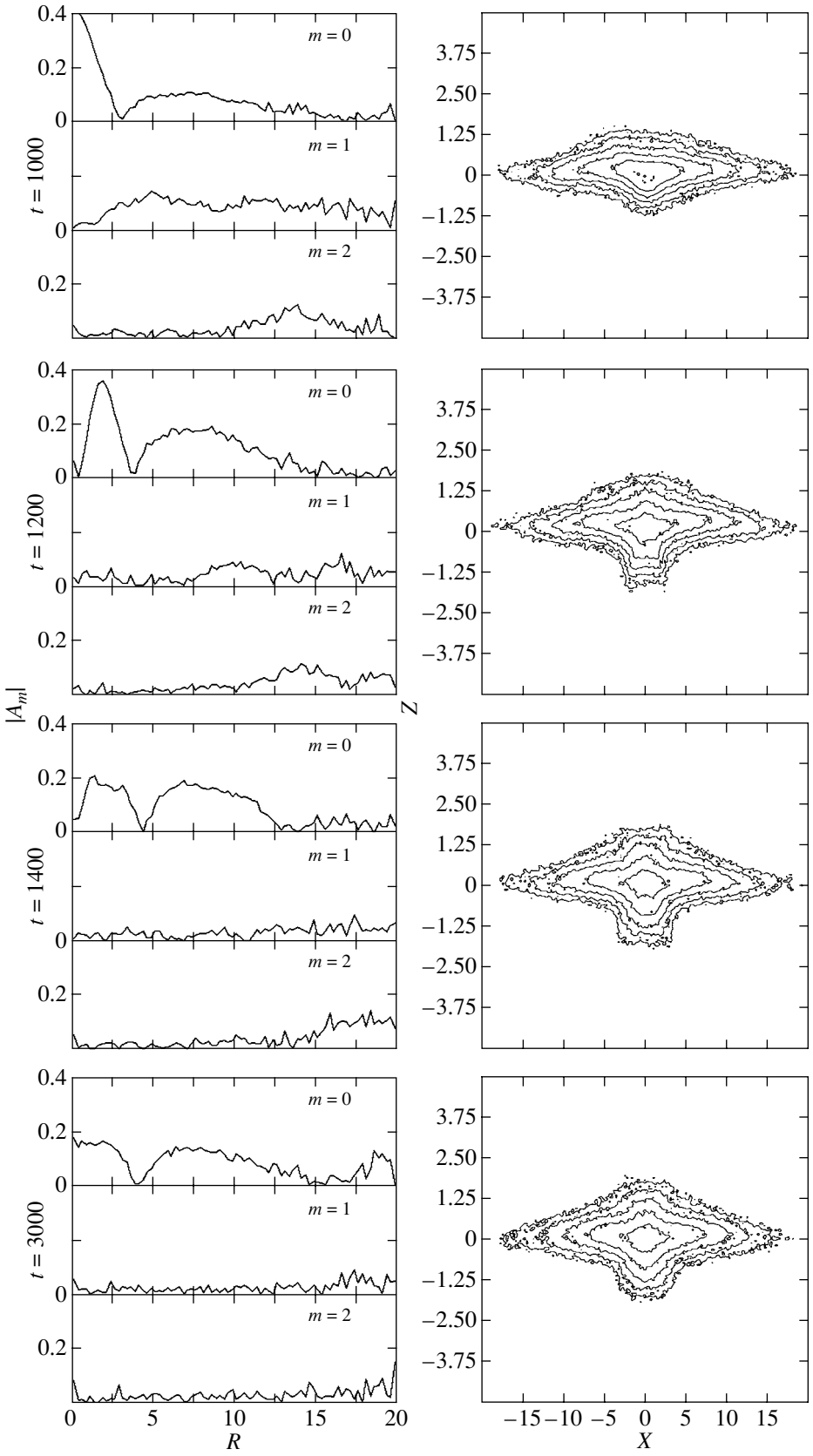

Fig. 2. Model 26_1. The same as Fig. 1 for late evolutionary stages.

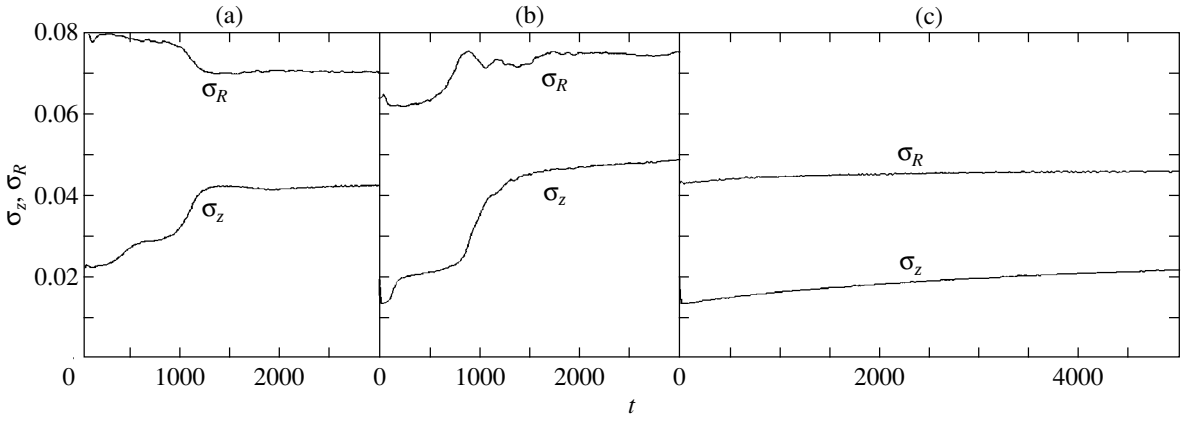

Fig. 3. σ_R (upper curve) and σ_z (lower curve) versus time. The integrated quantities referred to the entire galaxy are plotted: (a) Model 26_1; (b) Model 8_1; and (c) Model 9_1.

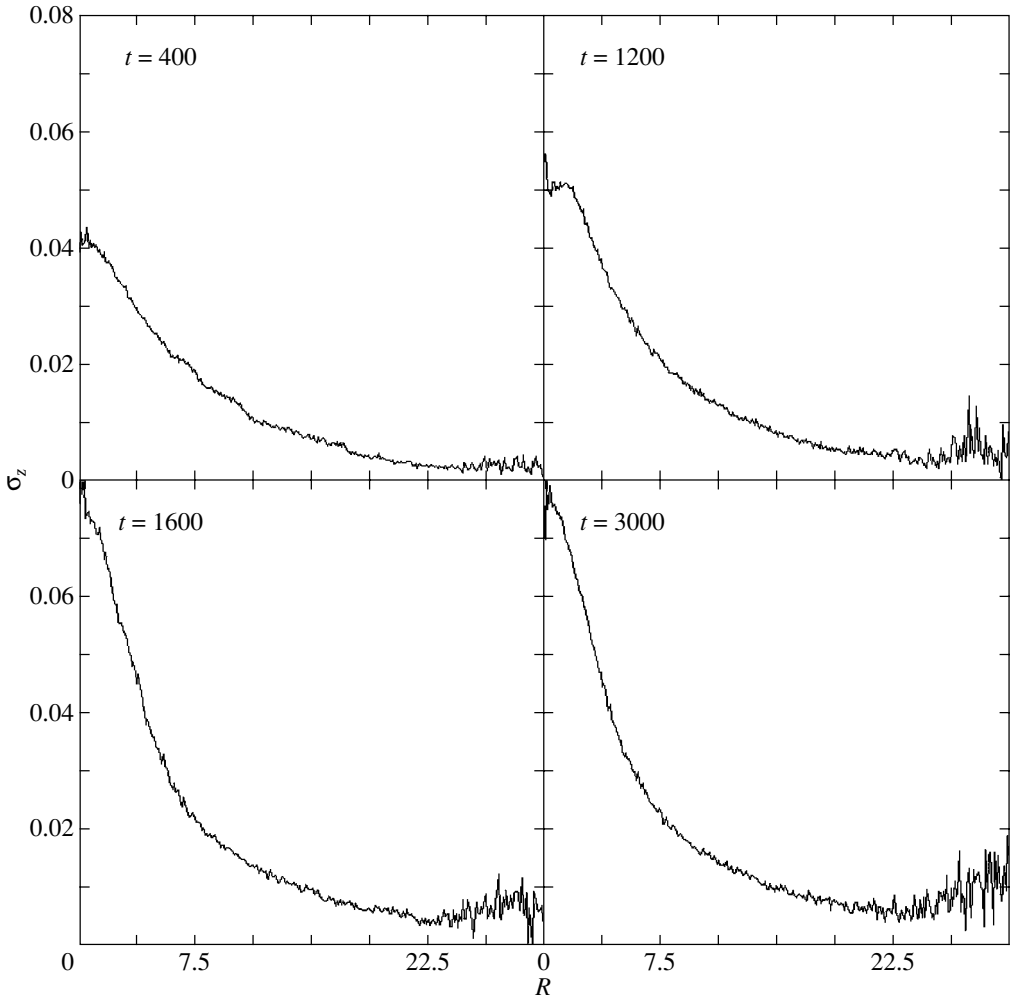

Fig. 4. Model 26_1. σ_z versus R for several times.

In Figs. 1 and 2 (right panels), the edge-on image of a model galaxy is represented by isophotes for several times. The image was vertically magnified by a factor of 4. As a result, the disk bending is clearly seen. Note that the galactic evolution at late stages gives rise to a family of X-shaped orbits in

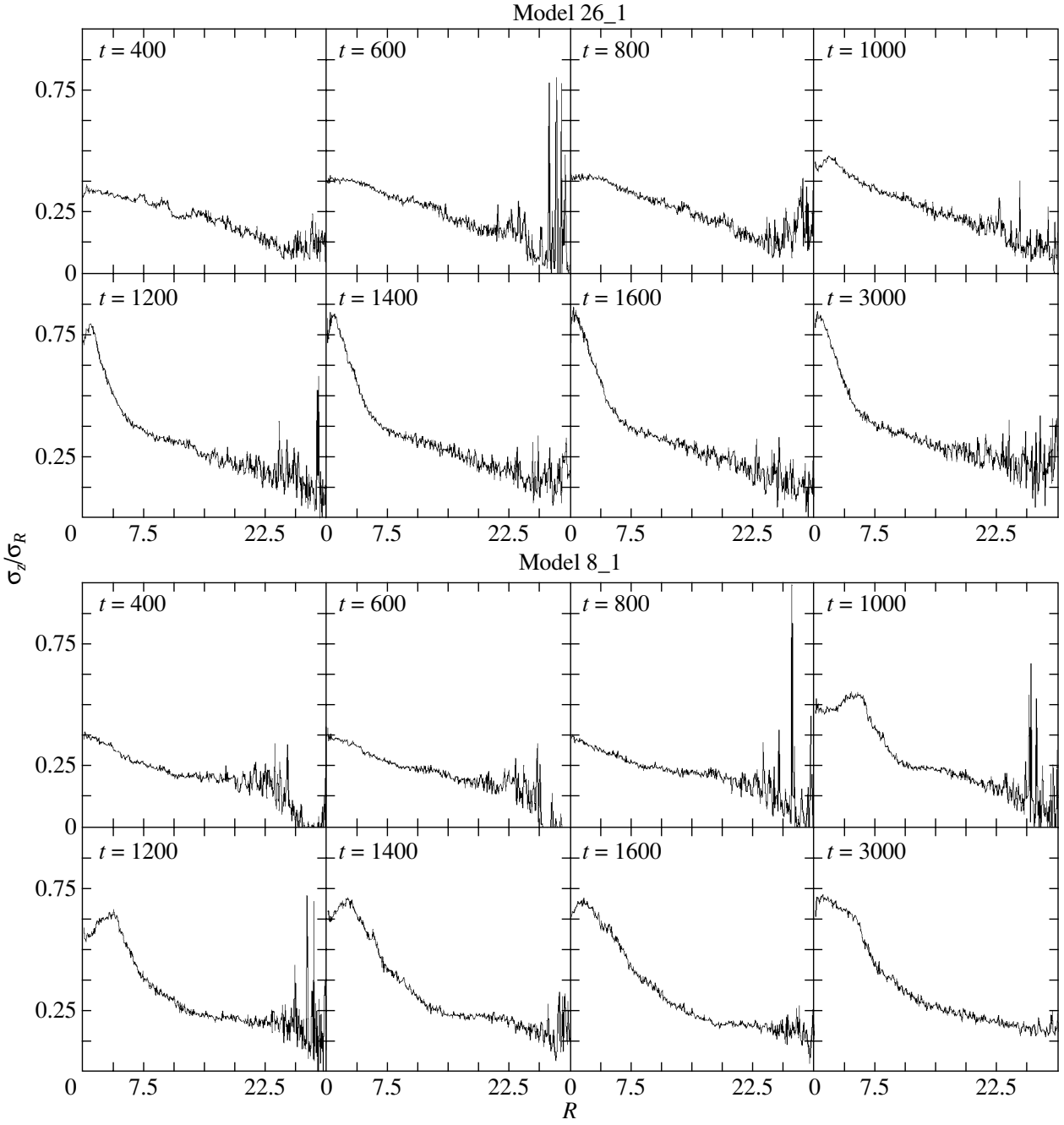

Fig. 5. σ_z/σ_R versus R for several times: Models 26_1 and 8_1.

central regions of the disk ($t = 1200, 1400, 3000$; the left frames; the X-shaped structures are more clearly seen on the pseudoimage of the model galaxy, ttp://www.astro.spbu.ru/staff/seger/articles/warps_2002/fig1_web.html). The main axisymmetric bending may be saturated at a galaxy thickness at which a resonance arises between the frequencies of the stellar oscillations across the disk and in the rotation plane. This resonance can produce X-shaped orbits, which have repeatedly been observed in numerical simulations (Combes *et al.* 1990; Pfenninger and Friedli 1991; Patsis *et al.* 2002).

In other models, the initial and main bends manifested themselves differently that those in Model 26_1. The behavior of all models can be assigned to one of the following cases.

(1) Both the initial and main bends arose almost simultaneously. In the long run, only the axisymmetric bending survived. Abrupt disk heating took place at the time the bending amplitude was increasing.

This scenario was observed for initially thin galaxies, i.e., for the models that started from initial conditions far from the linear saturation level. Almost all of the models with $Q_{8.5} = 2.0$ and $z_0 < 0.3$ kpc show such a pattern of evolution.

(2) The occurrences of the initial and main bends were well separated in time, as for Model 26_1 described in detail.

(3) There was no initial bending at all, while the main bending could be observed at very late evolutionary stages. This scenario is characteristic of initially thick disks, i.e., of the models that started from conditions close to the instability saturation limit. This result closely corresponds to the following theoretical result: at a given ratio of the masses of the spherical and disk components, the mode with the azimuthal number $m = 1$ becomes stable earlier than the other modes as the disk thickness increases (Fridman and Polyachenko 1984). As the disk thickness increases further, the $m = 2$ mode is ultimately saturated and the $m = 0$ mode remains at the fore. Note that the results of our numerical simulations and the theoretical calculations of Fridman and Polyachenko (1984) are inconsistent with the conclusions of Merrit and Sellwood (1994). These authors argue that the $m = 0$ mode is primarily stabilized in thick (radially hot) disks and the $m = 1$ mode must remain at the fore. In our numerical simulations, as the disk thickened, the growth rate of the $m = 0$ mode decreased sharply. A low-amplitude $m = 1$ mode was initially observed against the background of a slowly growing $m = 0$ mode; after the $m = 1$ mode displaced to the periphery, an axisymmetric bending clearly showed up. The vertical velocity dispersion in thick models began to increase only after the axisymmetric bending developed. Thus, for example, the disk bending in Model 32 was observed only 3000 Myr after the beginning of the evolution.

(4) In some of the models in which a bar was formed, only a small increase in the vertical velocity dispersion was associated with the initial bending of the entire disk. This applies to all of the models with $Q_{8.5} = 1.5$ and $z_0 < 0.3$ kpc. For thicker galaxies, no initial bending of the entire disk whatsoever was observed. In all of the models with $Q_{8.5} = 1.5$, the bending instability of the bar itself, which is investigated in the next subsection, was the leading heating mechanism.

The bending instability of the bars. The second vertical disk heating mechanism revealed by our numerical simulations is related to the bending instability of the bars. A bar bending was first detected by Raha *et al.* (1991) in three-dimensional numerical simulations. Its appearance was explained by the development of fire-hose instability in the bar. In our simulations, this instability was responsible for the secular disk heating almost in all of the models with bars.[5]

Consider the disk evolution scenario using Model 8_1 as an example. The main evolutionary stages of the bending in this initially moderately hot model are shown in the color two-dimensional histograms located at http://www.astro.spbu.ru/staff/seger/articles/warps_2002/fig6_web.html and http: // www.astro.spbu.ru / staff / seger / articles/warps_2002/fig7_web.html. At early stages ($t \approx 200$–400 Myr), the initial bending of the entire disk comes to the fore (the group of frames in the middle column). Gradually, the initial bending perturbation reaches its saturation level, is drifted to the galactic periphery, and decays ($t \approx 600$ Myr). A distinct bar has already been formed in the galaxy by this time (Figs. 6 and 7; the group of left frames; all images were oriented in such a way that the bar major axis was horizontal). At $t \approx 800$ Myr, the bending is already generated in the bar. At $t \approx 1000$ Myr, its amplitude reaches a maximum, after which the bending perturbation rapidly decays ($t \approx 1200$–1600 Myr).

The bar bending effect becomes understandable if we look at the group of right frames in Figs. 6 and 7. The shades of gray in these figures indicate the disk thickness in different disk regions. The thickness was calculated as $\sqrt{\overline{z^2(R,\varphi)} - \overline{z(R,\varphi)}^2}$. We see that the bar was much thinner than the rest of the galaxy, which can be explained as follows. Since most of the disk stars were captured into the bar, it has a high surface density. Self-gravity causes the disk to become thinner in the bar region, which gives rise to a bending.

If we look at the plot of the vertical velocity dispersion against time (Fig. 3b), then we will see the curve rises twice: first at $t \approx 200$ Myr, which is clearly associated with the appearance of the initial bending of the entire disk, and, second, at $t \approx 1000$–1200 Myr, which coincides with the time the amplitude of the bar bending reaches its maximum.

In Fig. 5, σ_z/σ_R is plotted against R for several times. We see that for relatively cold disks (as in the case of hot disks; Fig. 5, Model 26_1), the general saturation level of the bending instability is higher than the linear level (3). Merrit and Sellwood (1994) pointed out that moderately hot models ($Q \sim 1$) behave virtually as predicted by the linear theory. Large

[5] In some of the models that started from $Q_{8.5} = 2.0$, despite the large velocity dispersion in the disk plane, a distinct bar was formed at late stages. However, by this time, the vertical velocity dispersion was so large (because of the relaxation associated with the bending instability of the entire disk) that no bending was formed in the bar.

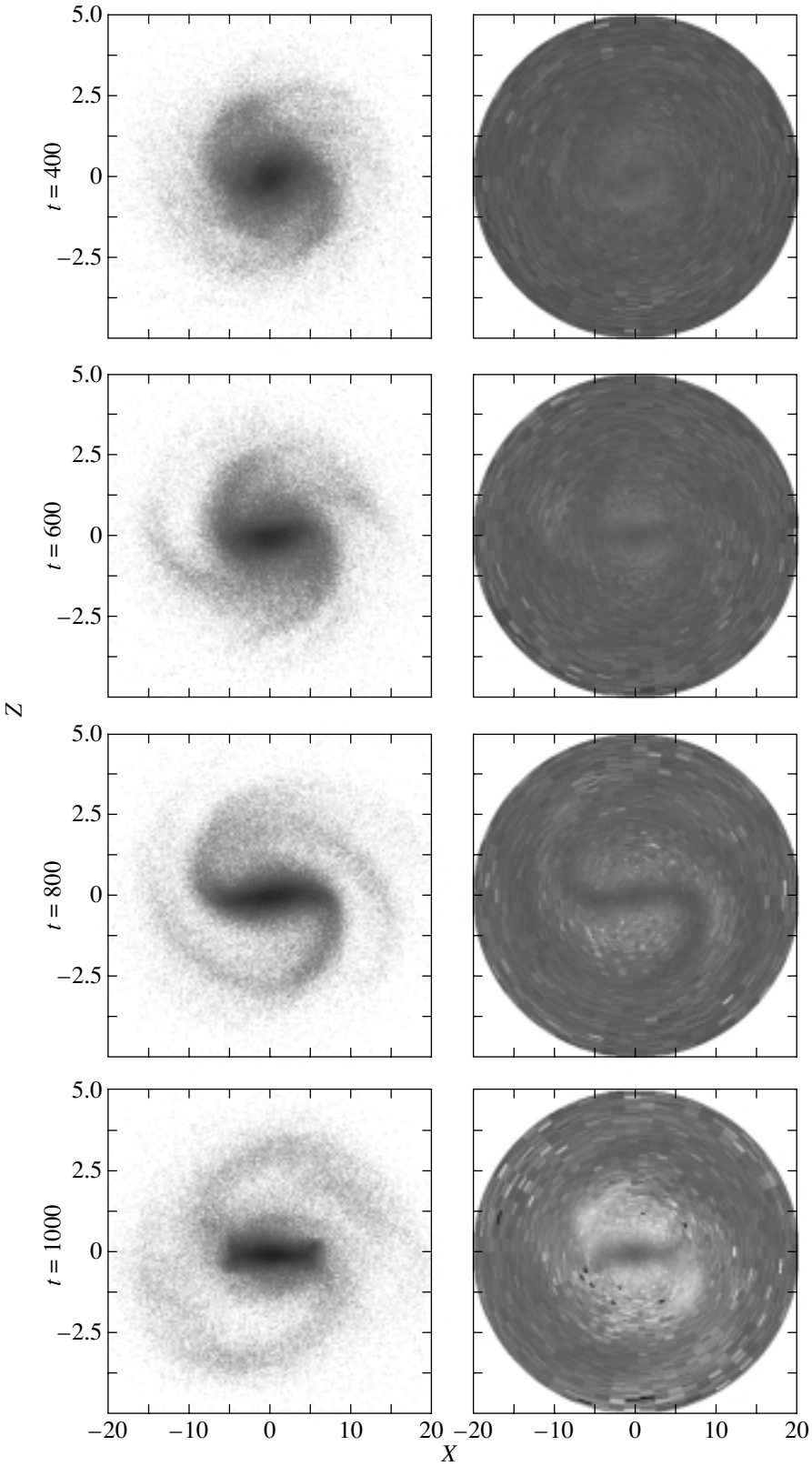

Fig. 6. Model 8_1. The evolution of a disk with $Q_{8.5} = 1.5$ (early stages). In each row: the first frame shows the galaxy seen face-on (the image brightness corresponds to the logarithm of the number of particles per pixel); the second frame shows the two-dimensional galaxy thickness distribution (the thickness is indicated by the shades of gray: the lighter is the disk region, the thicker it is; the thickness ranges from 0 to 1 kpc; the filled circle means that the thickness in this region is outside the range). All pictures are oriented in such a way that the bar was located along the X axis. The frame size is 40×40 kpc.

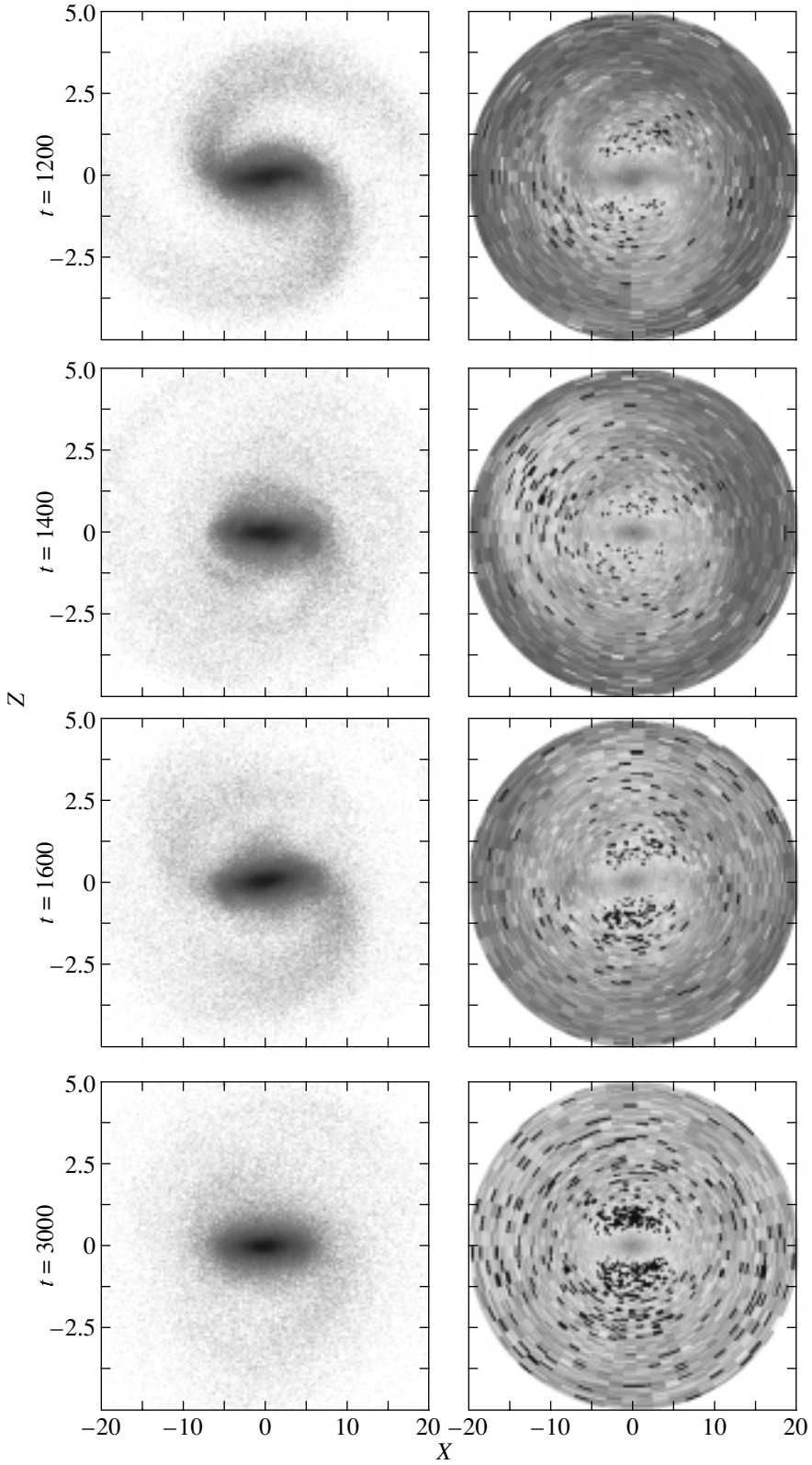

Fig. 7. Model 8_1. The same as Fig. 6 for late evolutionary stages.

deviations take place only for hot models. In our simulations, we observed a similar picture. The saturation level of the bending instability associated with the entire disk in the models with $Q_{8.5} = 1.5$ is close to the linear level (see Fig. 5, $t = 800$, Model 8_1). However, when the bending instability of the forming

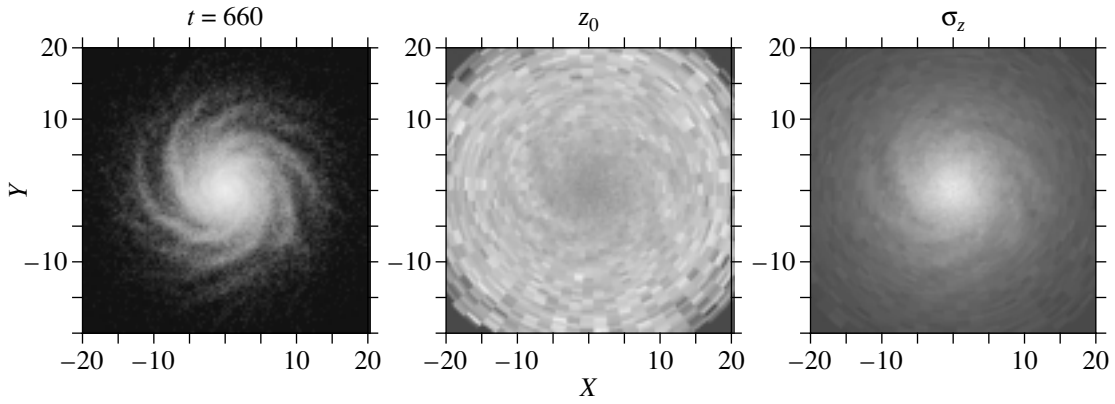

Fig. 8. Model 9_1. A snapshot of the galaxy at $t = 660$ and the two-dimensional disk thickness and σ_z distributions. The size of each frame is 40×40 kpc. The left frame shows the galaxy seen face-on (the image brightness corresponds to the logarithm of the number of particles per pixel). The middle frame shows the two-dimensional disk thickness distribution constructed by using the shades of gray (the brighter the disk region, the larger its thickness at a given location). The right frame shows the two-dimensional σ_z distribution over the galaxy; σ_z is indicates by the shades of gray (the velocity dispersion is larger in brighter regions). We see that in the region of the spiral arms, the galaxy is thinner but the vertical velocity dispersion is larger. This effect is most pronounced for the two arms located in the lower right corner.

bar came into effect, the final vertical disk heating was almost the same as that for the models with $Q_{8.5} = 2.0$ (see Fig. 5, $t = 3000$, Models 26_1 and 8_1).

For the remaining models with $Q_{8.5} = 1.5$ and a low dark-halo mass ($M_\mathrm{h}(4h)/M_\mathrm{d}(4h) < 1$), we observed the same growth stages of bending perturbations as those in Model 8_1. If a bar was formed in the disk, then bending instability sooner or later began to develop in it. The bending amplitude rapidly increased and the instability was ultimately saturated (all of these processes took place on time scales of the order of one billion years). Note that even the bending shape was in each case similar to that observed in Model 8_1. The models differed only by the bar formation time and by the duration of the stage that preceded the onset of bending formation in the bar itself. The larger the dark-halo mass, the later the bar formed and the farther the time of bending generation in the bar from this time. The larger the initial disk thickness, the later the bar formed.

Stellar relaxation in models with a massive halo. Consider the stellar relaxation for models with a massive halo. A massive spherical component is known to effectively suppress the growth of bar-like instability (Ostriker and Peebles 1973) and to have a stabilizing effect on the growth of bending perturbations (Zasov *et al.* 1991; Sellwood 1996). The stellar relaxation in such models (if it takes place) must be produced by some other factors. Let us trace the evolution of the vertical structure of a stellar disk embedded in a massive halo using Model 9_1 as an example.

Because of the presence of a massive spheroidal component in the galaxy, the bending instability of its disk was suppressed. No bar was formed either (at least on a time scale of 5 Gyr). Since a massive halo primarily stabilizes the disk against the growth of perturbations in the disk plane with azimuthal numbers $m \leq 2$, higher-order modes come to the fore. They manifest themselves in the form of multiple short-lived spiral waves and persist in the disk for several disk rotations (see, e.g., the left frame in Fig. 8 and in the figure at http://www.astro.spbu.ru/staff/seger/articles/warps_2002/fig8_web.html). Their amplitude is initially large but the spiral pattern is blurred almost completely by the time $t = 3000$ Myr.

Transient spirals are produced by collective processes and they are responsible for the heating of the disk in its plane. This relationship was first pointed out by Sellwood and Carlberg (1984). In Fig. 3c, the radial (σ_R) and vertical (σ_z) velocity dispersions are plotted against time. As would be expected, the rate of increase in the radial velocity dispersion slowly decreases with decreasing amplitude of the spiral arms and, after $t = 1500$ Myr, the stellar relaxation in the disk plane related to transient spiral perturbations becomes ineffective. At the same time, for all five billion years of evolution, σ_z slowly increases, although the rate of increase gradually decreases. The observed vertical secular disk heating is not the result of numerical pair relaxation, because the levels and the patterns of increase of σ_z and σ_R differ greatly (σ_R is almost constant at late evolutionary stages). The cause of the increase of σ_z in our simulations is completely different.

Let us analyze the vertical disk structure in more detail. Figure 8 shows three frames for one of the times: the galaxy seen face-on, the two-dimensional

disk thickness map, and the two-dimensional vertical velocity dispersion map. We clearly see from these frames that the disk thickness in the regions where the spiral arms are located is smaller than the disk thickness in the interarm space. In other words, inhomogeneities in the distribution of stars in the plane produce inhomogeneities in the vertical distribution of stars. The effect is similar in nature to the bar thinning described in the preceding section: a self-gravitating disk is thinner where the surface density is higher.

We assume that the observed increase of the vertical velocity dispersion is related to the scattering of stars by inhomogeneities in the distribution of matter in the z direction. Apart from the above explanation, there are two more additional facts that are indicative of this.

If we look at the two-dimensional σ_z distribution (Fig. 8), then we can see that σ_z in the spiral arms is higher than that in the interarm space. In addition, it follows from our computations that the decrease in the rate of increase of σ_z correlates well with the decrease in the intensity of transient spirals.

Thus, we believe that the slow increase of the vertical velocity dispersion in our described models is attributable to the scattering of stars by transient spiral perturbations. The latter produce inhomogeneities in the vertical distribution of matter due to self-gravity.

Vertical secular disk heating mechanisms. During our numerical stellar-dynamics simulations, we scanned the space of the control parameters (the initial disk half-thickness, the degree of disk heating in the disk plane, and the relative mass of the spheroidal subsystem). A detailed analysis of our numerical results revealed three distinct mechanisms of secular disk heating in the z direction.

(1) The large-scale bending instability of the entire disk.

(2) The bending instability of bars.

(3) The heating due to inhomogeneities in the vertical distribution of stars produced by matter inhomogeneities in the plane.

The action of a particular heating mechanism depends on the control parameters. If the bar mode is suppressed in the galaxy, then the heating is attributable to the large-scale bending instability associated with the entire disk. This is the case of a hot disk ($Q_{8.5} > 1.5$) and/or a moderately massive halo. In this case, the heating of the central regions is particularly strong. The saturation level of the bending instability in these regions is almost a factor of 2.5 higher than the level that follows from the linear theory. The bending mode with the azimuthal number $m = 0$ plays a key role in the secular heating. The time of its occurrence depends on the initial disk thickness: the thicker the disk, the farther in time the secondary rise in disk temperature related to the growth of the bell mode.

If a bar mode develops in the disk, then the bending instability of the bar gives the largest contribution to the heating. Until a bar is formed, the maximum value of σ_z/σ_R is 0.37 in the central regions and 0.3 on the periphery. This is the level that the bending instability associated with the entire disk reaches. It is in good agreement with the linear criterion. After the formation of a bar, at the time of its bending in the central regions, σ_z/σ_R rises to 0.7–0.8. The heating on vertical bar bending perturbations dominates in initially moderately hot disks ($Q_{8.5} = 1.5$) with a low-mass halo.

The heating on vertical inhomogeneities take place when the bending modes and the bar mode were suppressed. This was observed for moderately hot models ($Q_{8.5} = 1.5$) with a massive halo. Note that the secular disk heating in all directions in similar simulations has been observed more than once. However, we are probably the first to associate the increase of σ_z with the scattering of stars by vertical inhomogeneities.

CONCLUSIONS

We have numerically analyzed the nonlinear growth stages of bending instability in stellar disks with exponential radial density profiles and found significant deviations from the linear theory.

(1) All of the observed modes are global; i.e., the scale of unstable perturbations is larger than the typical scale of density variations in the disk. Our conclusion agrees with the conclusions of Sellwood (1996). It implies that, although the dispersion relation (1) derived for a homogeneous layer is also locally valid for inhomogeneous disks (in particular, exponential disks, as in our numerical simulations), it would be inappropriate to use this relation to analyze the saturation level of long-wavelength perturbations. This also suggests that bending instability will develop in inhomogeneous disks differently in different parts of the galaxy.

(2) The value of $(\sigma_z/\sigma_R)_{\rm cr} \approx 0.3$ was obtained from a linear analysis. As our numerical computations show, the saturation level of large-scale bending perturbations is a factor of 2 or 3 higher than the linear level. The differences are best seen in central regions of the stellar disk. The lower the dark-halo mass, the higher the instability saturation level and the larger the ratio of the vertical and radial velocity dispersions averaged within two exponential disk scale lengths. A similar dependence was pointed out by Mikhailova *et al.* (2001), although without discussing the underlying mechanisms. Early-type spiral galaxies have, on average, a smaller dark-to-luminous mass ratio and,

as follows from the observational data given above, a larger value of (σ_z/σ_R), in agreement with our computations.

(3) The instability saturation time scales are several billion years.

(4) Our numerical simulations revealed three distinct mechanisms of the secular heating of stellar disks in the z direction. We confirmed the existence of bar bending instability that was first detected by Raha *et al.* (1991). For a large series of models, we showed that the bar bending is an inevitable stage of its evolution.

Thus, we can conclude that bending instability can play an important role in the secular disk heating in the z direction.

ACKNOWLEDGMENTS

This work was supported in part by the Program "Leading Scientific Schools" (project no. 00-15-96607), the Federal Research and Technology Program "Astronomy" (project no. 40.022.1.1.1101), and the UR grant no. 02.01.006.

REFERENCES

1. S. Araki, Ph. D. Thesis, Massachus. Inst. Tech. (1985).
2. J. Barnes and P. Hut, Nature **324**, 446 (1986).
3. J. Binney and C. Lacey, Mon. Not. R. Astron. Soc. **230**, 597 (1988).
4. J. Binney and S. Tremaine, *Galactic Dynamics* (Princeton University, 1987).
5. J. Binney, W. Dehnen, and G. Bertelli, Mon. Not. R. Astron. Soc. **318**, 658 (2000).
6. F. Combes, F. Debbasch, D. Friedli, and D. Pfenninger, Astron. Astrophys. **233**, 82 (1990).
7. W. Dehnen and J. J. Binney, Mon. Not. R. Astron. Soc. **298**, 387 (1998).
8. A. M Fridman and V. L. Polyachenko, *Physics of Gravitating Systems* (Springer-Verlag, New York, 1984).
9. B. Fuchs, C. Dettbarn, H. Jahreis, and R. Wielen, Astron. Soc. Pac. Conf. Ser. **228**, 235 (2000).
10. J. Gerssen, K. Kuijken, and M. Merrifield, Mon. Not. R. Astron. Soc. **288**, 618 (1997).
11. J. Gerssen, K. Kuijken, and M. Merrifield, Mon. Not. R. Astron. Soc. **317**, 545 (2000).
12. L. Hernquist, Astrophys. J., Suppl. Ser. **64**, 715 (1987).
13. L. Hernquist, Astrophys. J., Suppl. Ser. **86**, 389 (1993).
14. C. Hunter and A. Toomre, Astrophys. J. **155**, 747 (1969).
15. A. Jenkins, Mon. Not. R. Astron. Soc. **257**, 620 (1992).
16. A. Jenkins and J. Binney, Mon. Not. R. Astron. Soc. **245**, 305 (1990).
17. R. M. Kulsrud, J. W.-K. Mark, and A. Caruso, Astrophys. Space Sci. **14**, 52 (1971).
18. C. G. Lacey, Mon. Not. R. Astron. Soc. **208**, 687 (1984).
19. M. Merrifield, J. Gerssen, and K. Kuijken, Astron. Soc. Pac. Conf. Ser. **230**, 221 (2001).
20. D. Merrit and J. A. Sellwood, Astrophys. J. **425**, 551 (1994).
21. E. A. Mikhailova, A. V. Khoperskov, and S. S. Sharpak, in *Stellar Dynamics—from Clasic to Modern,* Ed. by L. P. Ossipkov and I. I. Nikiforov (St.-Peterburg Gos. Univ., St. Petersburg, 2001), p. 147.
22. J. P. Ostriker and P. J. E. Peebles, Astrophys. J. **186**, 467 (1973).
23. P. P. Parenago, Astron. Zh. **27**, 150 (1950).
24. P. A. Patsis, E. Athanassoula, P. Grosbol, and Ch. Skokos, Mon. Not. R. Astron. Soc. **335**, 1049 (2002).
25. D. Pfenninger and D. Friedli, Astron. Astrophys. **252**, 75 (1991).
26. V. L. Polyachenko and I. G. Shukhman, Pis'ma Astron. Zh. **3**, 254 (1977) [Sov. Astron. Lett. **3**, 134 (1977)].
27. N. Raha, J. A. Sellwood, R. A. James, and F. D. Kahn, Nature **352**, 411 (1991).
28. V. Reshetnikov and F. Combes, Astron. Astrophys. **324**, 80 (1997).
29. W. C. Saslaw, *Gravitational Physics of Stellar and Galactic Systems* (Cambridge Univ. Press, Cambridge, 1985; Mir, Moscow, 1989).
30. J. A. Sellwood, Astrophys. J. **473**, 733 (1996).
31. J. A. Sellwood and R. G. Carlberg, Astrophys. J. **282**, 61 (1984).
32. J. A. Sellwood and D. Merritt, Astrophys. J. **425**, 530 (1994).
33. L. Spitzer and M. Schwarzshild, Astrophys. J. **114**, 385 (1951).
34. L. Spitzer and M. Schwarzshild, Astrophys. J. **118**, 106 (1953).
35. P. J. Teuben, Astron. Soc. Pac. Conf. Ser. **77**, 398 (1995).
36. A. Toomre, Astrophys. J. **139**, 1217 (1964).
37. A. Toomre, Geophys. Fluid Dyn. **66-46**, 111 (1966).
38. H. Velázquez and S. D. M. White, Mon. Not. R. Astron. Soc. **304**, 254 (1999).
39. I. W. Walker, J. Ch. Mihos, and L. Hernquist, Astrophys. J. **460**, 121 (1996).
40. A. V. Zasov, D. I. Makarov, and E. A. Mikhailova, Pis'ma Astron. Zh. **17**, 884 (1991) [Sov. Astron. Lett. **17**, 374 (1991)].

Translated by V. Astakhov

Astronomy Letters, Vol. 29, No. 5, 2003, pp. 336–343. Translated from Pis'ma v Astronomicheskiĭ Zhurnal, Vol. 29, No. 5, 2003, pp. 384–392.

A Study of the B[e] Star AS 160

A. S. Miroshnichenko[1,2*], V. G. Klochkova[3], and K. S. Bjorkman[4]

[1] *Pulkovo Astronomical Observatory, Russian Academy of Sciences, Pulkovskoe sh. 65, St. Petersburg, 196140 Russia*

[2] *Toledo University, Ohio, USA*

[3] *Special Astrophysical Observatory, Russian Academy of Sciences, Nizhnii Arkhyz, Stavropolskii Krai, 357147 Russia*

[4] *University of Toledo, Ohio, USA*

Received October 15, 2002

Abstract—We present the results of our study of the poorly known B[e] star AS 160 = IRAS 07370–2438. The high-resolution spectrum obtained with the 6-m BTA telescope exhibits strong emission in the Hα line with a two-component profile, indicating that the gaseous envelope of the star is nonspherical. Previously nonanalyzed photometric data suggest the presence of a compact dust envelope. The fundamental parameters of the star ($\log L/L_\odot = 4.4 \pm 0.2$, $v \sin i = 200$ km s^{-1}) and its distance (3.5 ± 0.5 kpc) have been determined for the first time and are in agreement with published estimates of the MK spectral type of the object (B1.5 V:). Analysis of the object's properties leads us to suggest that this is a binary system that belongs to our recently identified type of Be stars with warm dust.

Key words: *stars—properties, classification.*

INTRODUCTION

B[e] stars represent a group of B-type stars whose spectra exhibit emission lines (including forbidden ones) along with large near-infrared (1–5 μm) continuum excesses. Sixty-five such objects were first identified by Allen and Swings (1976) in the Milky Way. They noted a correlation between the presence of forbidden lines and the presence of infrared excesses and offered three possible explanations of this phenomenon: the formation of a planetary nebula, the interaction of a hot star with a late-type companion, and direct mass ejection from a massive star. Subsequent studies of B[e] stars indicated that objects at known and well-studied evolutionary stages (young Herbig Ae/Be stars, luminous blue variables (LBVs), symbiotic stars, protoplanetary and planetary nebulae (Miroshnichenko 1998a)) constitute almost half of the initial list. However, until recently about 30 B[e] stars have been studied inadequately and their evolutionary status has been unclear.

We began to investigate individual B[e] stars with an uncertain status in the mid-1980s by using long-term series of multicolor photometric observations (Bergner *et al.* 1995) and low-resolution spectra (Miroshnichenko 1995). These investigations revealed photometric variability in most of the objects studied and no photospheric lines in their spectra. In addition, we found that a large group of B[e] stars with very strong emission-line spectra occupies an unusual position in the IRAS color–color diagram. Such colors ($-0.5 \le \log(F_{25}/F_{12}) \le 0.1$, $-1.1 \le \log(F_{60}/F_{25}) \le -0.3$, where F_{12}, F_{25}, and F_{60} are the fluxes from the object in the IRAS photometric bands at 12, 25, and 60 μm, respectively) are typical of dust envelopes around cool stars or envelopes without dust hotter than ~200 K. Our subsequent studies of stars from this group (which presently contains 19 objects and which we call Be stars with warm dust) have led us to conclude that these are fairly evolved objects most of which are interacting binaries. The latter accounts for the presence of a large amount of circumstellar matter (see Miroshnichenko *et al.* 2002a). Although these objects share common properties, each of them is individual. Therefore, we present the results of our investigation either for individual objects or for small groups of them.

In this paper, which is a continuation of our series of papers including Miroshnichenko *et al.* (2000, 2001, 2002b, 2002c), we present our photometric and spectroscopic observations of the B[e] star AS 160 from the list of Allen and Swings (1976).

*E-mail: anatoly@physics.utoledo.edu

1063-7737/03/2905-0336$24.00

Table 1. The IRTF infrared photometry for AS 160

HJD	K	L	M	N
2451599.92	7.54 ± 0.02	5.84 ± 0.02	5.50 ± 0.05	2.88 ± 0.02

An emission-line spectrum of the star was discovered during a spectroscopic survey of the sky at the Mount Wilson observatory (Merrill and Burwell 1950). UBV and HKL photometry was obtained by Drilling (1991) and Allen (1973), respectively. Infrared radiation from the object was detected by the IRAS and MSX satellites. Based on data published by then, Lamers *et al.* (1998) concluded that the evolutionary status of AS 160 could not yet be determined. Cidale *et al.* (2001) provided spectrophotometry of the star in the wavelength range 3500–4600 Å. They found its spectral type from the Balmer discontinuity to be B1, while its luminosity class (V) was determined unreliably, which does not add information on the nature of the object. The IRAS colors ($\log(F_{25}/F_{12}) = -0.09$, $\log(F_{60}/F_{25}) = -0.71$) allow us to include AS 160 in the group of Be stars with warm dust in their envelopes.

OBSERVATIONS

Infrared $KLMN$ photometry of AS 160 was obtained on February 24–25, 2000, with a germanium–gallium bolometer attached to the 3-m IRTF NASA telescope (Mauna Kea, Hawaiian Islands, USA). The observations were carried out with a 10″ aperture; the background was subtracted at a distance of 15″ in the north–south direction with a frequency of 11 Hz. Four 20-s exposures were taken in each photometric band. The results were reduced to Johnson's broadband photometric system using standard stars from the IRTF list (HR 2574, HR 2943, HR 3314, and HR 3903).

Spectroscopy of the star was obtained on the night of November 30/December 1, 2001, with the LYNX echellè spectrometer (Panchuk *et al.*, 1999) attached to the 6-m BTA telescope in the wavelength range λ5030–6680 Å with a resolution of $\lambda/\Delta\lambda = 25\,000$. Two 53-min exposures were taken sequentially to reliably remove cosmic-ray particle hits. Observations of this star with such a resolution have been obtained for the first time. The mean signal-to-noise ratio in the continuum is close to 50.

RESULTS

Our infrared photometry for the star (see Table 1) confirms the presence of a large infrared excess, which was discovered by Allen (1973) in the early 1970s. The excess is clearly variable, because, while the results match in the L band, our magnitude estimate in the K band is 25% fainter than Allen's estimate, which significantly exceeds the accuracy of the two measurements (~2%). The flux at $\lambda = 12$ μm measured by the IRAS satellite in 1983 exceeds the flux measured by the MSX satellite in 1996 by roughly the same amount (see Fig. 1). On the other hand, our result for the N (10.4 μm) band is in excellent agreement with the IRAS data. Since only two infrared magnitude estimates at different wavelengths are available for the object, we cannot discuss the causes of its variability. We can only say that this picture is typical of other Be stars with warm dust (Miroshnichenko *et al.* 2002b), as is the spectral energy distribution (SED) of AS 160 in general (Fig. 1). In particular, its SED is almost identical to the SED of Hen 3–1398, one of the hottest stars in this group (Miroshnichenko *et al.* 2001). The large infrared excess of AS 160 cannot be explained by the free–free emission from circumstellar gas alone. ISO spectroscopic observations indicate that circumstellar dust is present in the envelopes of such objects (Waters *et al.* 1998). At the same time, the rapid decrease in the observed flux toward longer wavelengths, starting from $\lambda = 10$ μm, suggests that the dust envelope is compact. It may have formed recently.

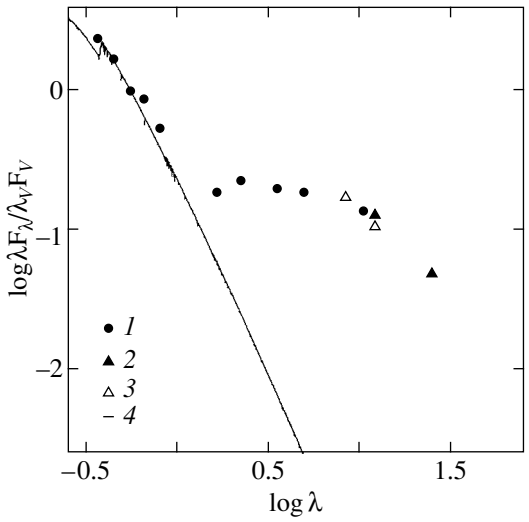

Fig. 1. The spectral energy distribution of AS 160 corrected for reddening: *1*—ground-based photometry; *2*—IRAS data; *3*—MSX data; *4*—theoretical SED for $T_{\rm eff} = 20\,000$ K and $\log g = 4.0$ (Kurucz 1994).

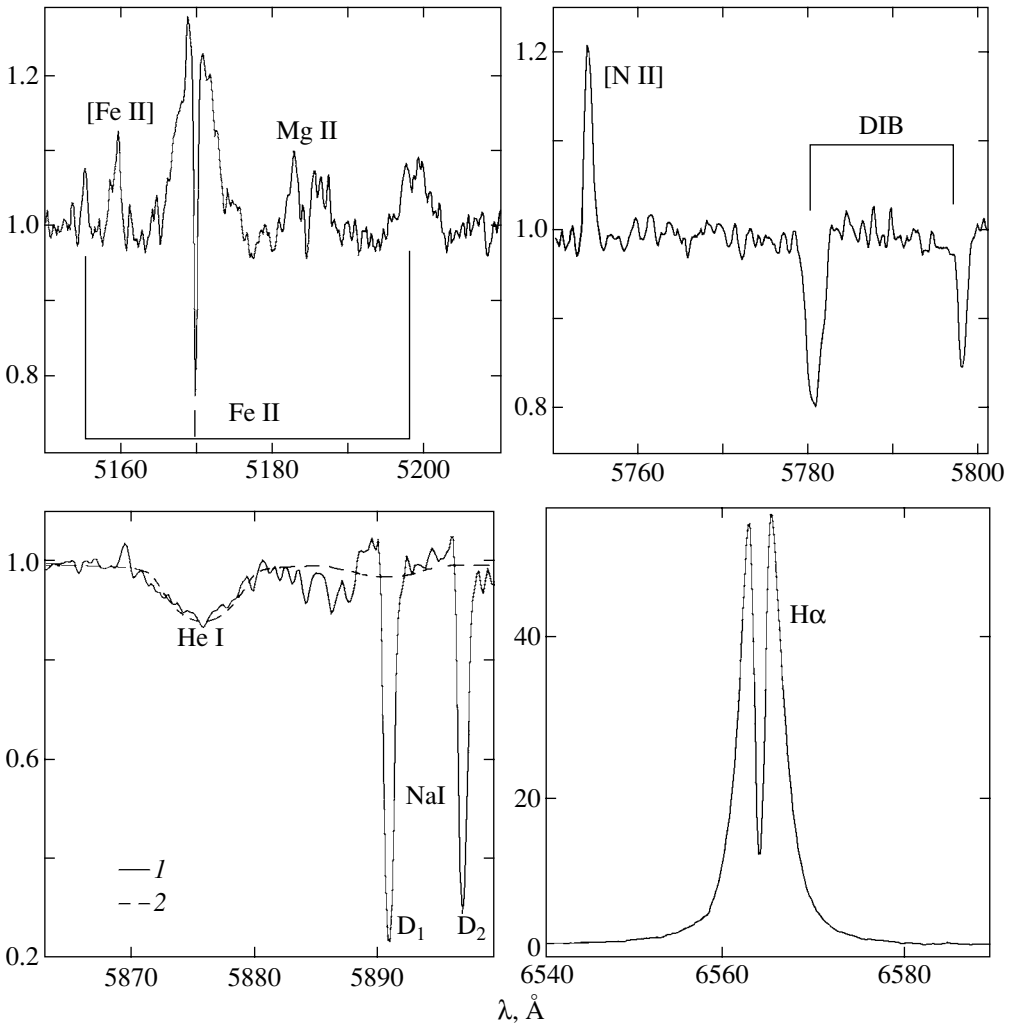

Fig. 2. Portions of the spectrum for AS 160: (*1*) the observed spectrum reduced to the local continuum; and (*2*) the theoretical spectrum computed with the SYNSPEC code (Hubeny *et al.* 1995) for $T_{\rm eff} = 20\,000$ K, $\log g = 4.0$, and $v \sin i = 200$ km s^{-1}. The shallow absorption features in the spectrum with the He I and Na I $D_{1,2}$ lines are telluric.

The lines that we identified in our high-resolution spectrum of AS 160 are listed in Table 2. The spectrum contains mostly permitted and forbidden emission lines of singly ionized iron and diffuse interstellar bands (DIBs). The Balmer spectrum is represented by a strong Hα line. The only detected line of neutral helium, λ5876 Å, has a purely absorption profile. No lines of ionized helium, for example, λ5412 Å, were detected. The state of the helium lines indicates that the spectral type of the object is not earlier than B1, because neutral helium in hotter B[e] stars is usually observed in emission. The observed absorption profile of the λ5876 Å line agrees with its theoretical profile for an effective temperature $T_{\rm eff} = 20\,000$ K, $\log g = 4.0$, and $v \sin i = 200$ km s^{-1} (see Fig. 2). Since there are no other photospheric lines in the observed spectral range, we cannot estimate the fundamental parameters of the star more accurately. However, the result presented above agrees with previously published data (Drilling 1991; Cidale *et al.* 2001).

The optical photometry of AS 160 obtained by Drilling (1991) and its spectrophotometry by Cidale *et al.* (2001) suggest that this is a moderately reddened early-B star. Assuming that the reddening is mainly interstellar (see the discussion below), we can estimate its value from the observed color index $B - V = 0\overset{m}{.}48$ (Drilling 1991) and the normal color $B - V = -0\overset{m}{.}25$ for the corresponding spectral type (Strajzhys 1977), $A_V = 2\overset{m}{.}3$. Approximately the same value, $A_V = 2\overset{m}{.}5 \pm 0\overset{m}{.}3$, can be obtained from the intensities of the DIBs observed in the object's spectrum (Herbig 1993).

The kinematic distance to AS 160 can be estimated from the mean iron-line velocity ($+62.0 \pm$

Table 2. The lines identified in the spectrum of AS 160

Line	λ, Å	I/I_c	RV_{em}, km s^{-1}	RV_{abs}, km s^{-1}	EW, Å
Fe II (35)	5154.50	1.05	67.1	–	0.07
[Fe II] (19F)	5158.81	1.14	60.7	–	0.10
Fe II (42)	5169.03	1.28	63.0	62.9	1.43
Mg I (2)	5183.60	1.10	62.2	68.0	0.29
Fe II (49)	5234.62	1.17	63.5	63.5	0.44
Fe II (48)	5316.78	1.37	52.5	58.3	2.68
[Fe II] (19F)	5333.65	1.09	59.9	–	0.06
[Fe II] (34F)	5746.96	1.07	63.0	–	0.04
[N II] (3F)	5754.80	1.23	52.6	–	0.22
DIB	5780.41	0.80	–	47.7	0.45
DIB	5797.03	0.83	–	50.2	0.17
DIB	5849.80	0.93	–	48.4	0.06
He I (11)	5875.63	0.88	–	6.4	0.75
Na I (1)	5889.95	0.25	–	47.1	0.75
Na I (1)	5889.95	0.18	–	60.9	
Na I (1)	5895.92	0.23	–	47.6	0.66
Na I (1)	5895.92	0.33	–	60.4	
DIB	6195.96	0.90	–	42.8	0.07
DIB	6203.08	0.94	–	37.9	0.10
DIB	6269.73	0.93	–	47.7	0.08
DIB	6283.85	0.82	–	46.2	0.76
[O I] (1F)	6300.30	2.72	61.4	–	1.90
Fe II ( )	6317.99	1.15	59.3	–	0.40
Si II (2)	6347.10	1.12	59.6	–	0.57
[O I] (1F)	6363.78	1.52	60.5	–	0.63
Si II (2)	6371.36	1.08	63.2	–	0.04
DIB	6379.29	0.81		45.8	0.27
H (1)	6562.82	55.70	63.0	53.2	235.30
[N II] (1F)	6583.45	1.23	61.3		0.20
DIB	6613.56	0.79		52.9	0.30

Note. The chemical element (with an indication of the multiplet number) or the interstellar band with which a given spectral feature is identified are listed in column 1; the laboratory wavelengths are listed in column 2; the intensities, in units of the adjacent continuum, are listed in column 3; the heliocentric radial velocities of the emission and absorption line components are listed in columns 4 and 5, respectively (measured by matching the erect and inverted profiles in velocity space); and the equivalent widths are listed in column 6 (measured for the line as a whole).

2.5 km s^{-1}), which is commonly taken as the center-of-mass velocity of the star–envelope system (Humphreys *et al.* 1989), by using the calibration of Dubath *et al.* (1988). The result 3.5 ± 0.2 kpc agrees with the object's position in the Carina arm and gives an estimate of the visual absolute magnitude, $M_V =$

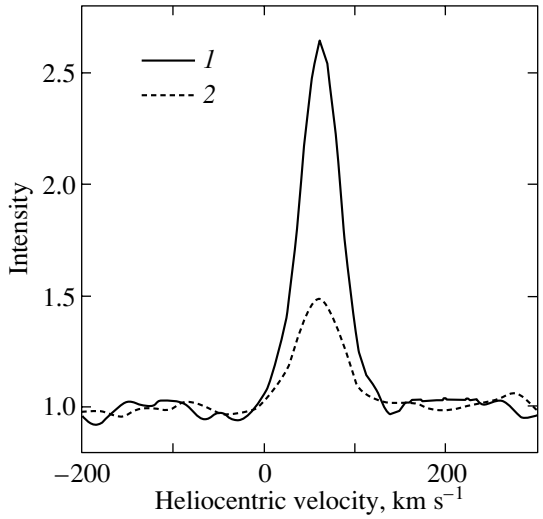

Fig. 3. Profiles of the oxygen forbidden lines in the spectrum of AS 160 at λ6300 Å (*1*) and 6363 Å (*2*). The velocities are given on the heliocentric scale; the intensities were reduced to the local continuum.

$-4\overset{m}{.}1 \pm 0\overset{m}{.}1$, for the observed visual magnitude of the star $V = 10\overset{m}{.}94$ (Drilling 1991) and $A_V = 2\overset{m}{.}3$. The derived luminosity corresponds to the MK spectral type B1.5 III–IV (Strajzhys and Kuriliene 1981), which is in agreement with the remaining data on the star given above. Taking the bolometric correction $BC = -2\overset{m}{.}2$ (Miroshnichenko 1998b), we obtain the luminosity $\log L/L_\odot = 4.4 \pm 0.1$. The interstellar reddening law toward AS 160 determined by Neckel and Klare (1980) indicates a linear and slow increase in A_V to $\sim 1^m$ as the distance from the Sun increases to $\sim$3 kpc followed by its sharp increase at distances of 3–3.5 kpc, which is consistent with our kinematic distance estimate.

The deep sodium lines (λ5889 and 5895 Å) split up into two components with radial velocities of +47 and +61 km s^{-1}. This splitting is almost invisible on the scale of Fig. 2, because the components are close. The position of the blue component coincides with the mean DIB radial velocity, while the position of the red component is close to the mean radial velocity of the emission lines in the spectrum. The blue component probably originates in the Carina spiral arm, suggesting that the object is far from the Sun, while the red component originates in the circumstellar medium. The absence of the component associated with the local spiral arm can be explained by the low density of the interstellar medium, which is confirmed by a small increase in the reddening of stars with distance in this direction up to the Carina arm (Neckel and Klare 1980).

DISCUSSION

We determined the kinematic distance to AS 160 and its error by assuming that the metal-line velocities reflect the object's velocity in its Galactic orbit (in other words, the peculiar velocity is low) and that the Galactic rotation curve toward the object has no significant systematic errors. The above distance dependence of interstellar reddening determined by Neckel and Klare (1980) indicates that these assumptions are valid. It shows that the lower limit of the distance to AS 160 cannot be less than 3 kpc. Otherwise, much of the object's reddening would be circumstellar. Below, we show that this is unlikely. In addition, since the object is close to the Galactic plane ($b = -1\overset{\circ}{.}4$), the reddening will be higher than the observed one when it is farther ($\sim$4 kpc or more). This will give rise to new components in interstellar lines that are unobservable in the object's spectrum. These considerations allow a more realistic distance estimate of 3.5 ± 0.5 kpc to be obtained, which also slightly increases the error in the luminosity estimate, $\log L/L_\odot = 4.4 \pm 0.2$. The equal velocities of the emission and absorption components in metal lines (and forbidden lines), indicating that both the emission and absorption features originate in the envelope, confirm the interpretation of their mean velocity as the velocity of the system. In addition, the kinematic distances estimated for other similar objects observed in different directions under this assumption are generally in good agreement with the distances calculated from their spectroscopic parallaxes (Humphreys *et al.* 1989; Miroshnichenko *et al.* 2000, 2001, 2002b).

The above distance estimate for AS 160 agrees with the interstellar reddening estimate provided that the circumstellar reddening is low. It can be shown that the effect of the object's gas–dust envelope on its optical SED is actually small. The emission-line profiles in the spectrum of AS 160 have either one or two peaks. In the latter case, the peaks are separated by a distinct absorption component. Such profiles are characteristic of nonspherical gaseous envelopes in the shape of highly flattened disks (Hummel and Vrancken 2000). In this case, the symmetry plane of the AS 160 envelope is inclined to the line of sight in such a way that we see it almost edge-on, but the optical depth on the line of sight is small. This orientation is evidenced by the absence of completely absorption Fe II line profiles and by the fact that only one line exhibits an absorption component with the minimum intensity below the continuum level (Fig. 2).

The symmetric emission profiles of the optically thin oxygen forbidden lines (Fig. 3) also indicate that the envelope is highly flattened. Theoretical calculations in terms of the model of an axisymmetric

constant-velocity polar wind (Edwards *et al.* 1987) predict such profiles for winds with strong focusing (the wind cone angle is no more than 30°) and with an inclination of the symmetry axis no less than 60° to the line of sight. We do not see double-peaked profiles of these lines, because the spectral resolution of our observations is insufficient. The presence of strong oxygen forbidden lines and weak nitrogen lines (λ6583 Å) makes it possible to estimate the matter density in the formation region of these lines. At a temperature of 10^4 K typical of this region in B[e] stars (Lamers *et al.* 1998), the maximum density at which the collisional and radiative processes become balanced is $\sim 10^6$ cm^{-3} for the [O I] λ6300 Å line and $\sim 10^5$ cm^{-3} for the [N II] λ6583 Å line (Osterbrock 1989). Thus, the sought-for density must be slightly below 10^5 cm^{-3}.

The absence of an emission or absorption band in the object's spectrum near $\lambda = 10$ μm indicates that the dust envelope is also nonspherical. The flat infrared spectrum in this wavelength range suggests either a large optical depth ($100 \leq \tau \leq 10$), if the envelope consists of silicate grains (Yorke and Shustov 1981), or the presence of predominantly amorphous carbon in the envelope. In the latter case, the optical depth can take on any value, because amorphous carbon has no spectral features near $\lambda 10$ μm. However, this chemical composition of the envelope suggests that the object has strongly evolved off the main sequence (MS) and that the carbon produced by nuclear reactions in the stellar core has already reached the stellar surface. Since the spectrum of AS 160 contains no lines characteristic of such evolved stars, it would be natural to assume that the circumstellar dust has a nearly interstellar composition. The envelope is then most likely optically thick and nonspherical, with a symmetry axis that does not pass through the line of sight. The infrared excess at wavelengths up to 60 μm accounts for about 1% of the stellar luminosity and is a lower limit for the amount of energy reradiated by the circumstellar dust. This estimate is consistent with the assumption that the dust envelope is optically thick only if it is highly flattened.

The velocity of the He I λ5876 Å line (+6 km s^{-1}) differs greatly from the velocities of the remaining lines and may suggest that the stellar velocity is peculiar. In particular, this difference may result from orbital motion in the binary system. We observed a change in the velocity of this line, while the positions of the emission lines were stable, in other members of the group of Be stars with warm dust (e.g., MWC 657; Miroshnichenko *et al.* 2000), together with other evidence of the binary nature. For example, lines of the late-type star are observed along with emission lines of the hot component in such members of the group as MWC 623 (Zickgraf and Stahl 1989), AS 381 (Miroshnichenko *et al.* 2002b), and V669 Cep (Miroshnichenko *et al.* 2002c). No lines that could be attributed to the secondary stellar component of the system were detected in the spectrum of AS 160.

Assuming that the velocity difference between the helium and metal lines ($\Delta V_r = 57$ km s^{-1}) is comparable to the half-amplitude of the radial-velocity curve for the primary component due to orbital motion, we can roughly estimate the parameters of the possible secondary component. It follows from the derived luminosity and temperature of the primary component (25 000 K; Cidale *et al.* 2001) that its radius is ~ 10 $R_\odot$. It thus follows that the minimum orbital period of the binary system is $\sim$10 days. With this orbital period, the primary component fills its Roche lobe and the binary component mass ratio is $\sim$3. In this case, distinct eclipses would be observed at the above orbital inclination. In addition, such close (Algol-type) binary systems do not exhibit strong emission-line spectra, because the intrasystem region is too small to accumulate a large amount of circumstellar matter. The eclipsing binary RY Sct with a period of $\sim$12 days and an infrared excess similar to that observed in AS 160 (Smith *et al.* 2002) serves as an example. Therefore, the orbital period of the binary must be longer (possibly, of the order of several months) and the mass ratio must be closer to unity ($\sim$2 for a period of two months). Systematic spectroscopic observations for one year could significantly refine the estimates obtained.

The large near-infrared ($\lambda 2$–10 μm) excess, together with the sharp decrease in the infrared flux toward longer wavelengths, imposes constraints on the possible evolutionary status of the object. For example, AS 160 cannot be at a pre-MS evolutionary stage, because the infrared SEDs for such objects are much flatter and the hot dust emitting in the near infrared dissipates earlier than the cold dust as they evolve toward the MS (Miroshnichenko *et al.* 1996). AS 160 cannot be at a post-AGB evolutionary stage either; i.e., it cannot be a protoplanetary nebula for the following reasons. First, the dust envelopes in such objects are formed at a previous evolutionary stage and their dust temperature is below $\sim$100 K. Second, the luminosity of AS 160 is close to the upper luminosity limit for planetary nebulae (Blöcker 1995). Such objects are rare, because they traverse the entire path from a red giant to a planetary nebula in several tens of years. We have no evidence of any change in the brightness or temperature of AS 160 in the 50 years elapsed since its discovery. In addition, the rotational velocities for objects at such an advanced

evolutionary stage are low because of the loss of angular momentum.

The luminosity of AS 160 also indicates that this star is not a supergiant, which can intensely lose its mass at a critical evolutionary stage, showing a strong emission-line spectrum (e.g., LBV-type stars). Nor can it be a Wolf–Rayet star, because its spectrum exhibits no characteristic emission lines of CNO-group elements. For a single star that is not far from the MS, a strong mass outflow is not typical at a relatively low rotational velocity (see above). Classical Be stars are the objects that are most similar to AS 160 in observed properties (Harmanec 2000). However, while the latter have a higher mean rotational velocity, their emission-line spectra are weaker than those of AS 160. In addition, more and more data suggesting that many Be stars (particularly those with strong emission-line spectra) are binary systems have recently appeared (Gies 2000).

Thus, in our opinion, the most plausible explanation for the combination of the object's low luminosity and its strong emission-line spectrum can be mass transfer in a high-mass binary system (Van den Heuvel 1994). The more massive components of such binaries do not go far from the main sequence, whereas their secondary components can have a much lower mass (and/or brightness), with their temperature range being wide. Indeed, among binary Be stars with warm dust, the secondary components are generally fainter than the primary components (B type stars) by 2^m–3^m. At the same time, the secondary components are detected in objects whose envelopes are inclined at a large angle to the line of sight. For example, the plane of the MWC 623 envelope is seen nearly face-on, while the narrow and mainly single-component emission-line profiles of AS 381 and V669 Cep suggest a large inclination of their envelope planes to the line of sight. Thus, it will apparently be difficult to detect secondary lines in the spectrum of AS 160 even at a higher spectral resolution and a higher signal-to-noise ratio. However, the amplitude of the radial-velocity variations due to orbital motion for the observed envelope orientation, which usually coincides with the orbital plane, must be larger for AS 160 than that for the binaries mentioned above.

Modeling the observed characteristics of AS 160 is beyond the scope of our study because of uncertainties in the parameters of the binary system in general (characteristics of the possible secondary component) and its envelope in particular (details of the geometry, sizes, etc.). To address this problem requires further observations, including multicolor photometry, spectroscopy with a higher resolution and a higher signal-to-noise ratio, speckle interferometry, and polarimetry.

CONCLUSIONS

Our new high-resolution spectroscopic observations of the B[e] star AS 160 have allowed its luminosity and distance from the Sun to be reliably determined for the first time. These results agree with previous photometric data and spectrophotometric estimates of the MK type of the object. Our infrared photometry of AS 160 and analysis of (IRAS and MSX) satellite data show that its brightness in the wavelength range $\lambda 2$–10 μm varied within no more than 20–25% compared to the 1970s–1980s data. The strong emission-line spectrum of the object, together with its peculiar infrared SED (a rapid decrease in the flux toward longer wavelengths from $\lambda = 10$ μm), allow us to put AS 160 in the group of Be stars with warm dust that has recently been identified and described by Miroshnichenko *et al.* (2002a). This group is among the few groups of early-type stars that show evidence of circumstellar dust in their envelopes. Our working hypothesis about the nature of such objects is that most of their observed properties can be explained by mass transfer in a binary system. However, the secondary components are difficult to detect because of the large magnitude difference between the components (2^m–3^m). A further study of AS 160 primarily requires spectroscopic observations with a time resolution from several weeks to several months, which can impose constraints on the probable orbital period of the binary system. In addition, a comprehensive investigation using various observing techniques will make it possible to refine the parameters of the circumstellar medium.

ACKNOWLEDGMENTS

This work was supported by the Russian Foundation for Basic Research (project no. 02-02-1685) and the U.S. Civilian Research and Development Foundation (CRDF) (grant no. RP1-2264). We wish to thank S.A. Lamzin for a critical analysis of the manuscript and for helpful remarks.

REFERENCES

1. D. A. Allen, Mon. Not. R. Astron. Soc. **161**, 145 (1973).
2. D. A. Allen and J.-P. Swings, Astron. Astrophys. **47**, 293 (1976).
3. Yu. K. Bergner, A. S. Miroshnichenko, R. V. Yudin, *et al.*, Astron. Astrophys., Suppl. Ser. **112**, 221 (1995).
4. T. Blöcker, Astron. Astrophys. **299**, 755 (1995).
5. L. Cidale, J. Zorec, and L. Triganiello, Astron. Astrophys. **368**, 160 (2001).
6. J. D. Drilling, Astrophys. J., Suppl. Ser. **76**, 1033 (1991).

7. P. Dubath, M. Mayor, and G. Burki, Astron. Astrophys. **205**, 77 (1988).
8. S. Edwards, S. Cabrit, S. E. Strom, *et al.*, Astrophys. J. **321**, 473 (1987).
9. D. R. Gies, in *The Be Phenomenon in Early-Type Stars*, Ed. by M. A. Smith, H. F. Henrichs, and J. Fabregat (Astron. Soc. of the Pac., San Francisco, 2000), Vol. 214, p. 668.
10. P. Harmanec, in *The Be Phenomenon in Early-Type Stars*, Ed. by M. A. Smith, H. F. Henrichs, and J. Fabregat (Astron. Soc. of the Pac., San Francisco, 2000), Vol. 214, p. 13.
11. G. H. Herbig, Astrophys. J. **407**, 142 (1993).
12. I. Hubeny, T. Lanz, and C. S. Jeffery, *Synspec—A User Guide* (1995).
13. W. Hummel and M. Vrancken, Astron. Astrophys. **359**, 1075 (2000).
14. R. M. Humphreys, H. J. G. L. M. Lamers, N. Hoekzema, and A. Cassatella, Astron. Astrophys. **218**, L17 (1989).
15. R. L. Kurucz, Smithsonian Astrophys. Observ. CD-ROM No. 19 (1993).
16. H. J. G. L. M. Lamers, F.-J. Zickgraf, D. De Winter, *et al.*, Astron. Astrophys. **340**, 117 (1998).
17. P. W. Merrill and C. G. Burwell, Astrophys. J., Suppl. Ser. **112**, 72 (1950).
18. A. S. Miroshnichenko, Astron. Astrophys. Trans. **6**, 251 (1995).
19. A. S. Miroshnichenko, in *B[e] Stars*, Ed. by A.-M. Hubert and C. Jaschek (Kluwer Acad., Dordrecht, 1998a), p. 145.
20. A. S. Miroshnichenko, in *The Interaction between Observation and Theory*, Ed. by T. R. Bedding (School of Physics, Univ. of Sydney, Sydney, 1998b), p. 50.
21. A. S. Miroshnichenko, Yu. K. Bergner, K. S. Kuratov, *et al.*, Astron. Zh. **73**, 559 (1996) [Astron. Rep. **40**, 509 (1996)].
22. A. S. Miroshnichenko, E. L. Chentsov, V. G. Klochkova, *et al.*, Astron. Astrophys., Suppl. Ser. **147**, 5 (2000).
23. A. S. Miroshnichenko, H. Levato, K. S. Bjorkman, and M. Grosso, Astron. Astrophys. **371**, 600 (2001).
24. A. S. Miroshnichenko, K. S. Bjorkman, E. L. Chentsov, and V. G. Klochkova, in *Exotic Stars as Challenges to Evolution*, Ed. by C. A. Tout and W. Van Hamme (Astron. Soc. of the Pac., San Francisco, 2002a), vol. 279, p. 303.
25. A. S. Miroshnichenko, K. S. Bjorkman, E. L. Chentsov, *et al.*, Astron. Astrophys. **383**, 171 (2002b).
26. A. S. Miroshnichenko, K. S. Bjorkman, E. L. Chentsov, *et al.*, Astron. Astrophys. **388**, 563 (2002c).
27. Th. Neckel and G. Klare, Astron. Astrophys., Suppl. Ser. **42**, 251 (1980).
28. D. E. Osterbrock, *Astrophysics of Gaseous Nebulae and Active Galactic Nuclei* (Univ. Sci. Books, Mill Valey, 1989).
29. V. E. Panchuk, V. G. Klochkova, I. D. Naidenov, *et al., Preprint of Special Astrophysics Observatory, Russian Academy of Sciences, Nizhnii Arkhyz, 1999*, No. 139.
30. N. Smith, R. D. Gehrz, O. Stahl, *et al.*, Astrophys. J. **578**, 464 (2002).
31. V. Strajzhys, *Multicolor Stellar Photometry* (Mokslas, Vilnus, 1977).
32. V. Strajzhys and G. Kuriliene, Astrophys. Space Sci. **80**, 353 (1981).
33. E. P. J. Van den Heuvel, in *Interacting Binaries*, Ed. by H. Nussbaumer and A. Orr (Springer, 1994), p. 263.
34. L. B. F. M. Waters, P. W. Morris, R. H. M. Voors, and H. J. G. L. M. Lamers, in *B[e] Stars* Ed. by A.-M. Hubert and C. Jaschek (Kluwer Acad., Dordrecht, 1998), p. 111.
35. H. W. Yorke and B. M. Shustov, Astron. Astrophys. **98**, 125 (1981).
36. F.-J. Zickgraf and O. Stahl, Astron. Astrophys. **223**, 165 (1989).

Translated by V. Astakhov

Astronomy Letters, Vol. 29, No. 5, 2003, pp. 344–347. From Pis'ma v Astronomicheskiĭ Zhurnal, Vol. 29, No. 5, 2003, pp. 393–396.

Some Integrable Cases of the Two-Body Problem with Mass Depending Both on Time and Distance*

J. A. Docobo**

Observatorio Astronómico Ramón María Aller,
Universidad de Santiago de Compostela, Avenida das Ciencias s/n,
15782 Santiago de Compostela, Spain

Received April 20, 2002; in final form, November 12, 2002

Abstract—An extension of the Gylden–Meshcherskii problem when the mass depends both on time and distance between two bodies is considered. Certain mass loss laws as well as the Meshcherskii position vector and time transformation are used to convert the problem into the cases with equations of motion arising from integrable potentials. © *2003 MAIK "Nauka/Interperiodica"*.

Key words: *celestial mechanics—mass loss.*

INTRODUCTION

An isotropic and intense mass loss when the latter does not affect the system dynamics represents a special case of the two-body problem with a variable mass. Traditionally, it is called the Gylden–Meshcherskii problem formulated by the vectorial equation

$$\ddot{\mathbf{r}} = -\mu(t)\frac{\mathbf{r}}{r^3}. \tag{1}$$

Along with this mathematical problem, the Eddington–Jeans law emerged:

$$\dot{m} = -\alpha m^n; \tag{2}$$

it tried to describe the mass loss caused by stellar radiation. Here, α and n are two positive real numbers, the first being close to zero and the latter being between 0.4 and 4.4.

The well-known exact solutions of the problem represented by Eq. (1) given by Meshcherskii correspond to law (2) when $n = 2, 3$. According to this law, the semimajor axis is the unique orbital element that presents a secular variation.

On the other hand, the statistical data collected on the basis of the orbital elements for visual double stars seem to indicate a trend when, on average, a higher eccentricity corresponds to a higher orbital period. Dommanget (1981, 1982, 1997) suggested that such a trend could be related to the stellar mass loss. Martin (1934) and Chiara (1957) showed that under the assumption of a mass-loss dependence on the distance between two components, a secular increase in eccentricity can be produced, while, on the other hand, no distance dependence implies a merely periodical behavior. For example, applying Martin's law,

$$\dot{m} = -\alpha\frac{m^n}{r^2}, \tag{3}$$

it can be proved (Docobo and Prieto 1998; Docobo *et al.* 1999a), in turn, that the higher the initial eccentricity, the larger its increase.

Nevertheless, when examining new catalogs of visual double stars (Hartkopf and Mason 2001: Docobo *et al.* 2001), this relationship between e and P is not globally observed. However, in the case of certain close binaries, some authors (e.g., Soker 2000) attribute the detected increase in orbital eccentricity to enhanced mass loss due to the gravitational effect at the periastron passage. This increase is occasionally even stronger than the tidal forces, which tend to circularize the orbit.

Apart from that, a number of papers where the relationship between components' position on the orbit and their colliding-wind disturbance become plausible were published (St. Louis 1996; Rauw *et al.* 1996; Moffat 1998).

All these facts forced us (Docobo *et al.* 1999b; Andrade and Docobo 2001a, 2001b) to study problem (1) when an additional dependence of the mass on distance is considered, with the aim of investigating a phenomenon that could be called a "periastron effect" and its possible influence on the secular variation of some orbital elements such as e and ω. In any case, we have shown recently (Docobo and Andrade 2002;

*This article was submitted by the authors in English.

**E-mail: oadoco@usc.es

1063-7737/03/2905-0344$24.00

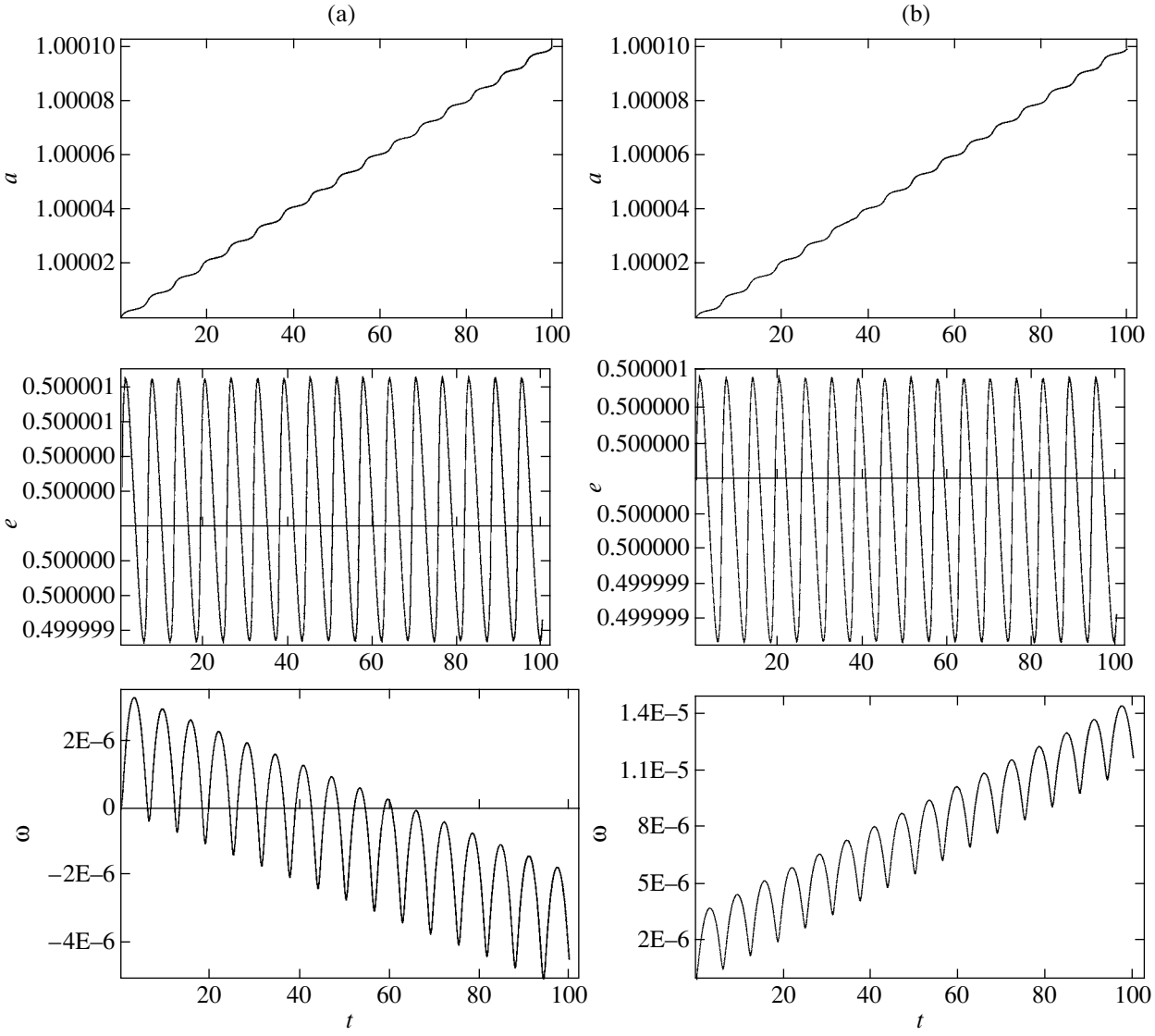

Fig. 1. (a) Time dependence of the semimajor axis, eccentricity, and pariastron passage for Case 1; (b) the same dependence for Case 2.

Andrade and Docobo 2002) that not all of the distant-dependent mass-loss laws produce a secular increase in eccentricity.

Here, we present a family of mass-loss laws (depending both on time and distance) leading to integrable cases.

INTEGRABLE CASES

Let us assume the gravitational constant $G = 1$ and the total mass $m = m_1 + m_2$ such that $\mu = G(m_1 + m_2) = m$.

It is well known that by introducing the following change of coordinates and time:

$$\mathbf{R} = \frac{\mathbf{r}}{1+\alpha t} \quad \text{and} \quad \tau = \frac{t}{1+\alpha t}, \tag{4}$$

where $\alpha \in \mathbb{R}^+$, the equations of motion (1) are transformed into

$$\mathbf{R}'' = -\mu(\tau)\frac{1}{1-\alpha\tau}\frac{\mathbf{R}}{R^3} \tag{5}$$

or

$$\mathbf{R}'' = -\mu(t)(1+\alpha t)\frac{\mathbf{R}}{R^3},$$

where $(''$) denote the second derivative with respect to the new time τ and $R = |\mathbf{R}|$.

Let us now consider a more general law of mass loss, namely, the one given by

$$\mu(t,r) = \frac{1}{1+\alpha t} + \sum_{i=n}^{m}(-1)^{k_i}\beta_i\left(\frac{1}{r}\right)^i(1+\alpha t)^{i-1}, \tag{6}$$

where α and β_i are positive (or with some β_i eventually equal to zero) real parameters; n and m are integers, with $n \leq m$ and k_i being 0 or 1.

The above change of variables (4) and (6) converts the equations of motion (1) into

$$\mathbf{R}'' = -\frac{\mathbf{R}}{R^3} + \sum_{i=n}^{m}(-1)^{k_i}\beta_i \frac{\mathbf{R}}{R^{i+3}}, \qquad (7)$$

which represents the motion of a particle in a central force field derived from the potential function

$$V = -\frac{1}{R} + \sum_{i=n}^{m}(-1)^{k_i}\frac{\beta_i}{(i+1)}R^{i+1} \qquad (8)$$

and which is integrable, because it is a problem with one degree of freedom. For instance, for $n = m = 2$, we obtain a potential similar to the one explaining the perihelion relativistic advance in planetary orbits. The motion is planar and the vector $\mathbf{R}$ describes the precession ellipse; this precession effect is an increasing monotonic function of the parameter β_2.

The trajectory that describes the vector $\mathbf{r}$ is also planar and it is a spiral (more closed corresponding to the smaller α) that also precesses.

It is noteworthy that, in general, the parameters α and β_i have not to be small. When $\beta_i \ll \alpha$, we obtain a Gylden–Meshcherskii perturbed problem.

Under these latter conditions and taking into account the aforementioned, one might expect this mass-loss law ($n = m = 2$) and, in general, other suggested laws to produce a secular variation both in semimajor axis and in periastron argument but not in eccentricity.

Another different integrable case is obtained when the mass-loss law is given by

$$\mu(t, r) = \frac{r^3}{(1+\alpha t)^4}. \qquad (9)$$

Indeed, with this law, Eq. (5) converts into

$$\mathbf{R}'' = -\mathbf{R},$$

which represents a harmonic oscillator.

NUMERICAL EXAMPLES

To put into practice the aforementioned, let us consider two special cases of law (6):

$$\mu_1 = \frac{1}{1+\alpha t} - \frac{\beta_2}{r^2}(1+\alpha t), \qquad (10)$$

$$\mu_2 = \frac{1}{(1+\alpha t)} + \frac{\beta_3}{r^3}(1+\alpha t)^2 - \frac{\beta_4}{r^4}(1+\alpha t)^3. \qquad (11)$$

In the first case, the parameters were chosen to be $\alpha = 10^{-6}$ and $\beta_2 = 10^{-8}$, while in the second case, they are $\alpha = 10^{-6}$, $\beta_3 = 10^{-8}$, and $\beta_4 = 10^{-9}$.

In both cases, the initial values of the orbital elements and mass were the following: $\mu_0 = 1$ (distance unit)^3/(time unit)^2, $f = 0$, $e = 0.5$, $a = 1$ distance unit, and $\omega = 0$.

We performed a numerical integration with a fourth-order Runge–Kutta method within a time span of 100 time units. Our results are shown in the figure. It can be seen that the semimajor axis, eccentricity, and periastron argument show the trends suggested above. Therefore, in these cases, the trajectories will be spirals in rotation.

CONCLUSIONS

Should all of the coefficients β_i in expression (6) be zero, we deal with one of the Meshcherskii solutions; e.g., the trajectory should be conical in the plane $\mathbf{R}$ and spiral in the plane $\mathbf{r}$.

Laws (6) represent an extension of the previous situation that gives rise to the integrable cases where both the periastron argument and the semimajor axis present a secular variation. Thus, the aforementioned spirals are now in rotation but the orbital eccentricity presents no secular variation.

Actually, with the aim of giving a mathematical response to the physical suggestion mentioned in the Introduction, we are working on the characteristic mass-loss laws that produce a secular increase in eccentricity.

ACKNOWLEDGMENTS

I thank Prof. A. Elipe for valuable remarks. This work is part of the Investigation Project AYA 2001-3073 of the Ministerio de Ciencia y Tecnologia (Spain).

REFERENCES

1. M. Andrade and J. A. Docobo, *Monogr. del Seminario Matemático "García de Galdeano,"* No. 21, 131 (Zaragoza, 2001a).
2. M. Andrade and J. A. Docobo, *Proceedings of International Conference on Classical Nova Explosions*, Ed. by M. Hernanz and J. Jose (American Institute of Physics, New York, 2002), Vol. 637, p. 82.
3. M. Andrade and J. A. Docobo, *Proceedings of the 4th Scientific Meeting of the Spanish Astronomical Society (SEA), Santiago de Compostela*, Ed. by J. Zamorano, J. Gorgas, and J. Gallego (Kluwer Academic Publishers, Dordrecht, 2001b), p. 273.

4. M. Andrade and J.A. Docobo, *Highlights of Spanish Astrophysics II, Proc. of the 4th Scientific Meeting of the Spanish Astronomical Society (SEA)*, Ed. by J. Zamorano, J. Gorgas, and J. Gallego, (Kluwer Academic Publishers, Dordrecht, 2001), p. 273.
5. L. Chiara, Publ. Oss. Astron. Palermo **10**, 8 (1957); **10**, 3 (1957).
6. J. A. Docobo and M. Andrade, *Métodos de dinámica orbital y rotacional* (Prensas Universitarias, Univ. de Murcia, Spain, 2002), p. 121.
7. J. A. Docobo and C. Prieto, *Boletín Real Instituto y Obseravtorio de la Armada en San Fernando*, No. 5, p. 13 (1998).
8. J. A. Docobo, C. Prieto, and J. Ling, Astrophys. Space Sci. **261**, 205 (1999a).
9. J. A. Docobo, P. Abelleira, and J. Blanco, *Monografías de la Academia de Ciencias de Zaragoza*, No. 14, p. 33 (1999b).
10. J. Dommanget, in *Proceedings of the Fifty-ninth Colloquium "Effects of Mass Loss on Stellar Evolution,"* Ed. by C. Chiosi and R. Stalio (Italy, D. Reidel Publishing, Dordrecht, Trieste, 1981), p. 507.
11. J. Dommanget, in *Proceedings of the 69th Coll. of IAU "Binary and Multiple Stars as Tracers of Stellar Evolution",* Ed. by Z. Kopal and J. Rahe (Italy, D. Reidel Publishing, Dordrecht, Trieste, 1982), p. 119.
12. J. Dommanget, in *Visual Double Stars: Formation, Dynamics, and Evolutionary Tracks,* Ed. by J. A. Docobo, A. Elipe, and H. McAlister (Kluwer Academic Publishers, Dordrecht, 1997), p. 403.
13. W. Hartkopf and B. Mason, 2001, http://ad.usno.navy.mil/wds/orb6.html.
14. M. M. Katsova and A. G. Shcherbakov, *Proceedings of ESO Workshop "Cyclical Variability in Stellar Winds"* (Springer Verlag, 1998,) p. 230.
15. E. L. Martin, *Real Stazione Astron. Geof. de Carlofonte* (Cagliari), No. 36 (1934).
16. A. F. J. Moffat, Astrophys. Space Sci. **260**, 225 (1998).
17. G. Rauw, J-M. Vreux, and E. Gosset, Rev. Mex. Astron. Astrofis. (Conf. Ser.) **5**, 108 (1996).
18. St. Louis, Rev. Mex. Astron. Astrofis. (Conf. Ser.) **5**, 76 (1996).
19. N. Soker, Astron. Astrophys. **357**, 557 (2000).

Astronomy Letters, Vol. 29, No. 5, 2003, pp. 348–351. Translated from Pis'ma v Astronomicheskiĭ Zhurnal, Vol. 29, No. 5, 2003, pp. 397–400.

A Basic System of Equations in the Field of a Rotationally Symmetric Potential

T. A. Agekyan*

Astronomical Institute, St. Petersburg State University, Universitetskii pr. 28, Petrodvorets, 198504 Russia

Received September 12, 2002

Abstract—We consider system of equations of motion in the field of a rotationally symmetric potential.
© *2003 MAIK "Nauka/Interperiodica".*

Key words: *celestial mechanics.*

FORMULATION OF THE PROBLEM

A rotationally symmetric potential is the most widespread form of potential in nature. The gravitational fields of the Earth, other planets and their satellites, stars, globular clusters, and elliptical and spiral galaxies are exactly or almost exactly rotationally symmetric. There are grounds for believing that rotationally symmetric force fields are also widespread in the microworld.

In a rotationally symmetric potential, the infinite trajectory of a mass point fills a torus, all of whose meridional cross sections are identical. To determine the laws of motion of a particle in a rotationally symmetric potential, it will suffice to study the patterns of its motion in the meridional (comoving) plane that passes through the particle and the axis of the rotationally symmetric potential.

THE BASIC EQUATION

Denote the angle between the tangent to the trajectory in the meridional plane and the x axis in this plane by f.

Based on some obvious properties of the third integral of motion and using the Boltzmann equation, we previously (Agekyan 1972) derived the following equation of the trajectory in the meridional plane:

$$\frac{\partial f}{\partial R}\cos f + \frac{\partial f}{\partial z}\sin f + \frac{1}{2(U+I)} \times \left(\frac{\partial U}{\partial R}\sin f - \frac{\partial U}{\partial z}\cos f\right) = 0, \quad (1)$$

where $U(R,z)$ is the potential in the meridional plane defined by the equality

$$U(R,z) = \Phi(R,z) - \frac{J^2}{2R^2},$$

where $\Phi(R,z)$ is the rotationally symmetric potential, J is the area integral, and I is the energy integral.

Sidorova (2000) showed that Eq. (1) can be derived more easily by excluding time from the equations of motion.

Given $U(R,z)$, I, and the angle f at some point (R,z) in the meridional plane, Eq. (1) defines the orbit that is filled with the turns of the infinite particle trajectory. In this case, the value of the third integral of motion is fixed, although it remains unknown.

Figure 1 shows the results of our numerical integration of Eq. (1) over a long time interval for

$$U(R,z) = -\frac{1}{2}(R^2+z^2) - Rz^2 + \frac{1}{3}R^3,$$
$$I = 0.051.$$

The coordinate origin is at the circular point. The points closer to the rotation axis of the system then have negative coordinates R. The angle f was specified at some initial point (R_0, z_0).

In the regions of the orbit where the two conjugate trajectory turns with the angles f and α intersect at each point, the equation

$$\frac{\partial \alpha}{\partial R}\cos\alpha + \frac{\partial \alpha}{\partial z}\sin\alpha + \frac{1}{2(U+I)} \times \left(\frac{\partial U}{\partial R}\sin\alpha - \frac{\partial U}{\partial z}\cos\alpha\right) = 0 \quad (2)$$

defines the same orbit as Eq. (1).

In the regions where four or more turns pass through each point (there are three such regions in Fig. 1), the turns each time break down into pairs of conjugated turns. We can always consider the pairs of conjugate equations (1) and (2).

Here, there is an uncertainty. Whereas the angle f is known exactly at the point of intersection, this is

*E-mail: vor@astro.spbu.ru

1063-7737/03/2905-0348$24.00

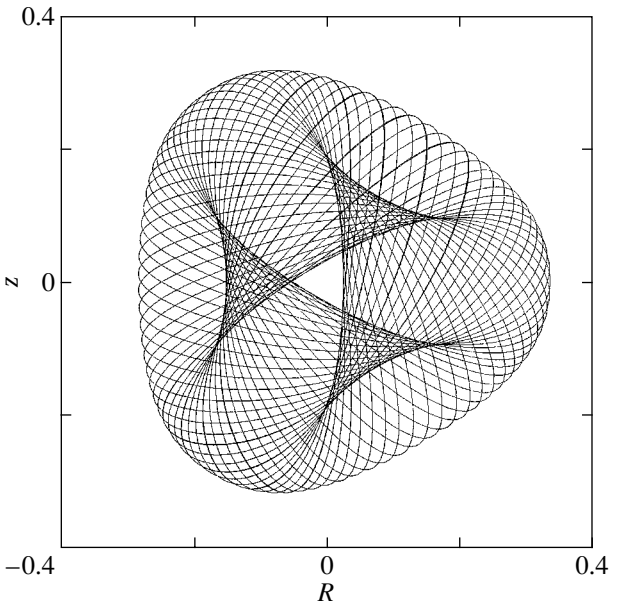

Fig. 1. The trajectory of a particle in the potential of Hénon and Heiles (1964). The energy integral is equal to $I = 0.051$. The coordinates of the staring point are $R_0 = -0.15$, $z_0 = 0$.

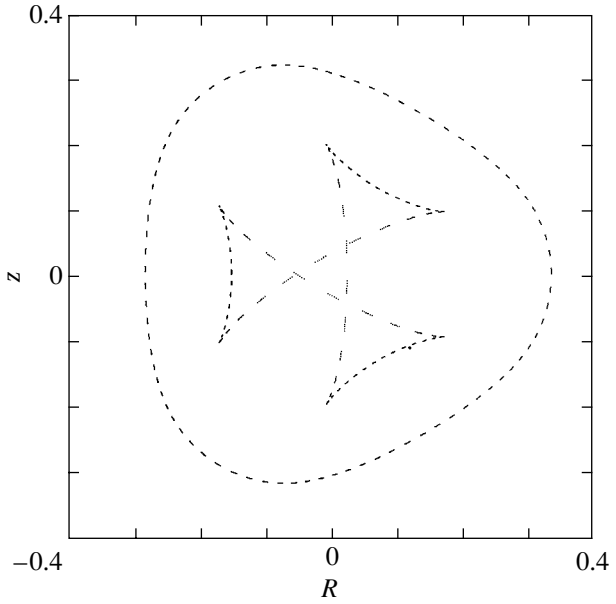

Fig. 2. The shape of the orbital contours and the velocity-field folds for the particle trajectory shown in Fig. 1.

not the case for the angle α. The uncertainty should be removed by assuming that f is conjugate to such an angle α at which the same orbit, the same (unknown) value of the third integral of motion, corresponds to Eq. (2).

When differentiated with respect to f and α, Eqs. (1) and (2) preserve the orbit and the third integral of motion.

AN EQUATION VALID ON THE CONTOURS OF THE ORBIT AND THE FOLDS OF THE DIRECTION FIELD

The derivative of the angle f along the normal to the trajectory ($\partial f/\partial n$) has a peculiar property. Agekyan and V'yuga (1973) and Saginashvili (1975), who considered the problem in the fields of quasi-Newtonian and quasi-Hooke potentials, respectively, showed that $\partial f/\partial n = \pm\infty$ on the contours of the orbit and the folds of the direction fields. This property is valid for any rotationally symmetric potentials.

Previously (Agekyan 1974), we derived the following equation for $\partial f/\partial n$:

$$\frac{\partial}{\partial l}\frac{\partial f}{\partial n} + \left(\frac{\partial f}{\partial n}\right)^2 + \frac{1}{2(U+I)} \tag{3}$$
$$\times \left(\frac{\partial U}{\partial R}\cos f + \frac{\partial U}{\partial z} sinf\right)\frac{\partial f}{\partial n} + \frac{3}{4(U+I)^2}$$
$$\times \left(-\frac{\partial U}{\partial R}\sin f + \frac{\partial U}{\partial z}\cos f\right)^2 + \frac{1}{2(U+I)}$$
$$\times \left(-\frac{\partial^2 U}{\partial R^2}\sin^2 f + 2\frac{\partial^2 U}{\partial R \partial z}\sin f \cos f - \frac{\partial^2 U}{\partial z^2}\cos^2 f\right).$$

In general, this equation is approximate, because it is derived by using differentiation along the normal to the trajectory.

Agekyan and Yakimov (1976) showed that, if one numerically integrates Eq. (1) and simultaneously integrates Eq. (3) along the trajectory turns obtained and mark the points at which $\partial f/\partial n = \pm\infty$, then the contours of the orbit and the folds of the direction field can be accurately outlined. In this case, there is no need to plot the trajectory turns; the picture of the contours of the orbits and the folds of the direction field is well defined in close agreement with what is obtained when numerically integrating Eq. (1). This is shown by Fig. 2.

Pit'ev (1980, 1981), Agekyan (1992), Myullyari and Orlov (1993), and Dubinina (2001) confirmed the accuracy of the described method. Agekyan and Orlov (2002) showed that this method is accurate, because Eq. (3) is exact on the contours of the orbits and the folds of the direction field; on these contours, differentiating along the normal to the trajectory does not change the orbit or the third integral of motion.

ADDITIONAL EQUATIONS

Let us denote

$$h(R,z) = U(R,z) + I,$$

$$a_1 = \frac{\partial^2 f}{\partial z^2} - \frac{\partial f}{\partial R}\frac{\partial f}{\partial z} + \frac{1}{2h}\frac{\partial f}{\partial z}\frac{\partial U}{\partial z} + \frac{1}{2h}\frac{\partial^2 U}{\partial R \partial z} - \frac{1}{2h^2}\frac{\partial U}{\partial R}\frac{\partial U}{\partial z},$$

$$a_2 = \frac{\partial^2 f}{\partial R \partial z} - \left(\frac{\partial f}{\partial R}\right)^2 + \frac{1}{2h}\frac{\partial f}{\partial R}\frac{\partial U}{\partial z} + \frac{1}{2h}\frac{\partial^2 U}{\partial R^2} - \frac{1}{2h^2}\left(\frac{\partial U}{\partial R}\right)^2,$$

$$a_3 = \frac{\partial^2 f}{\partial R \partial z} + \left(\frac{\partial f}{\partial z}\right)^2 + \frac{1}{2h}\frac{\partial f}{\partial z}\frac{\partial U}{\partial R} - \frac{1}{2h}\frac{\partial^2 U}{\partial z^2} + \frac{1}{2h^2}\left(\frac{\partial U}{\partial z}\right)^2,$$

$$a_4 = \frac{\partial^2 f}{\partial R^2} + \frac{\partial f}{\partial R}\frac{\partial f}{\partial z} + \frac{1}{2h}\frac{\partial f}{\partial R}\frac{\partial U}{\partial R} - \frac{1}{2h}\frac{\partial^2 U}{\partial R \partial z} + \frac{1}{2h^2}\frac{\partial U}{\partial R}\frac{\partial U}{\partial z},$$

$$a_5 = \frac{\partial^2 f}{\partial z^2} + \frac{1}{2h}\frac{\partial f}{\partial R}\frac{\partial U}{\partial R} + \frac{1}{2h}\frac{\partial^2 U}{\partial R \partial z} - \frac{3}{4h^2}\frac{\partial U}{\partial R}\frac{\partial U}{\partial z},$$

$$a_6 = 2\frac{\partial^2 f}{\partial R \partial z} - \frac{1}{2h}\frac{\partial f}{\partial z}\frac{\partial U}{\partial R} - \frac{1}{2h}\frac{\partial f}{\partial R}\frac{\partial U}{\partial z} + \frac{1}{2h}\frac{\partial^2 U}{\partial R^2} - \frac{1}{2h}\frac{\partial^2 U}{\partial z^2} - \frac{3}{4h^2}\left(\frac{\partial U}{\partial R}\right)^2 + \frac{3}{4h^2}\left(\frac{\partial U}{\partial z}\right)^2,$$

$$a_7 = \frac{\partial^2 f}{\partial R^2} + \frac{1}{2h}\frac{\partial f}{\partial z}\frac{\partial U}{\partial z} - \frac{1}{2h}\frac{\partial^2 U}{\partial R \partial z} + \frac{3}{4h^2}\frac{\partial U}{\partial R}\frac{\partial U}{\partial z},$$

$$b_1 = \frac{\partial^2 \alpha}{\partial z^2} - \frac{\partial \alpha}{\partial R}\frac{\partial \alpha}{\partial z} + \frac{1}{2h}\frac{\partial \alpha}{\partial z}\frac{\partial U}{\partial z} + \frac{1}{2h}\frac{\partial^2 U}{\partial R \partial z} - \frac{1}{2h^2}\frac{\partial U}{\partial R}\frac{\partial U}{\partial z},$$

$$b_2 = \frac{\partial^2 \alpha}{\partial R \partial z} + \left(\frac{\partial \alpha}{\partial z}\right)^2 + \frac{1}{2h}\frac{\partial \alpha}{\partial z}\frac{\partial U}{\partial R} - \frac{1}{2h}\frac{\partial^2 U}{\partial z^2} + \frac{1}{2h^2}\left(\frac{\partial U}{\partial z}\right)^2,$$

$$b_3 = \frac{\partial^2 \alpha}{\partial R \partial z} - \left(\frac{\partial \alpha}{\partial R}\right)^2 + \frac{1}{2h}\frac{\partial \alpha}{\partial R}\frac{\partial U}{\partial z} + \frac{1}{2h}\frac{\partial^2 U}{\partial R^2} - \frac{1}{2h^2}\left(\frac{\partial U}{\partial R}\right)^2,$$

$$b_4 = \frac{\partial^2 \alpha}{\partial R^2} + \frac{\partial \alpha}{\partial R}\frac{\partial \alpha}{\partial z} + \frac{1}{2h}\frac{\partial \alpha}{\partial R}\frac{\partial U}{\partial R} - \frac{1}{2h}\frac{\partial^2 U}{\partial R \partial z} + \frac{1}{2h^2}\frac{\partial U}{\partial R}\frac{\partial U}{\partial z},$$

$$b_5 = \frac{\partial^2 \alpha}{\partial z^2} + \frac{1}{2h}\frac{\partial \alpha}{\partial R}\frac{\partial U}{\partial R} + \frac{1}{2h}\frac{\partial^2 U}{\partial R \partial z} - \frac{3}{4h^2}\frac{\partial U}{\partial R}\frac{\partial U}{\partial z},$$

$$b_6 = 2\frac{\partial^2 \alpha}{\partial R \partial z} - \frac{1}{2h}\frac{\partial \alpha}{\partial z}\frac{\partial U}{\partial R} - \frac{1}{2h}\frac{\partial \alpha}{\partial R}\frac{\partial U}{\partial z} + \frac{1}{2h}\frac{\partial^2 U}{\partial R^2} - \frac{1}{2h}\frac{\partial^2 U}{\partial z^2} - \frac{3}{4h^2}\left(\frac{\partial U}{\partial R}\right)^2 + \frac{3}{4h^2}\left(\frac{\partial U}{\partial z}\right)^2,$$

$$b_7 = \frac{\partial^2 \alpha}{\partial R^2} + \frac{1}{2h}\frac{\partial \alpha}{\partial z}\frac{\partial U}{\partial z} - \frac{1}{2h}\frac{\partial^2 U}{\partial R \partial z} + \frac{3}{4h^2}\frac{\partial U}{\partial R}\frac{\partial U}{\partial z}.$$

Differentiate Eqs. (1) and (2) with respect to f and α:

$$a_1 \tan f \tan\alpha + a_2 \tan f + a_3 \tan\alpha + a_4 = 0, \quad (4)$$
$$b_1 \tan f \tan\alpha + b_2 \tan f + b_3 \tan\alpha + b_4 = 0,$$
$$a_5 \tan^2 f + a_6 \tan f + a_7 = 0,$$
$$b_5 \tan^2\alpha + b_6 \tan\alpha + b_7 = 0.$$

Eliminating $\tan f$ and $\tan\alpha$ from Eqs. (4), we obtain

$$(-a_1a_5b_4 + a_1a_6b_2 + a_2a_5b_3 - a_2a_6b_1 - a_3a_5b_2 + a_4a_5b_1)(-a_1a_7b_4 + a_2a_7b_3 + a_3a_6b_4 - a_3a_7b_2 - a_4a_6b_3 + a_4a_7b_1) + (a_1a_7b_2 - a_2a_7b_1 - a_3a_5b_4 + a_4a_5b_3)^2 = 0, \quad (5)$$

$$(-b_1b_5a_4 + b_1b_6a_3 - b_2b_5a_3 - b_3b_6a_1 + b_3b_5a_2 + b_4b_5a_1)(-b_1b_7a_4 + b_2b_6a_4 - b_2b_7a_3 + b_3b_7a_2 - b_4b_6a_2 + b_4b_7a_1) + (b_1b_7a_3 - b_2b_5a_4 - b_3b_7a_1 + b_4b_5a_2)^2 = 0. \quad (6)$$

Equations (5) and (6) contain derivatives only up to the second order with respect to f and α. The system of equations and equalities that defines the motion in the field of a rotationally symmetric potential has the following form:

(I) In the region of possible motions in the meridional plane, f and α are the angles of conjugate trajectories. Equations (1), (2), (5), and (6) are valid.

(II) On the contours of the orbit and the folds of the direction field, $f = \alpha$, $\partial f/\partial n = \pm\infty$, and Eq. (3) is valid.

(III) When Eqs. (1) and (3) are simultaneously numerically integrated, the points at which $\partial f/\partial n = \pm\infty$ accurately outline the contours of the orbit and the folds of the direction field.

REFERENCES

1. T. A. Agekyan, Astron. Zh. **49**, 371 (1972) [Sov. Astron. **16**, 303 (1972)].
2. T. A. Agekyan, Dokl. Akad. Nauk SSSR **214**, 783 (1974).
3. T. A. Agekyan and A. A. V'yuga, Vestn. Leningr. Univ. **7**, 128 (1973).
4. T. A. Agekyan and S. P. Yakimov, Vestn. Leningr Univ. **13**, 177 (1976).
5. T. A. Agekyan, A. A. Myullyari, and V. V. Orlov, Astron. Zh. **69**, 469 (1992) [Sov. Astron. **36**, 236 (1992)].
6. T. A. Agekyan and V. V. Orlov, Pis'ma Astron. Zh. **28**, 71 (2002) [Astron. Lett. **28**, 63 (2002)].
7. L. Dubinina, in *Stellar Dynamics: From Classic to Modern*, Ed. by L. P. Ossipkov and I. I. Nikiforov (St. Petersburg: St. Petersburg University, 2001), p. 198.
8. M. Hénon and C. Heiles, Astron. J. **69**, 73 (1964).
9. A. A. Myullyari and V. V. Orlov, Vestn. St. Peterburg. Univ. **15**, 120 (1993).
10. N. P. Pit'ev, Vestn. Leningr. Univ. **19**, 98 (1980).
11. N. P. Pit'ev, Astron. Zh. **58**, 528 (1981) [Sov. Astron. **25**, 299 (1981)].
12. M. G. Saginashvili, Bull. Abastuman. Astrophys. Obs. **46**, 125 (1974).
13. V. K. Sidorova, Diploma, St. Peterburg. State Univ. (2000).

Translated by A. Dambis